Fusion Energy Engineering Laboratory (FEEL)
Departament de Física i Enginyeria Nuclear
Escola Tècnica Superior d'Enginyeria Industrial de Barcelona
UNIVERSITAT POLITÈCNICA DE CATALUNYA

PhD thesis presented by

Jerónimo García Olaya

For the degree of doctor at the

UNIVERSITAT POLITÈCNICA DE CATALUNYA

Study of electron heat transport in LHD and TJ-II

Director

Javier Dies
Professor at the UPC

Para mis padres

FAUST:
Werd ich beruhigt je mich auf ein Faulbett legen,
So sei es gleich um mich getan!
Kannst du mich schmeichelnd je belügen,
Daß ich mir selbst gefallen mag,
Kannst du mich mit Genuß betrügen-
Das sei für mich der letzte Tag!
Die Wette biet ich!

MEPHISTOPHELES:
Topp!

FAUST:
Und Schlag auf Schlag!
Werd ich zum Augenblicke sagen:
Verweile doch! du bist so schön!
Dann magst du mich in Fesseln schlagen,
Dann will ich gern zugrunde gehn!
Dann mag die Totenglocke schallen,
Dann bist du deines Dienstes frei,
Die Uhr mag stehn, der Zeiger fallen,
Es sei die Zeit für mich vorbei!

(Goethe, Faust)

Acknowledgments

I am deeply grateful to Professor Javier Dies, my thesis director, for allowing me to make this thesis and helping me as much as possible, including my participation in several national fusion projects.

I will be in debt for live with Professor Kozo Yamazaki, from National Institute for Fusion Science, for making my long stages in Japan as comfortable as possible, for his continues encourage and help, for solving my scientific doubts with his incredible patience, and finally, for our long talks about scientific (and non scientific) subjects which have always contributed to my scientific and human apprenticeship.

I wish to acknowledge the contribution of Dr. Francisco Castejón from CIEMAT for offering valuable suggestions, comments and stimulating discussions throughout this thesis.

My special thanks to Dr. Ferran Albajar for sharing with me his deeply knowledge about cyclotron radiation as well as for his permanently encourage and optimism whatever the situation was.

I am also grateful to Dr. Josep Maria Fontdecaba and Dr. Joan Fontanet, for their help in solving my innumerable doubts about PRETOR-Stellarator code. Without them, I would not know how this code works yet.

I do not want to forget Jesús Izquierdo. His encourage, dynamism, optimism and friendship as well as his valuable and right comments about my research have made possible this thesis.

I also wish to acknowledge to the “Departament de Fisica i Enginyeria Nuclear” and the “Seccio d’Enginyeria Nuclear” for their help.

Contents

Introduction

Framework

This thesis has been carried out in the framework of three different National Plans from the Spanish “Ministerio de Ciencia y Tecnología”:

- “TJ-II and LHD transport studies with semiempirical and theoretical models using remote participation techniques” (ENE2004-05647-FTN).

- “Contribution to the remote study of Transport in TJ-II. Remote operation of the charge exchange spectrometer“(FTN2000-1743-C02-02).

- “Implementation of synchrotron radiation losses in international plasma simulation codes. Application to ITER” (FTN2002-02601).

The author has taken advantage of the infrastructure of the “Departament de Física i Enginyeria Nuclear” at the “Universitat Politècnica de Catalunya”. Numerical simulations have been performed using several PC’s and a 64-bits Compaq Alpha server workstation.

Objectives and plan of the thesis

The main objectives of this thesis are as follows:

- Contribution to the knowledge of neoclassical and anomalous electron thermal transport in the Large Helical Device (LHD) and TJ-II with the aim

of analyzing the physical mechanism responsible of the high levels of turbulence present in most of the shots.

- To analyze the Internal Transport Barrier formation in LHD and TJ-II in order to compare if both devices share the physical mechanism responsible of the turbulent transport suppression.
- Study of the non-local (non diffusive) electron thermal transport phenomena which is present in many experiments in LHD and TJ-II.
- Use of the previous knowledge to study the similarities and differences of the stellarator and tokamak future commercial reactor.

In Chapter 1, the more important energy issues worldwide are discussed. In addition, fusion energy is presented as a solution for these problems. Finally, ITER and the future fusion commercial reactor characteristics are shown.

In Chapter 2, a detailed analysis of the stellarator devices LHD and TJ-II, whose plasmas have been studied throughout this thesis, is described.

In Chapter 3, the plasma transport codes used in this thesis, TOTAL and PRETOR-Stellarator, are deeply described.

In Chapter 4, the remote participation tools used along this thesis are shown.

In Chapter 5, neoclassical transport theory in stellarators is described. A particular model of this transport, which allows a fast computation of diffusivities as well as electric field, is used with PRETOR-Stellarator to study neoclassical transport in TJ-II and LHD. Results show good agreement with previous studies made with more sophisticated routines and with experimental data.

In Chapter 6, with the aim of analyzing the physical mechanism involved in the electron thermal transport channel in TJ-II, some transport models have been added to PRETOR-Stellarator. Simulations show that electromagnetic driftwaves can drive electron anomalous transport in TJ-II. In addition, the W7-AS transport model based in the W7-AS scaling can be a good tool to simulate TJ-II shots with no enhanced heat confinement.

In Chapter 7, a complete analysis of the suppression of anomalous transport in LHD and TJ-II by the $E \times B$ sheared flow is carried out. It is shown that this mechanism can be effective enough to generate plasma regimes with Internal Transport Barrier. Moreover, comparing the results with the experimental data, it is demonstrated that the neoclassical

model implemented in PRETOR-Stellarator is a powerful tool to analyze neoclassical transport as well as its interaction with anomalous one.

In Chapter 8, a new transport model is proposed to analyze and to simulate the non-diffusive/non-local heat transport. The new model is based in the neoclassical transport non-locality. This model is able to simulate the main features of non-local transport, e.g.: very fast perturbation propagation, velocity increasing in the plasma core, instability growing in the plasma core and at the edge or the “ballistic transport”.

Finally, in Chapter 9, a comparison between the main characteristics and differences of the stellarator commercial reactor and the tokamak one are analyzed. In the stellarator case, the commercial reactor based on a LHD-like design should be a factor 5 larger than the LHD. This configuration leads to 450MW fusion power in a continuum regime. The main problem for this configuration is that ion anomalous transport should be small. Unlike in the stellarator case, it is shown that cyclotron radiation can be the main source of energy losses for the electrons for tokamaks. A detailed study of this radiation and the influence of wall reflection coefficient on plasma equilibrium is done.

Chapter 1

Nuclear fusion as future primary energy source

1.1 Introduction

Energy sources are becoming one of the most important problems of whole the humanity. Several key factors determine how energy and its sources are evolving, e.g. world population and growth of economy, social behaviour, contamination or technology. In fact, all these factors are in correlation, since the growth of economy tends to make the social behaviour western-like with a very high energy consuming rates. This fact also contributes to the population growing since technology is able to make the life longer. All these features contribute to the high contamination levels of the atmosphere (mainly due to burning fossil fuels) which, as has been pointed several times, may lead to the climate change.

According to the United Nations [UN05], the world population can reach 9 millions in 2050, see figure 1.1, which means upon 1.5 times the actual population. Moreover, this growing rate is expected to continue until 2100. Taking account the fact that most of this population will be from developing countries, which at the present time lack of most of the advanced technologies but in the future will be able to access, will make the energy demanding rise in a considerable manner.

Some decisions have been taken in the developed countries to avoid this increasing demanding. Perhaps, the most important one is to convince the population in not wasting energy, and always, if possible, try to recycle. These decisions have result to be positive, since the total energy demanding is stabilized. However, these proposals cannot be followed in the developing countries, since in order to improve the quality life of the population, the growth of energy demanding is absolutely necessary.

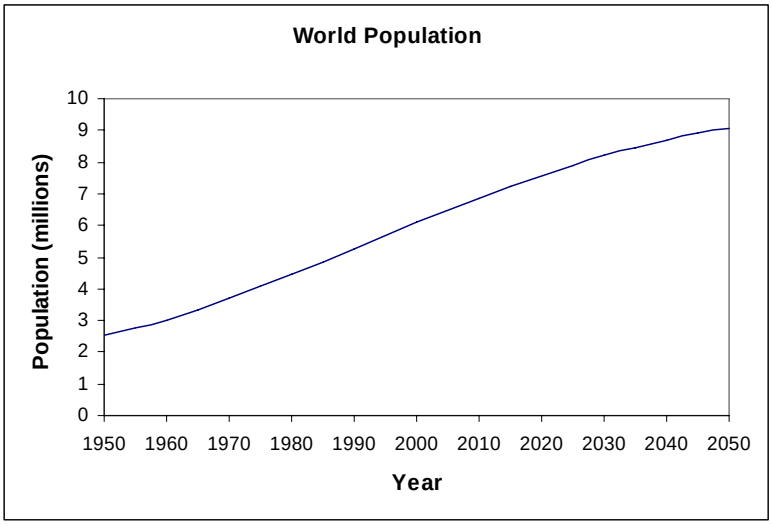

Figure 1.1 Evolution of the world population according to the United Nations [UN05].

At the present time, the energy demanding is supplied mainly by burning fossil fuels, as can be seeing in table 1.1. In this situation, the compliance of the stabilisation CO2 emission to the atmosphere (Kyoto Protocol and the UNFCCC[1] objectives) seems to be difficult. Moreover, EEUU which is the country with more CO2 emissions has not signed these protocols yet. Therefore, the CO2 concentration in the atmosphere, which has been growing in the last 200 years, is expected to keep rising, as shown in figure 1.2, taking account the new development of some countries, e.g. China.

Energy source	Primary energy production (%)
Oil	39.4
Natural gas	23.9
Coal	22.3
Hydroelectricity	7.1
Nuclear fission	6.6
Others (renewable)	0.7

Table 1.1 Contribution of the main energy sources to the primary energy production in the world [EIA99].

According to table 1.1, if CO2 emissions must be reduced, few possibilities are available. Unfortunately, renewable energies are not still able to supply sufficient energy for the world population. Besides, their efficacy must be improved. Related to nuclear

fission, although it is a free CO2 emission energy, is subject to an unfavourable social opinion, due to the long-term radioactive waste that generate and to the association of this energy with military subjects.

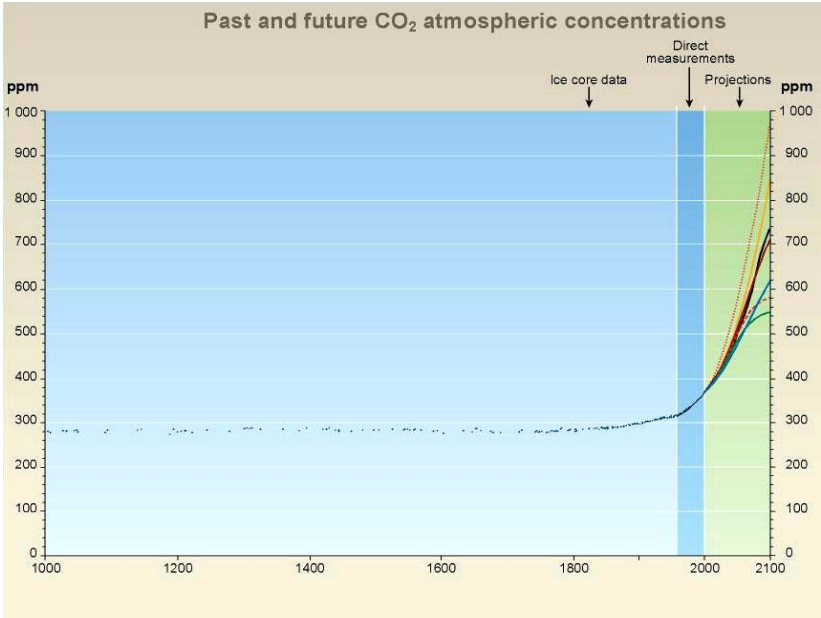

Figure 1.2 Evolution of the CO2 concentration in the atmosphere (in ppm) in the last 1000 years and several projections for the next century [UNE01].

Finally, another problem arises from the dependence on the oil as a primary energy production. As can be seen in figure 1.3, the expected annual oil production worldwide may drop by 2005 because the world reserves are falling. This fact, together with the continuum population growing (which will induce a demanding rise) may lead to an important rise in the oil prices and the lack of petroleum availability. In fact, this behaviour is being confirmed since 2004, from that year, and meanly in 2005, the oil prices are rising continuously.

With the aim of solving the problems previously described there are basically two possibilities. First, keep working on renewal energies, improving their efficiency and trying that this kind of energy be possible not just for developed countries but for developing countries, which have the same rights to be developed societies. Second, keep also working in fusion, which is an energy that seems to meet all the needs previously described, and, in the case that finally it results to be a commercial energy, it will available for whole the humanity.

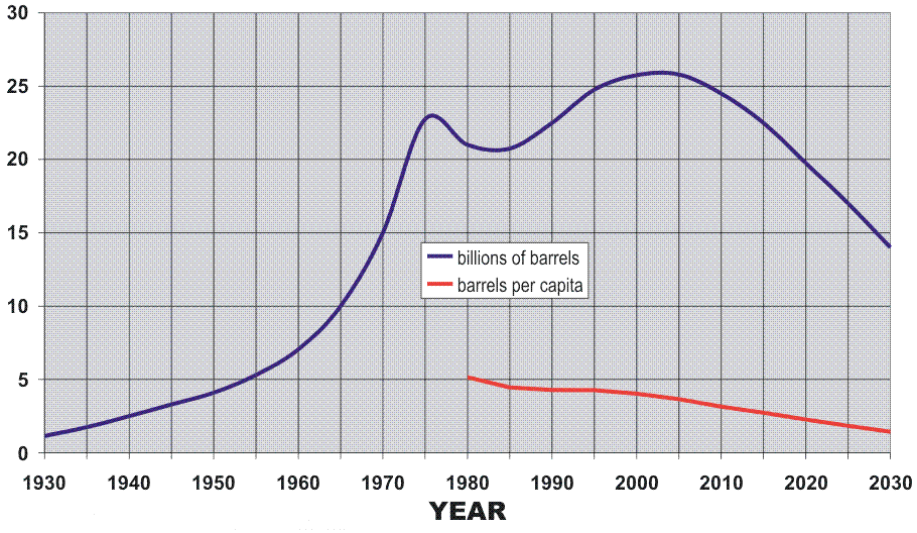

Figure 1.3 Evolution of the annual oil production worldwide in billions of barrels (blue) and the barrels per capita available (red) [Cam98].

1.2 Fusion energy

As pointed in the previous section, fusion energy is a real solution for the future energy problems. The fuel sources for this energy are almost inexhaustible and available worldwide. It respects the environment, since there are no CO2 emissions to the atmosphere, and, unlike the fission case, the low production of radioactive waste is perfectly assumable by the society. Moreover, fusion energy represents a next-step from the safety point of view compared with fission energy, since the loss of plasma control does not lead to the emission of high levels of energy and radioactivity to the atmosphere, otherwise, the reaction tends to stop in a few seconds.

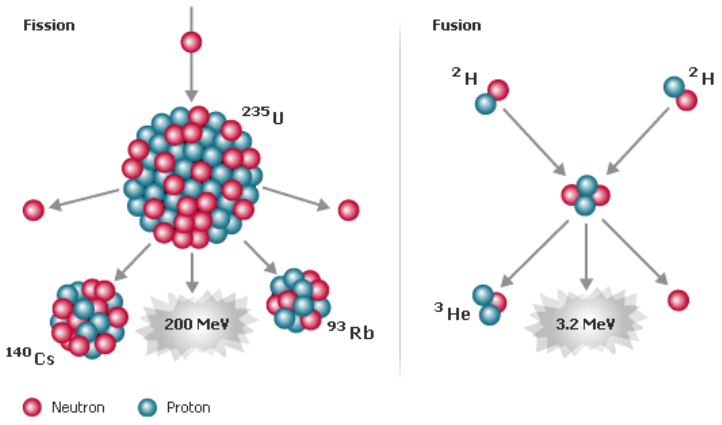

Figure 1.4 Schematic representations of a fission reaction (left) and a fusion reaction (right).

Unlike in the fission energy, fusion energy consists on the union of light atoms nuclei which lead to a final atom with less mass than the sum of the former ones, as shown in figure 1.4. This exceed of mass is transformed into energy following the expression $E = (\Delta m)c^2$.

In order to overcome the electrostatic repulsion of the atoms, high energies (temperatures of around 100 millions degrees) are needed. These temperatures are possible in the core of massive stars like the sun due to the high gravitational pressure achieved. However, it is expected to obtain these temperatures on the earth by means of fusion experimental devices.

From the point of view of the commercial fusion reactor, the most interesting reaction is formed by the deuterium ^{2}D and tritium ^{3}T (D-T) (figure 1.5),

$$^{2}D + {}^{3}T \rightarrow {}^{4}He + n + 17.5MeV \tag{1.1}$$

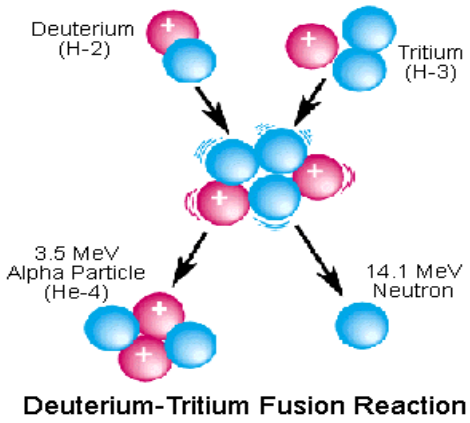

Figure 1.5 Schematic representation of a D-T fusion reaction [ITE05].

In this reaction, the deuterium and tritium atoms fuse to produce an alpha particle ^{4}He (helium nuclei) and a neutron. Both, the deuterium and tritium, are isotopes of the hydrogen. The deuterium is stable, inexpensive and pretty abundant on earth, since is present in the sea water with concentration 0,034g/l. The tritium does not exit naturally on earth but can easily obtained by using the lithium as absorber of the neutron produced by the fusion in the following fission reaction,

$$n + {}^{6}_{3}Li \rightarrow {}^{4}_{2}He + T \tag{1.2}$$

Taking account the fact that lithium is available worldwide, the source for the tritium is guaranteed.

In this reaction no direct radioactive waste is produced. However, the neutron can activate the surrounding wall of the reactor. Thus, a challenge in the fusion research field is

to find materials with low activation rates. Anyway, these radioactive wastes are 10 times less radioactive than the ones produced in a fission reactor [Con90].

There are other possible fusion reactions as the deuterium-deuterium (D-D),

$$^2D + {}^2D \rightarrow \begin{cases} {}^3He + n + 3.27MeV \ \ (50\%) \\ {}^3T \ + \ n \ + 4.03MeV \ \ (50\%) \end{cases} \tag{1.3}$$

This reaction has the advantage of not using tritium as fuel and not producing an energetic neutron, however, the temperature needed to make this reaction possible is up to 10 times higher than the one needed for the D-T reaction. Thus, D-D reaction would be feasible and desirable for a second generation fusion energy reactor.

Finally, another fusion reaction is possible, deuterium-helium3 (D-^{3}He),

$$^2D + {}^3He \rightarrow {}^4He + p + 18.35MeV \tag{1.4}$$

which is very interesting since it does not use tritium, and does not produce any neutron, however, it has some clear drawbacks, as the high temperatures needed and the lack of ^{3}He on earth (unlike on the moon, where it is pretty abundant).

1.3 Controlled fusion energy strategies

The final goal of the controlled fusion energy on earth is to make this kind of energy commercial competitive with the rest ones. In order to achieve this objective, fusion energy must be self sustained, or in other words, the plasma combustion must be maintained by means of the energy produced by the plasma itself. Two main scientific strategies have been developed: inertial confinement and magnetic confinement.

In the inertial confinement, a small capsule composed by deuterium and tritium is compressed by means of laser beams. When the capsule has a critical density, some fusion reactions are present in the core, leading to more reactions at the plasma surrounding. This configuration has extremely low confinement time. A major drawback of this type of magnetic controlled fusion experiments is that the accuracy of the beams must be extremely high to compress the capsule in a homogeneous way.

In the magnetic confinement, since the plasma consist of two types of charged particles, ions (atoms nuclei) and electrons, the plasma is confined by means of high magnetic fields. In this situation, the particles spiral along the magnetic field lines. The

confinement time achieve in this configuration can be quite long. This type of controlled fusion experiment is the most understood nowadays.

1.3.1 Magnetic confinement

Magnetic configurations can be divided into two main categories: open and closed configurations. In the open configurations magnetic filed lines are not closed in the space where the plasma is confined. In this situation, the magnetic field is gradually increased between two mirror points and particles cannot escape.

The closed magnetic configuration consists mainly on toroidal devices ("doughnut" shaped) in which the plasma is confined by the magnetic field. This magnetic field is formed by a toroidal component (in the direction of the torus) and a poloidal component. The toroidal component is induced by the external coils of the experiment device. In order to get the poloidal component of the magnetic field two strategies are available. First, it can be generated by the plasma itself by inducing an external current. Second, it can be generated by external coils. Depending on the way this poloidal component is generated the corresponding magnetic confinement device may has two different names: tokamak or stellarator.

1.3.1.1 Tokamaks

In tokamaks, poloidal magnetic field is generated by inducing an external current on the plasma. By adding this component to the toroidal component generated by the external coils (figure 1.6) the total magnetic field necessary to confine the plasma is obtained.

It is worth to point out that due to this configuration the tokamak has non continuum pulsar behaviour. This is the principal drawback of this design; however, several methods are being studied in order to avoid this difficulty, e.g. using the electron cyclotron resonant heating or the neutral beam injection as non-induced current generators.

1.3.1.2 Stellarators

In this configuration, the magnetic field is completely generated by the external coils, thus, no induced current is necessary. This feature allows a continuum working regime of the stellarator device (figure 1.7). This fact, which is an advantage over the tokamak concept, also leads to some important difficulties. The principal is that the magnetic field must be calculated with high accuracy since any deviation may lead to the plasma loss of

confinement. Other important drawback is that neoclassical transport is quite enhanced in stellarators configurations. In order to avoid this fact, quite large aspect ratio devices have been constructed. However, some new studies suggest the possibility of low aspect ratio compact stellarators with low neoclassical transport. More information about this subject will be discussed in chapter 2.

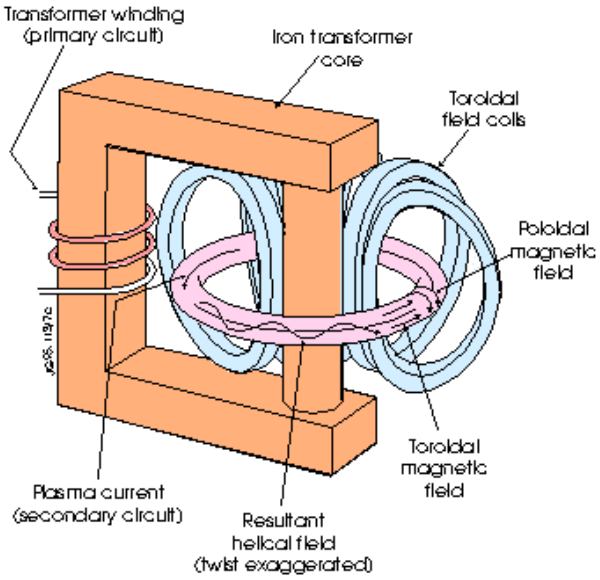

Figure 1.6 Schematic representation of a tokamak fusion device [EFD05].

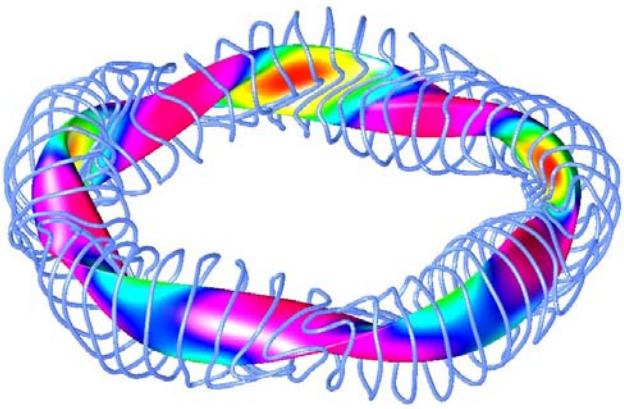

Figure 1.7 Schematic representation of the coils and the magnetic surfaces of the stellarator fusion device W7-X [IPP05].

1.4 Fusion energy future

1.4.1 Fusion energy highlights

Since the construction of the first fusion experimental devices many improvements have been discovered and applied in order to get better performances. As can be see from figure 1.8, fusion energy obtained in the last 30 years has grown in a spectacular way, even compared with the increase of computational power capability of the computers. Moreover, net fusion power has been obtained already, 10.7 MW were obtained in TFTR (1994) and 16 MW in JET (1997), leading in this last case to Q=0.6. In addition, really long pulses have been obtained in the last years, as has been shown in Tore-Supra and LHD where, by means of superconducting coils, 30 minutes discharges have been obtained. These long discharges allowed establishing new records of stored energy in LHD (1.3 GJ). All these facts seem to demonstrate the viability of fusion as net energy source.

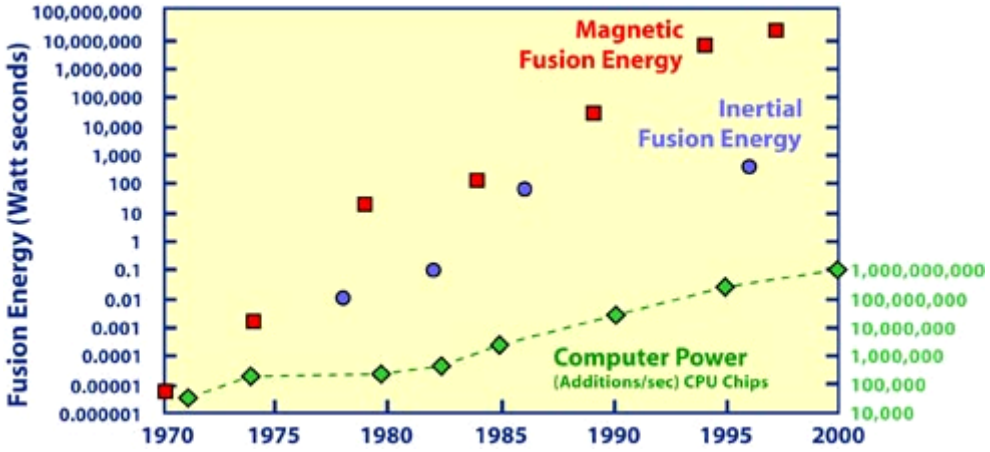

Figure 1.8 Evolution of the fusion energy obtained and the computer power capability in the last 30 years [PPP05].

In spite of these important achievements a next-step is needed in order to completely demonstrate fusion viability before the final design of the commercial fusion reactor. This next-step is ITER.

1.4.2 ITER

ITER is the fusion experimental device which should demonstrate the viability of fusion as primary energy source. In order to achieve this main goal, ITER device should be

able to maintain D-T reactions in conditions close to the ignition and the steady-state. However, as a first step, instead of steady-state, inductive scenarios with high inductive current are preferred, since at the present time, these scenarios are the most studied in the present tokamak devices. A summary of main ITER parameters in the inductive working regime is given in table 1.2. Once this working regime is fully operational, more sophisticated and promising working regimes as the steady-state (with internal transport barrier and around 80% of non-inductive current) and hybrid scenarios (a mixture of inductive and steady-state with around 50% of non-inductive current) could be investigated.

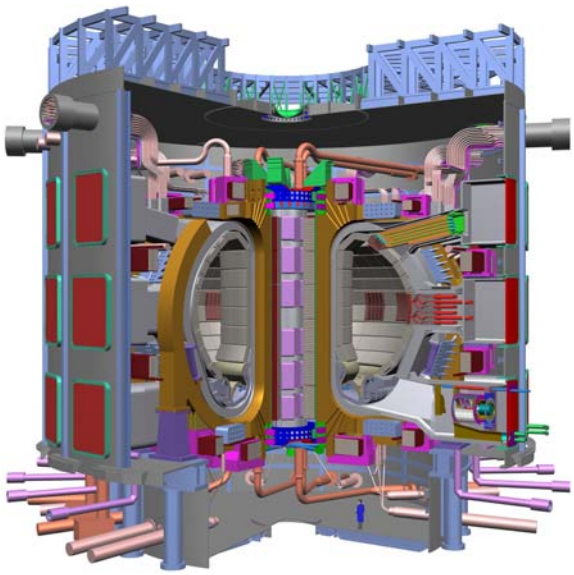

Figure 1.8 Schematic representation of ITER main building [ITE05].

Parameter	Value
Major radius (m)	6.2
Minor radius (m)	2.0
Plasma volume (m^3)	840
Current (MA)	15.0
Toroidal field on axis (T)	5.3
Fusion power (MW)	500
Burn flat top (s)	>400
Power amplification	>10
Elongation/triangularity	1.9/0.40

Table 1.2 Main parameters and dimensions of ITER [ITE05].

	Issue to Solve	JET-class machine	ITER
1	Stable effective plasma confinement scheme	Confirm, optimise, seek promising new directions	Confirm and optimise at new scale
2	Heat plasma to burn temperature	Examine performance of options	Find optimum and efficient performance mix
3	Plasma control in steady state	Examine options for achievement	Demonstrate schemes and maximise performance
4	High temperature tritium-breeding blanket	Not tested	Test components and develop materials in parallel
5	Remote replacement	Test methods	Deploy in reactor-realistic situation
6	Safety and environmental acceptability	Hardly an issue	External tritium supply, large waste arising, minimise environmental impact
7	Economic viability	Not relevant	Relevant for most costs, used to point to directions for minimisation
8	Divertor operation and plasma purity	Develop underlying understanding	Demonstrate control and performance
9	High heat flux components	Develop underlying understanding	Demonstrate technologies and engineering design
10	Superconducting magnets	Used only in two smaller concurrrent experiments	Demonstrate manufacturing feasibility, performance and reliability
11	Low activation materials	Under development in concurrent underlying programme	Some properties measured on ITER components and others in materials test facility
12	Reliability	Shot reliability maximized	Demonstrate highly reliable performance for short periods (~ 2 weeks)

Table 1.3 Main challenges to be overcome by ITER [ITE05].

ITER should demonstrate, as an inherent part of its initial design and operation, adequate solutions to the challenges that the actual tokamak devices have not been able to overcome. A list of these challenges is given in table 1.3. In particular, 1, 2, 3, 5, 8, 9 and 10 can be used in any subsequent commercial deployment of tokamak-based fusion power. During its operating life, ITER will test and confirm design solutions for 4 (tritium-breeding blankets). ITER provides the only good opportunity to identify the best engineering solutions to generate sufficient tritium fuel in a realistic fusion reactor environment with minimum contamination of the high grade coolant needed for steam generation. However, due to ITER's relatively low power level, the testing will take a considerable time - about 15 years of machine operation. ITER can be run to end of life

using externally supplied tritium (removed e.g. from heavy water coolant coming from some fission reactors), but all the subsequent machines must rely on tritium generated by themselves.

In answering these challenges, ITER will also have demonstrated that it can answer challenge 12, although it will not demonstrate the long term high availability necessary for reliable electrical power production.

1.4.3 Beyond ITER

ITER has been designed to operate at nominal 500 MW fusion power. However, if the future commercial reactor must have a similar size, its fusion power must be around 4 times higher, leading to 500 MW electrical power delivered to the network. Therefore, heat fluxes to the wall will be 4 times higher too, and global performance should be improved by a factor 4. Some studies have shown that density should be a 30% higher that the nominal for ITER to achieve this purpose. If these goals can be reached in the next-step device to ITER, namely DEMO, then DEMO itself may become the first prototype of fusion commercial reactor.

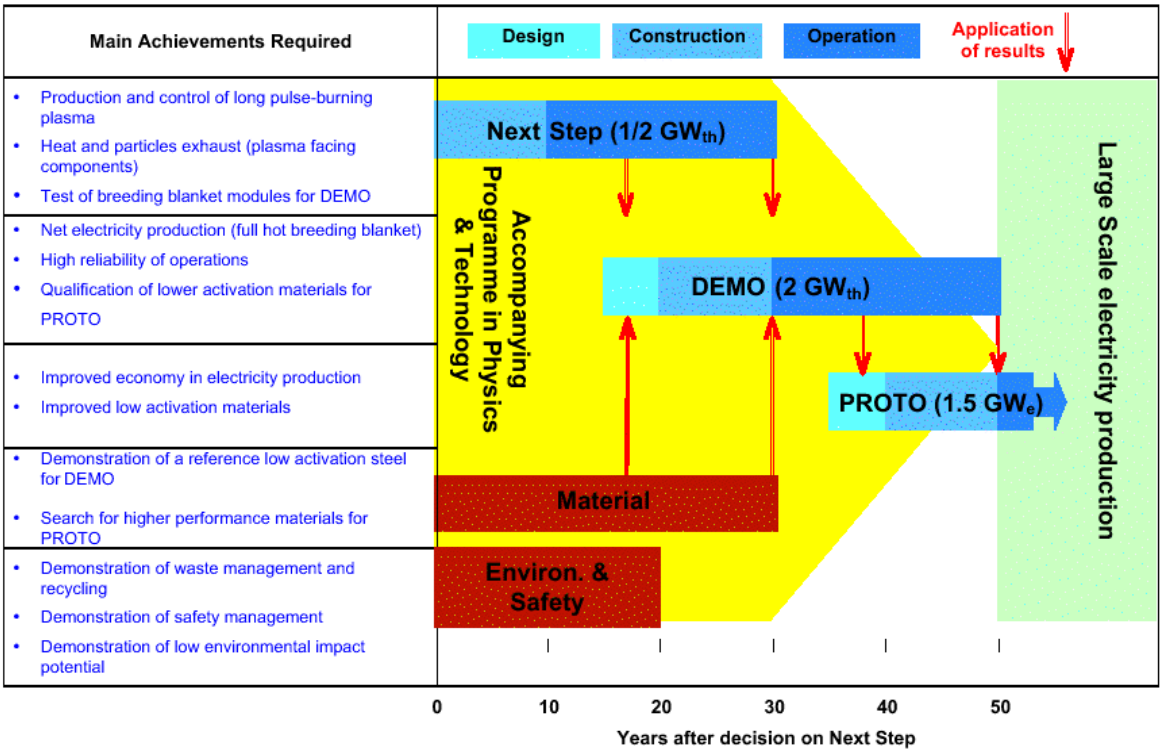

Figure 1.10 Roadmap to the commercial fusion reactor [ITE05].

This strategy could accelerate the purpose of having fusion energy commercial reactors (figure 1.10) 20 years, as has been specified in the called “fast-track”.

1.5 Summary

It has been shown that the actual population growth rate is the crucial factor that leads to a drastic change in our energy culture. Such growing rate will imply higher levels of energy demanding as well as higher atmospheric contamination due to CO2 if the actual dependence on fossil fuels is maintained. In order to avoid these perspectives few possibilities arise. Renewable energies seem far from being able to sustain human energy necessities. On the other hand, although nuclear fission respects Kyoto protocol, needs political agreement to be considered as a solution.

In this situation nuclear fusion appears as a primary energy source that overcomes the difficulties previously pointed. Particularly important is the D-T fusion reaction, which needs temperatures that, at the present time and taking account the future construction of ITER, are possible to achieve.

However, it is worth to point out that the final goal of fusion studies is to provide knowledge enough to the scientific community in order to have commercial fusion reactors as soon as possible. It is also worth to keep in mind that, not just scientific efforts are needed to make this “dream” possible, but worldwide government’s efforts providing sufficient money are also needed.

Chapter 2

LHD and TJ-II devices description

2.1 Introduction

The stellarator fusion device concept is an alternative to the more classical tokamak device. One of the most important advantages of this design is that it allows free disruption fusion plasma devices. This feature could make stellarator reactors an attractive fusion concept due to the inherent lack of instabilities. Nowadays, research in stellarator plasmas is particularly important at the Large Helical Device (LHD), where quite long shots have been obtained.

The stellarator concept is not just important for future commercial reactor design but for plasma physics itself, since, although tokamaks and stellarators share many physical processes, there are some particular events that are typical of stellarator devices. An example could be the Internal Transport Barrier scenarios, which are generated by electric field in stellarators and magnetic field shear in tokamaks.

2.2 Stellarators characteristics

2.2.1 Differences between tokamaks and stellarators

Stellarators are fusion devices with many similarities compared with tokamak ones. However, important differences arise between both concepts; perhaps the most important one is the way the magnetic field is generated. In the tokamak case, a current must be induced in the plasma in order to obtain the poloidal magnetic field, whereas in the

stellarator case, magnetic field is completely generated by the external coils. Due to the fact that the coils position must be completely determined to obtain the desired plasma equilibrium, another important difference between tomakaks and stellarator arise, the lack of toroidal symmetry. This feature implies some physical processes characteristic of stellarators, as asymmetric neoclassical transport and radial electric field.

The lack of an induced current to obtain plasma equilibrium is important in order to design future steady-state fusion reactors, since in the tokamak case, more probable disruptions can be expected because of the difficulty to maintain the induced current in steady-state scenarios.

2.2.2 Stellarators magnetic configuration

Several stellarator designs have been developed (figure 2.1),

- Torsatrons (helias), with helicoidal coils and a shear similar to tokamaks. (LHD, CHS)
- Modulars, with asymmetric toroidal coils and low shear. (W7-AS, W7-X)
- Heliacs, with planar coils and low shear. (TJ-II).

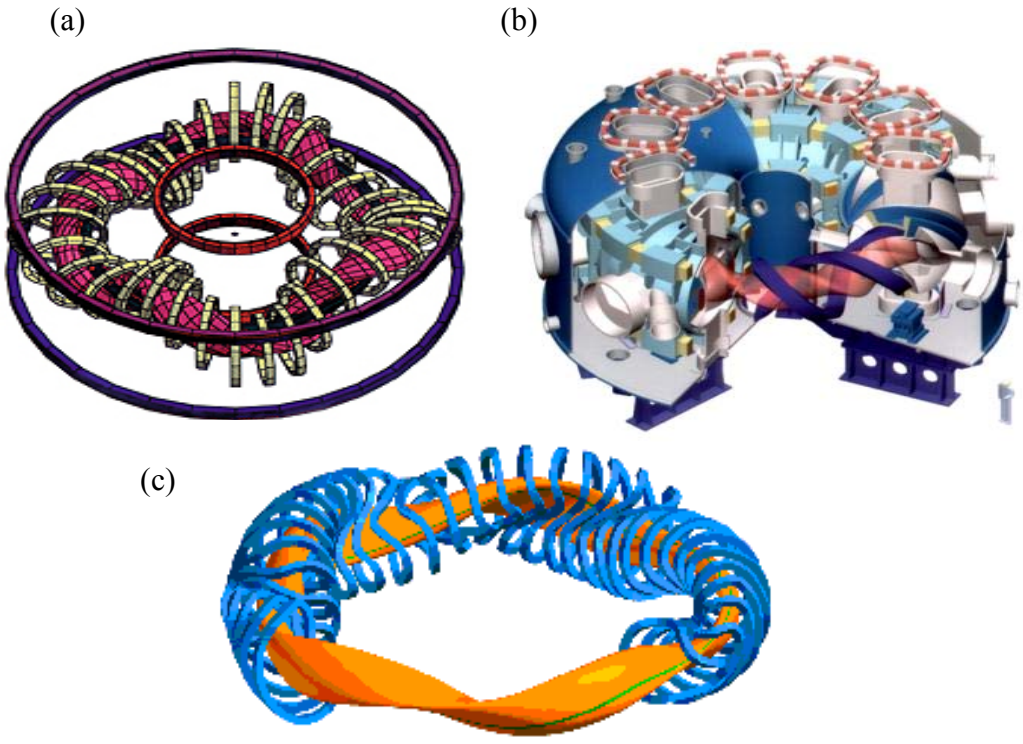

Figure 2.1 Schematic overview of different stellarators design: Heliac (TJ-II) (a) [CIE05], Torsatron (LHD) [NIF04] (b) and Modular (W7-X design) [IPP05] (c).

A summary of the main characteristics of W7-X, LHD and TJ-II devices is addressed in table 2.1

Parameter	W7-X	LHD	TJ-II
Magnetic configuration	Modular	Helias	Heliac
Number of periods	5	10	4
Major Radius	5.5 m	3.9 m	1.5 m
Average minor radius	0.5 m	0.5-0.65 m	0.12-0.2 m
Magnetic field	3 T	3-4 T	1 T
Plasma Volume	≈30 m^3	≈20-30 m^3	≈1.2 m^3
Additional power	≈14 MW		
ECRH		10 MW	≈0.6 MW
ICRH		14 MW	
NBI		15-20 MW	≈4 MW
Shot length	<30 min	≈ 30 min	0.5 s

Table 2.1 Main characteristics of the W7-X, LHD and TJ-II stellarator devices.

2.2.3 Advanced research in Stellarators magnetic configuration

Advanced research in the stellarator concept is being carried out at the present time in order to obtain the best designs for the future fusion commercial reactor. This commercial reactor must have some crucial requirements (better choice in the brackets)[Yam04b]:

- Steady State Operation at high Beta (β >4%, f_{BS}>70%) (Stellarator)
- Free from Disruptions (Tokamak/Stellarator hybrid)
- Divertor Solution (Mirror Type)
- Compactness/Low Cost (Spherical stellarator)
- Simple System/ Easy Maintenance (Simple coil)

These characteristics make the decision of what magnetic configuration is the most convenient quite difficult. The stellarator concept is an ideal choice in order to have a steady state reactor, free of disruptions, however, a commercial reactor based in the LHD design would be to large (in order to have a large aspect ratio, which minimize neoclassical transport) and expensive [Yam04], hence a more compact design must be studied in order to reduce costs. Several compact stellarators are being currently designed. These stellarators, with plasma aspect ratios 1/2 to 1/3 that of conventional stellarators, are quasy-

symmetric confinement devices that have helical magnetic field lines similar to those in tokamaks and conventional stellarators, but the confining poloidal magnetic field is created by both the plasma-generated internal "bootstrap" current and currents in external coils. Neoclassical transport can be minimized in these low aspect ratio devices by introducing a new symmetry in the general 3-dimensional dependence of the magnetic field in stellarators $B = B(\psi, \theta, \varphi)$, to a 2-dimensional dependence of its modulus $|B| = |B|(\psi, \zeta)$ [San05b]. This new symmetry of the magnetic configuration makes these devices similar to tokamaks. Some of the proposed designs are the following,

- Quasi-axisymmetry (QA), which uses the bootstrap current to produce most of the poloidal field and has tokamak-like (Figure 2.2, left).

- Quasi-omnigeneity (QO), which approximately aligns bounce-averaged drift orbits with magnetic surfaces and aims at a smaller bootstrap current (Figure 2.2, right).

- Quasi-helically symmetric (QH) approach, which produces configurations with high effective rotational transform, small deviations from a magnetic surface, and little bootstrap current.

- Quasi-poloidal (QP) approach, is a compact (A = 2.7) two field period with quasi–poloidally symmetry.

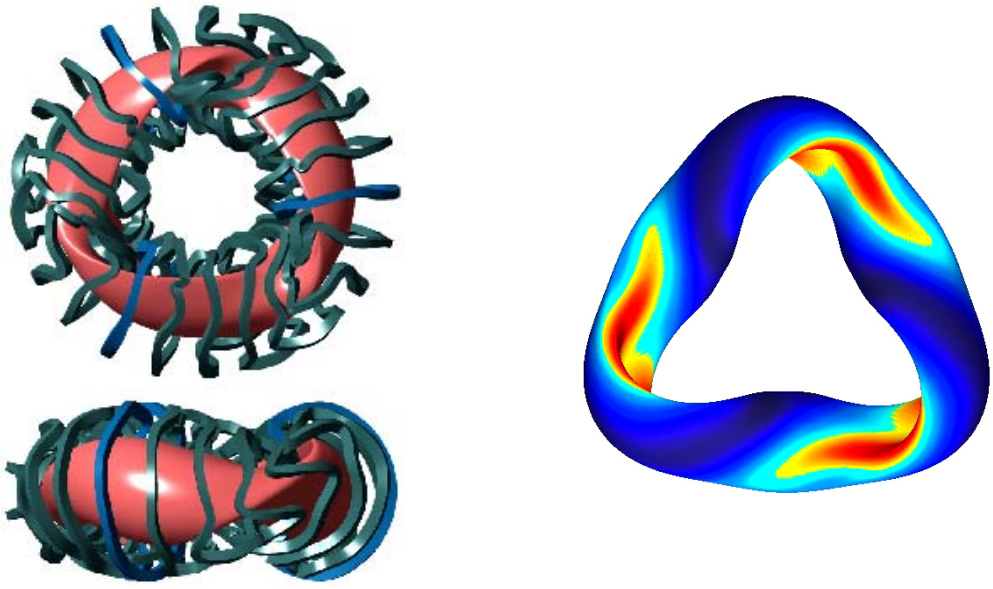

Figure 2.2 A modular coil set for the QA plasma configuration (left)[Lyo00]. Plasma shape for a QO three periods compact stellarator (right) [Yam04b].

Another example of new concept is the spherical stellarator (SS). The Spherical Stellarator (figure 2.3) is an advanced concept for controlled nuclear fusion. It represents a low-aspect-ratio compact stellarator approach that uses plasma current (bootstrap current, at high plasma pressure) to achieve a significant part of the rotational transform as compared with that produced by the stellarator's coils. This concept is most advantageous at low plasma aspect ratios A < 3.5. The SS concept emphasizes effectiveness of the plasma (bootstrap) current in reaching high plasma pressure operation and improved confinement. On this way, compact stellarator configurations with extremely low aspect ratios approaching to 1 were found with the following characteristics [SST05],

- Very compact stellarator design, making it inexpensive to construct and operate
- Very high plasma pressure regimes of operation (comparable to that for spherical tokamaks)
- Steady-state operation with advanced regimes could be fully supported by a self-induced bootstrap current, at high plasma pressure
- Enhanced particle and energy confinement in the plasma
- High ratio of plasma volume, V, to plasma surface area, S (a corresponding dimensionless parameter might be V/RS)

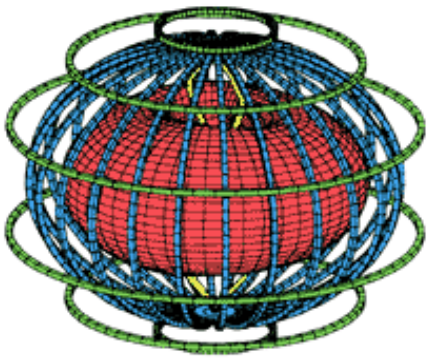

Figure 2.3 Schematic view of the spherical stellarator fusion device [SST05].

These designs may overcome some issues of the former stellarator concept by improving neoclassical transport, improving confinement, obtaining β larger than 5%, demonstrating disruption-free operation at high β and reducing costs.

2.3 LHD characteristics

The Large Helical Device (LHD), figure 2.4, is a torsatron (helias) device that produced first plasmas in 1998. One of the main goals of the LHD is to demonstrate the possibility of long steady-state plasmas with no disruptions in stellarators devices. Due to the necessary continuum-working regime of the future fusion commercial reactors this is a very important issue. Thus, in order to reach this objective, it is planned to increase the strength of confinement magnetic field, to boost heating power and to extend operation time. These efforts will lead to elucidation of the physics of steady-state currentless plasma. Some other goals of the LHD are to study the physics and engineering issues in helical devices and compare the results with other stellarator and tokamak devices, studies of plasmas with high triple product $n\tau T_i$ and high β in order to store as energy as possible. The highest β obtained is 4.1% with B_t=0.45T and stored energy of 1MJ.

Three poloidal coils and one helicoidal coil (superconducting coils), figure 2.5, generate the necessary magnetic field. A summary of the main characteristic of these coils is shown in table 2.2. The standard configuration of the LHD plasmas has minor radius 0.6m and magnetic field strength 3T, although because of the installed coils, a wide configurations range can be obtained. In order to have a global vision of the LHD, a schematic overview is given in figure 2.6.

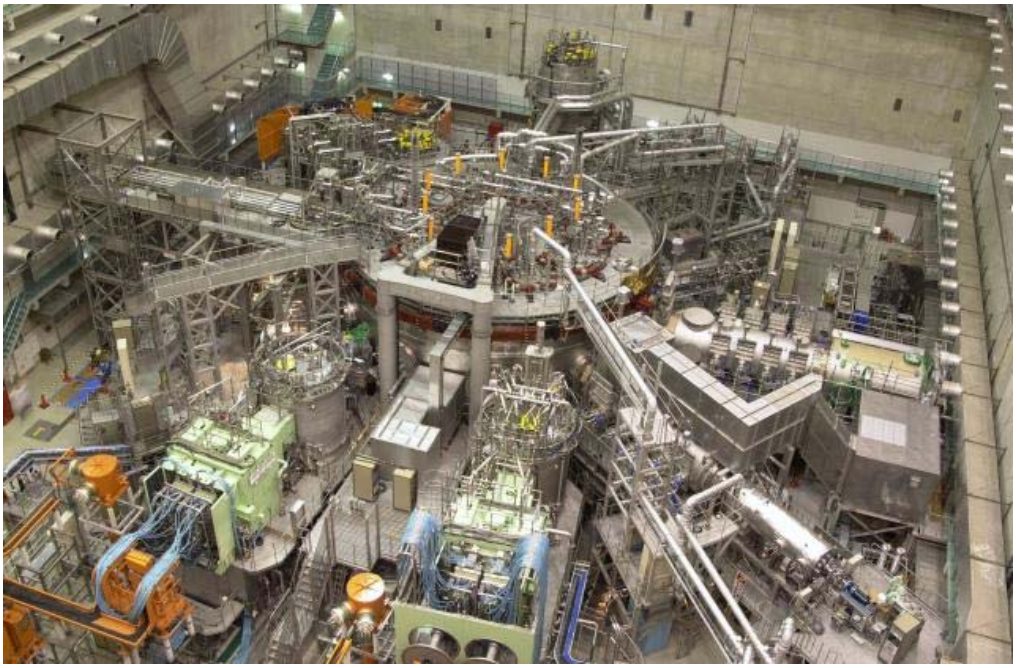

Figure 2.4 Overview of the LHD and the auxiliary systems [NIF04].

	IV coil	IS coil	OV coil	HELICAL coil	
Diameter (inside)	3.2m	5.4m	10.4m	Major radius	3.9m
Diameter (outside)	4.2m	6.2m	11.6m	Minor radius	0.975m
Weight	16ton	25ton	45ton	65ton	
B max	6.5T	5.4T	5.0T	6.9T	
Current	20.8kA	21.6kA	31.3kA	13kA	17kA
Turn number	240	208	144	450	

Table 2.2 Poloidal and helical coils characteristics (Inner Vertical coil, Inner Shaping coil, and Outer Vertical coil). The current in the helical coil has two maximums depending on the phase [NIF04].

As it was described previously, LHD has superconducting helical coils, which are presently cooled with liquid helium at 4.4K (-268.8°C). Sub-cooled liquid helium of 3K and/or pressurized super fluid helium of 1.8K will be used in the future to increase the achievable magnetic field so that the better plasma performance will be obtained. For this purpose, research in superconductors cooled by sub-cooled liquid helium is being increased. An advanced current lead system using high temperature super conductors is also being developed for the future higher current applications.

Figure 2.5 LHD helical coil [NIF04].

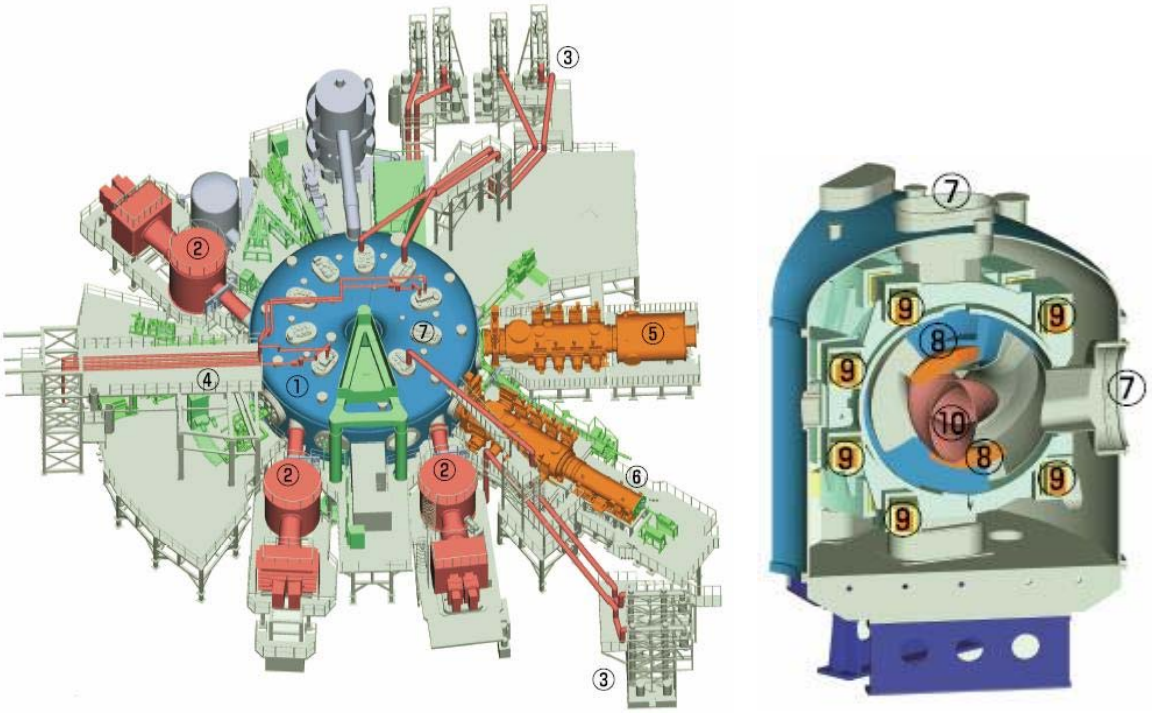

Figure 2.6 Schematic overview of the LHD and its auxiliary systems (a). Sectional view of the LHD (b). The number descriptions are given in table 2.3 [NIF04].

Number	Description
1	LHD
2	Neutral beam injection heating device
3	Ion cyclotron range-of-frequency heating device (coaxial conduit for power transmission and stub tuner)
4	Electron cyclotron heating device (waveguide for power transmission)
5	Local Island Divertor (LID)
6	Vacuum pumps
7	Diagnostic ports
8	Superconducting helical coils
9	Superconducting poloidal coils
10	Plasma

Table 2.3 Number description of figure 2.6.

Three heating methods are being applied to attain higher temperature plasmas required for nuclear fusion reactions. These methods are neutral beam injection (NBI), which injects electrically neutral high-energy particles; ion cyclotron range-of-frequency (ICRF） heating and electron cyclotron resonance heating (ECRH), which resonantly heat ions and electrons in a plasma by radio frequency waves or millimetre waves respectively. Research for higher power injection technique and optimisation of absorption in plasmas is under way.

Since 1998, many LHD improvements (e.g. higher heating power) allowed to reach higher electron and ion temperatures, β, stored energy, triple product and confinement time. A summarize of the LHD main results is given in table 2.4. As can be seen, maximum electron temperature achieved, 10 keV, was obtained in a very low density regime. These scenarios are said to have electron Internal Transport Barrier (eITB), and their main characteristic is high peaked electron temperature profiles (figure 2.7 left). Maximum ion temperature measured is about 7 keV (figure 2.7 right), and it was obtained with a newly operated Ne glow discharge cleaning. The increase in the NBI absorption power by Ar gas puff and the increase in the NBI heating power up to 10MW also contributed to the high ion temperature.

	Electron temperature	**Ion temperature**	**Confinement time**	**Inject. power**	**Average electron density**
$T_{e,\max}$	10keV	2.0keV	0.06s	1.2MW	$5.0\text{x}10^{18}\text{m}^{-3}$
$T_{i,\max}$	4.2keV	7.0keV	0.06s	3.1MW	$2.9\text{x}10^{18}\text{m}^{-3}$
$\tau_{\max}$	1.3keV	1.3keV	0.36s	1.5MW	$4.8\text{x}10^{19}\text{m}^{-3}$
$n\tau T_i$	$2.2\text{x}10^{19}\,\text{keVm}^{-3}\text{s}$				
$W_{\max}$	1.16MJ				
$\beta_{\max}$	β =4.1% at B_t=0.45T				
$n_{e,\max}$	$1.6\text{x}10^{20}\text{m}^{-3}$				

Table 2.4 LHD main results [NIF04].

As previously mentioned, one of the mail goals of the LHD is to sustain plasmas with high triple product for a long time in order to demonstrate the helical devices capability to be the next-step commercial reactor. A significant progress is two-minute discharges by ICRF, in which electron density is $0.8\text{x}10^{19}\text{m}^{-3}$ and electron and ion temperatures are both

1.2keV has been achieved. High density plasmas are sustained by 2MW NBI power for 10 seconds and plasma shots over forty seconds can be repeated every nine minutes. However, nowadays even more spectacular results have been obtained. A long 31min 45s discharge has been obtained in the 2004 campaign by using ICRF heating (700kW) and B_t=2.75 T. Electron and ion temperatures obtained were 2 keV and average electron density was sustained at $0.8x10^{19}m^{-3}$. With these features a new energy stored world record, 1.3 GJ, was established. These facts lead to the conclusion that helical devices can be a good choice as the next step reactor design.

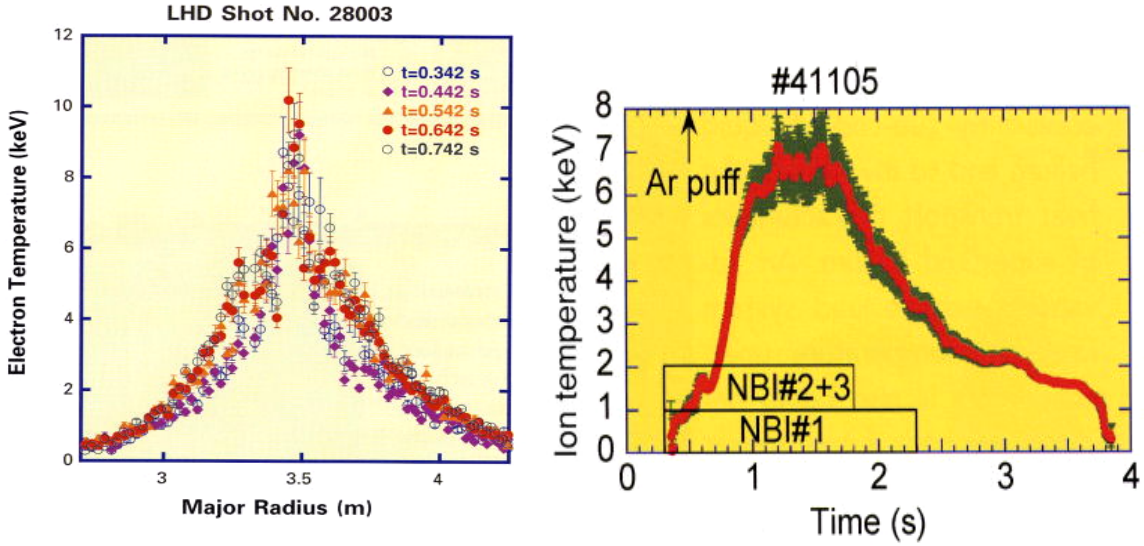

Figure 2.7 Electron temperature profile with eITB (left). Maximum central electron temperature achieved is 10 keV. Central ion temperature time evolution (rigth). Maximum temperature, 7 keV, is achieved by using NBI heating [NIF04].

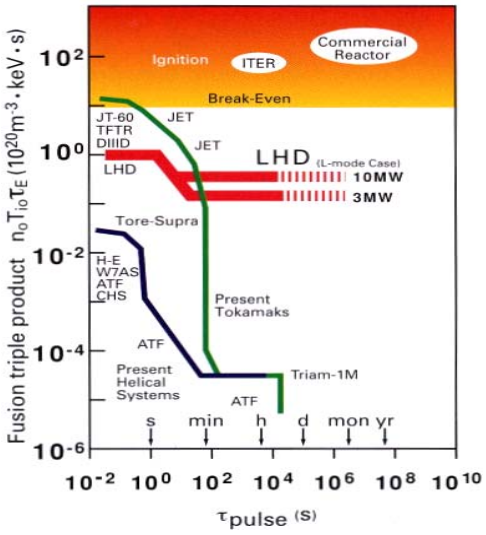

Figure 2.8 Comparison between the fusion triple product of different fusion devices and the LHD [NIF04].

Finally, a comparison between several magnetic fusion devices and the LHD is addressed in figure 2.8. As can be seen from the figure, LHD fusion triple product results are comparable to that obtained in similar tokamaks devices. Besides, by increasing the heating power (mainly in the ion channel) higher results can be obtained. However, a commercial reactor based on a helical device is far from being as attractive as tokamak design, because of the large major and minor radius needed to obtain enough alpha power.

2.4 TJ-II characteristics

TJ-II stellarator [Ale90] is the most important fusion project in Spain. It was started in 1986 when the "Asociación Euratom-CIEMAT para Fusión" was created. The first step was the presentation, before EURATOM was established, of the flexible heliac project TJ-II, directed towards demonstrating its scientific interest (Phase I). In 1990 EURATOM decides financing 45% (preferential support) of the TJ-II project when its technical viability is demonstrated (phase II). In 1997, the TJ-II construction is over, and firsts plasmas are confined.

Main goal of the TJ-II experiments are to study the physics of stellarator devices. As these experiments depend strongly on the heating method available, three scientific stages have been defined [CIE05],

- **Stage I:** ECH system

  - Consisting of 2 gyrotrons working at second harmonic 53.2 GHz
  - Injected power <= 1 MW.
  - The expected plasma values with this heating are: $n_e(0) \sim 1.7 \times 10^{19}$ m^{-3}, $T_e(0) \sim$ 1.0 - 1.5 keV, $T_i(0) \sim 300$ eV, $\tau_E \sim 4$ ms

- **Stage II:** Neutral Beam Injection system

  - Two co/counter NBI lines
  - Injected power <= 3 MW.
  - The expected plasma values with this heating are: $n_e(0) \sim 10^{20}$ m^{-3}, $\beta(0) \sim 3$ %, $\tau_E \sim 6$ ms.

- **Stage III:** Consists of 3 MW additional power.

The former TJ-II device heating method was ECR heating (stage I) but since 2003 NBI heating is also available (stage II). Stage III definition depends on the results obtained with NBI heating and the experience from other fusion devices. Anyway, is expected to achieve the TJ-II beta limits with stage III.

According to these three stages a four points scientific programme has been developed,

- **Confinement studies:** These studies are done to clarify what variables are important to get high confined plasmas.

  - Magnetic surfaces and magnetic field fluctuations

  - Confinement dependence on the rotational transform
  - Plasmas with low collissionality
  - Fast particles
  - Far from equilibrium plasmas
  - Particle transport

- **Electronic kinetic processes:** The kinetic processes induced by ECR heating are studied. It can help to study this heating method.

  - Induced current by ECR heating studies
  - Power deposition

- **Fluctuation studies:** These studies are focused in instabilities processes.

  - Electron temperature fluctuations mechanism
  - Magnetic turbulence
  - Non-stationary processes
  - Non-local transport

- **Wall-plasma interaction:** These studies are focused in understanding the key processes in the wall-plasma interaction.

The toroidal field necessary is produced by 32 coils (figure 2.9). The tree-dimensional twist of the central axis of the configuration is generated by means of two central coils: one circular and one helical. The horizontal position of the plasma is controlled by the vertical field coils. The combined action of these magnetic fields generates bean-shaped magnetic surfaces that guide the particles of the plasma so that they do not collide with the vacuum vessel wall.

In addition to the toroidal and helical coils some other coils have been added to control the plasma: two vertical field coils to position the magnetic axis, four ohmic coils able to generate 0.1 V e.m.f. indented to cancel possible spurious toroidal currents and four radial coils which produce a trimming radial fields up to 100 G aimed at compensating stray fields. A summary of the main coils characteristics can be found in table 2.5.

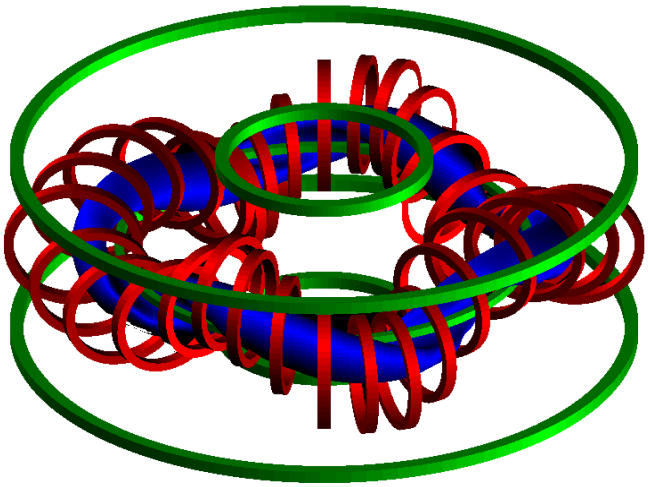

Figure 2.9 Schematic overview of the TJ-II. Helical coils are represented in green, toroidal coils in red and plasma in blue [CIE05].

Coils	Radius (m)	Nr. Turns	Current (A) in 1 turn
CIRCULAR	1.5	24	11700
HELICAL	1.5	24	10800
TOROIDAL 32 coils (4 enlarged/28 normal)	0.475/0.425 (enlarged/normal)	9/8 (enlarged/normal)	32500
VERTICAL 2 coils	2.25	16	12500
COMPENSATION 4 coils (2 inner/2 outer)	0.78/2.29 (inner/outer)	20/1 (inner/outer)	7200
RADIAL 4 coils (2 inner/2 outer)	0.74/2.24 (inner/outer)	7/5 (inner/outer)	5200

Table 2.5 TJ-II helical, toroidal and auxiliary coils description [CIE05].

Last experimental campaigns of TJ-II stellarator have been focused in studying the influence of radials electric fields on electron temperature, density and confinement. Besides, magnetic topology influence on electric field has been studied too. Some of the main recent results are the following,

Plasma density scan experiments: Plasma confinement dependence on density and rotational transform has been found. Rotational transform dependence is compatible with

ISS95 scaling, however, density dependence is slightly different. Electron thermal diffusivity dependence on rotational transform has been found too.

Density scan experiments performed in TJ-II have shown that the radial electric field tends to be negative in the plasma edge as density increases above the critical value. Near the critical density, where the sheared flow is developed, the level of edge turbulent transport and the turbulent kinetic energy significantly increases. The resulting sheared flow is close to the one required to reduce turbulent transport (as measured during biasing induced improved confinement regimes), proving that spontaneous sheared flows and fluctuations are near marginal stability

Evidence of non-diffusive transport mechanisms has been also observed in particular during the propagation of edge cooling pulses, leading to the called ballistic transport. In order to clarify the underlying physics of non-diffusive transport, a one-fluid transport model in which the usual Gaussian distributions are generalized to Lévy distributions has been developed. This physics framework yields to long correlations in these plasmas, which have been experimentally checked in other stellarator devices.

Magnetic topology studies: Electron internal transport barrier formation has been found when a low order rational surface is close to the plasma core region ($\rho \approx 0.2 - 0.3$) either with negative or positive magnetic shear. Steeped electron temperature profiles are formed in the plasma core, as well as high positive electric fields (about three times higher than with no low order rotational surfaces) while in the outer plasma the electric field remains unchanged. This feature has been also found in other stellarator devices, as in the LHD case.

On- and off-axis ECH plasmas: Several experiments have been carried out in order to study the influence of the heating deposition profile on impurity transport. The results show significant changes in impurity confinement when on-axis heating is changed to off-axis ECR heating. A transport analysis is in progress to obtain deeper knowledge about the mechanisms responsible for these effects.

NBI heated plasmas: Nowadays, NBI discharges with reasonable density control of up to 130 ms duration have been obtained. A fast drop of both central plasma potential measured by HIBP and edge turbulence transport is observed in pure NBI plasmas, while a gradual modification of core plasma potential and no change in edge turbulence transport is found in NBI + off-axis ECH plasmas. The behaviour of the plasma ions and impurities has also been studied at the transition between ECH and NBI regimes. An important fact is

that ion temperature as measured by a Neutral Particle Analyzer shows non-Maxwellian spectra with a first slope that evolves from 90 eV under ECH to around 130 eV under NBI. However, a better performance in NBI heated plasmas is expected in future campaigns having higher NBI power and higher density target plasmas heated by Electron Bernstein waves.

2.5 Summary

Stellarator research is very important subject because of some special characteristics of this fusion concept. Unlike in the tokamak case, continuum free discharge regime is expected in stellarator discharges. This fact is a key issue for the next step commercial fusion reactor, since electricity must be generated with no disruptions. Besides, plasma physics research in stellarators is quite important by itself, since many differences arise from different fusion devices. For example, internal transport barrier formation seems to be quite different in tokamaks and stellarators. In the first case magnetic field shear seems to play an important role, however, in the stellarator case, low density and low rational surfaces locate in the plasma core can suppress anomalous transport.

Two stellarator devices (LHD and TJ-II) have been selected in this thesis in order to study specific electron heat transport characteristics of stellarator plasmas. These two devices, although being similar in many aspects, generate the necessary magnetic field in a very different way. In the LHD case, a superconducting helical coil together with some toroidal coils generates the magnetic field lines. This type of stellerator configuration is called helias. In the TJ-II case (Heliac), toroidal planar coils and some auxiliary coils are necessary.

The LHD is, at the present time, the largest stellarator in the world. The main goal of the LHD team is to obtain plasmas with high triple product in order to demonstrate the possibility of future commercial reactors based on a helias design. With this aim, some spectacular results have been obtained, e.g. maximum central electron temperature achieved is 10 keV, maximum central electron temperature achieved is 7 keV, maximum β=4.1% at B_t=0.45T and maximum triple product is 2.2×10^{19} keVm^{-3}s. These values are in the range of some tokamaks devices with similar size and magnetic field. Long sustained shots have been also obtained in the LHD. In the 2004 campaign a long 31min 45s discharge has been obtained by using ICRF heating (700kW) and B_t=2.75 T. With these features a new energy stored world record, 1.3 GJ, was established. All these facts come to the conclusion that the studies on helias design must be carried out since this fusion concept is an attractive way to finally reach a commercial reactor.

The TJ-II device is one of the most important experiments in Spain. The main goal of the TJ-II experiments is to study the physics of stellarator devices and to compare with other similar devices. In the first campaigns, ECR heating was available, and eITB with high peaked electron temperature plasmas were obtained. Nowadays, NBI heating is also available and an increase in ion temperature is expected. Besides, experiments with higher average line density can be obtained. In the future, the TJ-II beta limits are expected to achieve with 3 MW of additional heating power.

Chapter 3

TOTAL and PRETOR-Stellarator transport codes description

3.1 Introduction

Understanding plasma physics is a challenge for the science community, since the processes involved comprise many different physics fields as thermodynamics, electromagnetism or hydrodynamics. In the resulting framework (and particularly, in the magnetic fusion field) the equations involved in the resolution of the main plasma variables are quite difficult to solve due to their high non-linear global structure. In this situation, transport codes are a powerful tool in order to solve the plasma equations obtained from physical theories. Moreover, from the analysis of the results obtained, the experimental data can be better understood and the experiments may be improved.

Another important purpose of the transport codes is to use the physical models already checked with experimental data in order to study and to predict the performance of future fusion magnetic devices. Without these tools, it would be quite difficult to design future commercial reactors as well as ITER.

Two transport codes, Toroidal Transport Analysis Linkage (TOTAL) and PRETOR-Stellarator, have been used throughout this thesis in order to study heat transport in LHD and TJ-II. TOTAL code was created by Dr. Kozo Yamazaki and Dr. Tsuneo Amano, and it is currently used mainly to simulate LHD plasmas. PRETOR-Stellarator transport code is a

modification from the originally PRETOR transport code created for tokamaks devices. It was created in the "Departament de Física i Enginyeria Nuclear" (DFEN) at the "Universitat Politècnica de Catalunya" (UPC). It is used to simulate TJ-II plasmas, and the results have been compared with the transport code PROCTR, used in the CIEMAT, leading to the conclusion that their results were quite similar [Fon99]. A description of both codes will be reported in the following sections.

3.2 TOTAL transport code description

The simulation code TOTAL [Yam92] was created at the National Institute for Fusion Science (NIFS) in Japan in order to improve HSTR code. This code consists of a 3-dimensional equilibrium code with ohmic and bootstrap currents and a 1-dimensional transport code with neoclassical and anomalous transport. Neutral, impurity transport, and neutral beam deposition are also included. The interface between experimental data and the main program was also included as well as an interface between the experimental data and the equilibrium routine (PRE-TOTAL). A flow chart of the global TOTAL code is shown in figure 3.1.

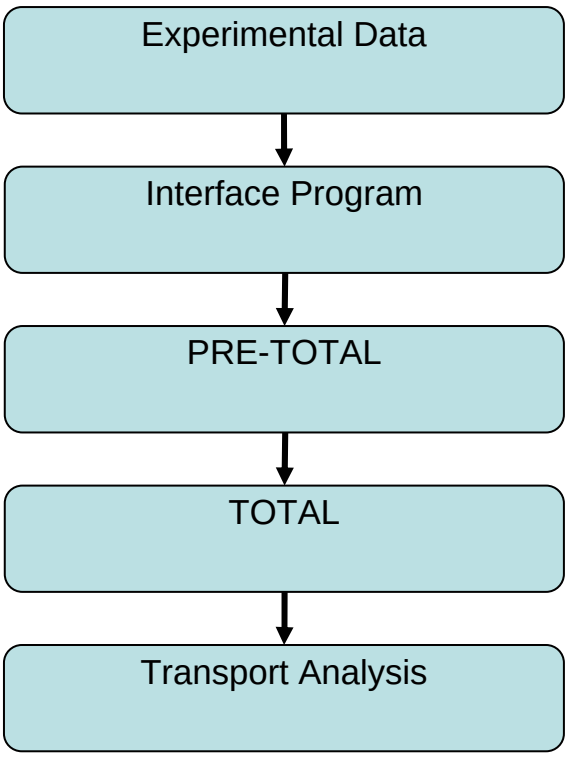

Figure 3.1 Flow Chart of global TOTAL code.

In figure 3.2 a flow chart of the internal TOTAL code is shown. As can be seen, TOTAL code is able to simulate the plasma equilibrium of stellarators as well as for tokamaks. In the stellarator case, the 3D equilibrium is solved by means of the VMEC code, and in the tokamak case, it is used APOLLO code. Once that the equilibrium is calculated, the VMEC coordinates are transformed into Boozer coordinates.

The code has other important tools, as the Electron Cyclotron Heating (ECH) Ray Tracing, the neoclassical transport (which includes calculation of ambipolar electric field with multiple-helicity magnetic field effects), Neutral Beam Injector (NBI) deposition (HFREYA), and neutral transport (AURORA). Finally, the 1D transport code HTRANS calculates transport in each iteration.

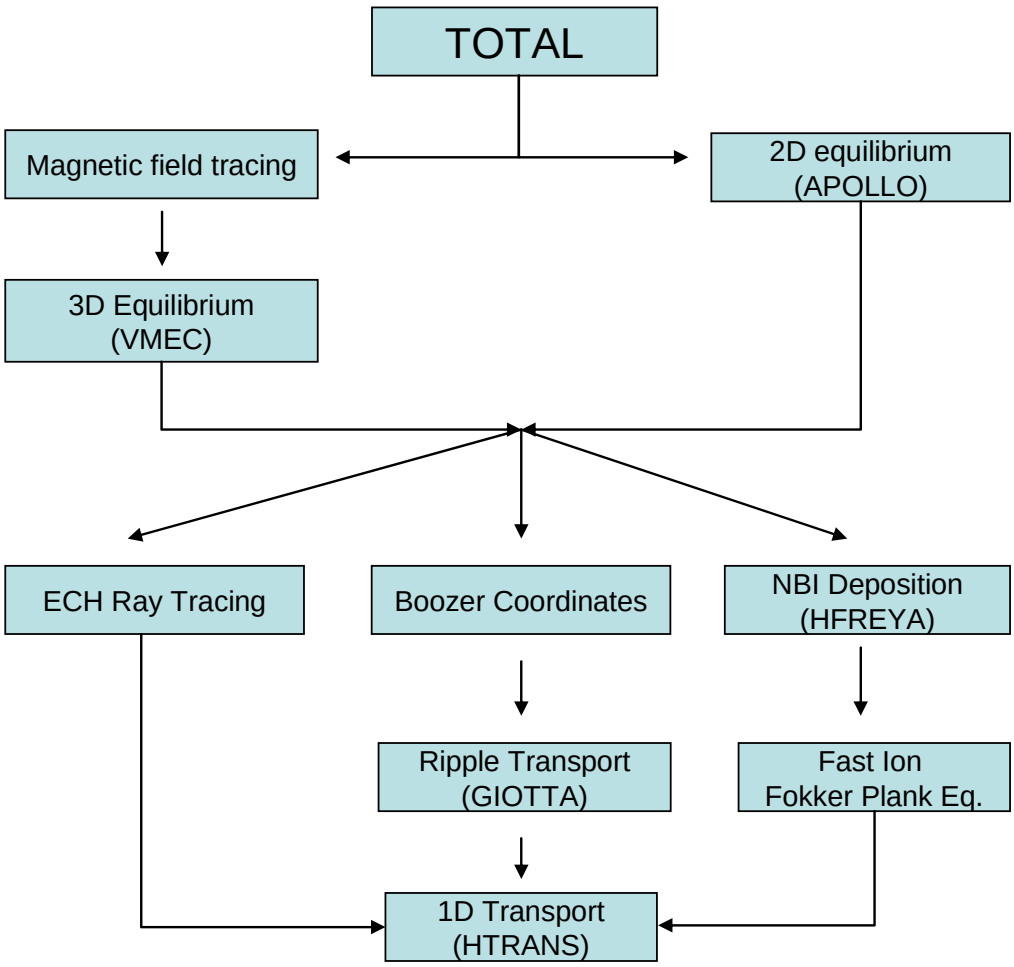

Figure 3.2 Flow Chart of internal TOTAL code.

3.3 Basic equations and models of the TOTAL code

3.3.1 Basic equations

TOTAL code solves the continuity equations for density and energy taking into account the source terms. These equations are similar to the ones used in other transport codes, particularly the ASTRA code [Per91],

$$\frac{\partial n_k}{\partial t} = -\frac{1}{V'}\frac{\partial}{\partial \rho}\left[V'\left(\Gamma_k^{neoc} + \Gamma_k^{ano}\right)\right] + S_k \tag{3.1}$$

$$\frac{3}{2}\frac{\partial (n_e T_e)}{\partial t} = -\frac{1}{V'}\frac{\partial}{\partial \rho}\left[V'\left(Q_e^{neoc} + \frac{5}{2}\Gamma_e^{neoc} T_e - n_e \chi_e^{ano}\left\langle |\nabla \rho|^2 \right\rangle \frac{\partial T_e}{\partial \rho} + \frac{3}{2} T_e \Gamma_e^{ano}\right)\right] + P_e \tag{3.2}$$

$$\frac{3}{2}\frac{\partial (n_k T_k)}{\partial t} = -\frac{1}{V'}\frac{\partial}{\partial \rho}\left[V'\left(Q_k^{neoc} + \frac{5}{2}\Gamma_k^{neoc} T_k - n_k \chi_k^{ano}\left\langle |\nabla \rho|^2 \right\rangle \frac{\partial T_k}{\partial \rho} + \frac{3}{2} T_k \Gamma_k^{ano}\right)\right] + P_k \tag{3.3}$$

$$\Gamma_k^{ano} = -D_k^{ano}\left\langle |\nabla \rho|^2 \right\rangle \frac{\partial n_k}{\partial \rho} + V_{p,k}\left\langle |\nabla \rho| \right\rangle n_k \tag{3.4}$$

$$n_e = \sum_k z_k n_k \tag{3.5}$$

Equation 3.1 is the density equation for each specie k. Equation 3.2 and 3.3 are pressure equations for electrons and each ion specie k respectively. Equation 3.4 is the particle flux definition for each specie k. Finally equation 3.5 is the definition of the quasy-neutrality of the plasma.

The particle source for each specie k, S_k, consists of the sources from pellet injection, gas-puffing neutrals, NBI and recycling. P_e and P_k correspond to the heat sources and sinks. Their expression is the following,

$$P_e = P_{\alpha,e} + P_{rf,e} + P_{nb,e} - P_{ei} - P_{ion} - P_{brems} - P_{EC} - P_l \tag{3.6}$$

$$P_i = P_{\alpha,i} + P_{rf,i} + P_{nb,i} - P_{ei} - P_{cx} \tag{3.7}$$

where $P_{\alpha,e}$, $P_{\alpha,i}$ are the alpha particle heating, $P_{rf,e}$, $P_{rf,i}$ are RF heating, $P_{nb,e}$, $P_{nb,i}$ are neutral bean heating, P_{ei} is equi-partition energy, P_{ion}, P_{cx} are ionization and charge Exchange losses, P_{brems}, P_{EC}, P_l are Bremmstrahlung, synchrotron and line radiation terms respectively.

3.3.2 Physic models implemented

3.3.2.1 Neutral particle recycling and gas-puffing

The code AURORA [Hug78] is used to compute the neutral particle density distribution and ionization and charge exchange processes. The input into AURORA is recycling flux $\Gamma_{recycle}$ and gas puffing flux $\Gamma_{gaspuff}$, recycling rates from the wall, gas puffing and recycling particle energy.

3.3.2.2 Pellet injection

Pellet injection is modeled by using two models,

1. Parks and Turnbull NGS model [Par78]
2. Kuteev model [Kut95]

In the NGS (neutral gas shielding) model, the ablation rate dN/dt (in atoms/s) is given by

$$\frac{dN}{dt} = 5.2\times10^{16} n_e^{1/3} T_e^{1.64} r_p^{1.333} M_i^{-0.333} / V_p \tag{3.8}$$

where the electron temperature is measured in eV, r_p is the pellet radius M_i is the mass number of the pellet material in atomic units and V_p is the pellet velocity. The number of atoms in the pellet is expressed as,

$$N = 2n_s\left(\frac{4\pi r_p^3}{3}\right) \tag{3.9}$$

where n_s is the molecular density of the solid hydrogen.

In the Kutteev model dN/dt is given by,

$$\frac{dN}{dt} = 5.1\times10^{14} n_e^{0.453} T_e^{1.72} r_p^{1.443} M_i^{-0.283} / V_p \tag{3.10}$$

3.3.2.3 ECR heating

For electron cyclotron resonance (ECR) heating a simple form is used in most of the cases,

$$P_{ec} = P_0 \exp\left[\frac{-(\rho-\rho_{res})^2}{\rho_{wid}^2}\right] \tag{3.11}$$

where P_0 is normalized so as the total energy input is a given input power, ρ_{res} is the resonant position and ρ_{wid} is the resonance width.

3.3.2.4 Neutral beam heating

HFREYA code (i.e. the stellarator version of FREYA code [Lis76]) is used to simulate NBI deposition and FIFPC Fokker-Plack code [Fow78] to follow the thermalization.

3.3.2.5 Alpha particle heating

For alpha heating the routine followed is quite similar to that used in PRETOR [Bou92] code,

$$\langle\sigma v\rangle_{fusion} = 11730.2\,\Theta\sqrt{\frac{f}{1124656 T_{i3}^3}}\exp(-3f) \tag{3.12}$$

$$\Theta = \frac{T_i}{\left[1-T_i\left(\theta_1+T_i\left(\theta_2-T_i\theta_3\right)\right)\right]}\times\frac{1}{\left[1+T_i\left(\theta_4+T_i\left(\theta_5+T_i\theta_6\right)\right)\right]}$$

$$\theta_1 = 0.0151361 \quad \theta_3 = 0.00010675 \quad \theta_5 = 0.0135$$
$$\theta_2 = 0.00460643 \quad \theta_4 = 0.0751886 \quad \theta_6 = 0.00001366$$

$$f = \left(\frac{1182.176936}{4\Theta}\right)^{1/3}$$

The proportion g_α of the fusion energy that goes to the heating of ions is,

$$g_\alpha = \frac{1.03}{\left[1+E_c\left(0.35+0.02W_c\right)\right]}$$

$$W_c = \frac{58.333}{T_e\left[\left(n_D + n_T\right)/\left(2n_e\right) + n_\alpha / n_e\right]^{2/3}}$$

Then, the alpha power density is,

$$P_\alpha = n_D n_T E_0 \left\langle \sigma v \right\rangle_{fusion} \left(1 - f_{ripple}\right) \tag{3.13}$$

$$P_{\alpha,e} = P_\alpha \left(1 - g_\alpha\right) \qquad P_{\alpha,i} = P_\alpha g_\alpha \tag{3.14}$$

where E_0=3.52 [MeV] and f_{ripple} is the ripple loss fraction.

3.3.2.6 Radiation losses

Bremmstrahlung radiation loss is given by,

$$P_{brems} = 1.6 \times 10^{-2} z_{eff} n_{e20}^2 T_{e10}^{1/2} \tag{3.15}$$

where $n_{e20} = n_e / 10^{20}$ and $T_{e10} = T_e / 10$.

Synchrotron radiation loss is given by

$$P_{EC} = 6.2 \times 10^{-2} n_{e20} T_{e10} B^2 \Phi_s \tag{3.16}$$

where $\Phi_s = 2.1 \times 10^{-3} T_{e10}^{3/2} \left[B_0 / \left(n_{e20} a\right)\left(1 + X_{syn}\right)\right]^{1/2} \left(1 - R_w\right)^{1/2}$, $X_{syn} = 5.7 / A T_{e10}^{1/2}$, R_w is the wall reflection. CYTRAN [Tam81] routine has been introduced recently in TOTAL code in order to improve synchrotron radiation calculation taking account non-local effects.

Line radiation losses from impurity ions can be calculated by using the IMPDYN code [Ama82]. IMPDYN solves the impurity transport equation for any number of multi-species impurities by using ADPAK [Hul83] atomic physics package.

3.3.2.7 Anomalous transport

Several anomalous transport models are currently available in the code (empirical and theoretical models).

- 6-Regime drift wave model (electrostatic and electromagnetic)
- LHD scaling

- W7-AS scaling
- Empirical Alcator
- Empirical ISS95

Some new transport models, as will be reported in chapter 7, have been recently added to study the Internal Transport Barrier formation and the effect of the electric field and its shear on the anomalous transport suppression.

3.3.2.8 Neoclassical transport

The neoclassical model used in TOTAL code [Yam92] determines axisymmetric and asymmetric particle and heat neoclassical diffusivities (diagonal and off-diagonal terms) as well as non-ambipolar electric field. Further description of this model will be reported in chapter 5.

3.3.3 Boundary Conditions

The boundary conditions on the diffusion equations 3.1, 3.2 and 3.3 are,

$$\frac{\partial n_k}{\partial \rho} = \frac{\partial \left(n_e T_e \right)}{\partial \rho} = E_\rho = 0 \text{ at } \rho = 0$$

At the plasma boundary ($\rho = a$), the value or the radial gradient of each variable is specified.

3.3.4 Initial conditions

When no initial input data is specified, the particle density, temperatures and effective charge distributions are taken as,

$$n_e = anec + \left(anec - aneli \right) \left[1 - \left(\rho / a \right)^{anel} \right]^{anem} \tag{3.17}$$

$$T_e = atec + \left(atec - ateli \right) \left[1 - \left(\rho / a \right)^{atel} \right]^{atem} \tag{3.18}$$

$$T_i = atic + \left(atic - atili \right) \left[1 - \left(\rho / a \right)^{atil} \right]^{atim} \tag{3.19}$$

$$Z_{eff} = zefc + \left(zefc - zefli \right) \left[1 - \left(\rho / a \right)^{zefl} \right]^{zefm} \tag{3.20}$$

where the constants must be adjusted to have the desired input profile for each variable.

3.4 TOTAL code modifications

Some modifications of TOTAL code have been carried out recently in order to have a graphics interface screen between the main program and the final user. This new version is called TOTAL_P [Ama00]. In this code, the former TOTAL code and the Graphic User Interface (GUI) from PRETOR [Bou92] code are combined. These modifications allow the interaction between the user and the main code by changing many important parameters of the simulation, as the anomalous transport parameters, power depositions or fire pellet velocities for example. Besides, some plasma variable profiles can be seen in the screen, as shown in figure 3.3. It is also possible to see the time evolution of some important variables, as shown in figure 3.4. Other feature of this code is that the output data can be easily analyzed in real time in a summary screen, as shown in figure 3.5.

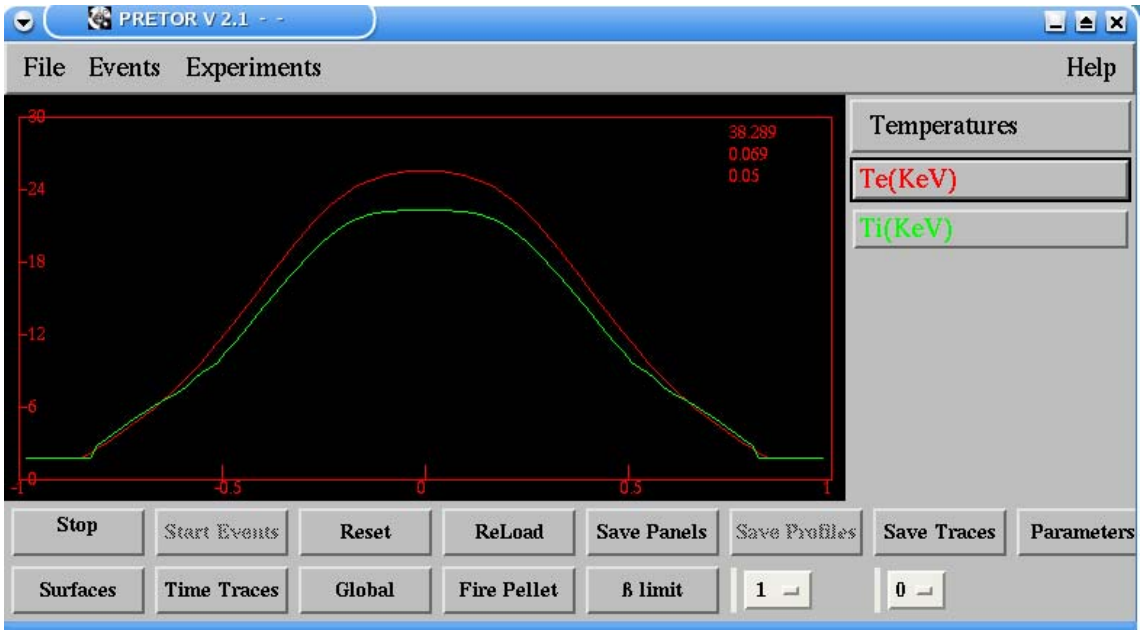

Figure 3.3 Electron and ion temperature profiles as appear in the TOTAL_P code interactive screen.

Finally, and related to some technical characteristics, the main TOTAL code is programmed in FORTRAN language and can be compiled using any compiler. The advantage is that can be run in any operative system. However, TOTAL_P code must be

run in UNIX workstations or in personal computers with LINUX by using MOTIF libraries.

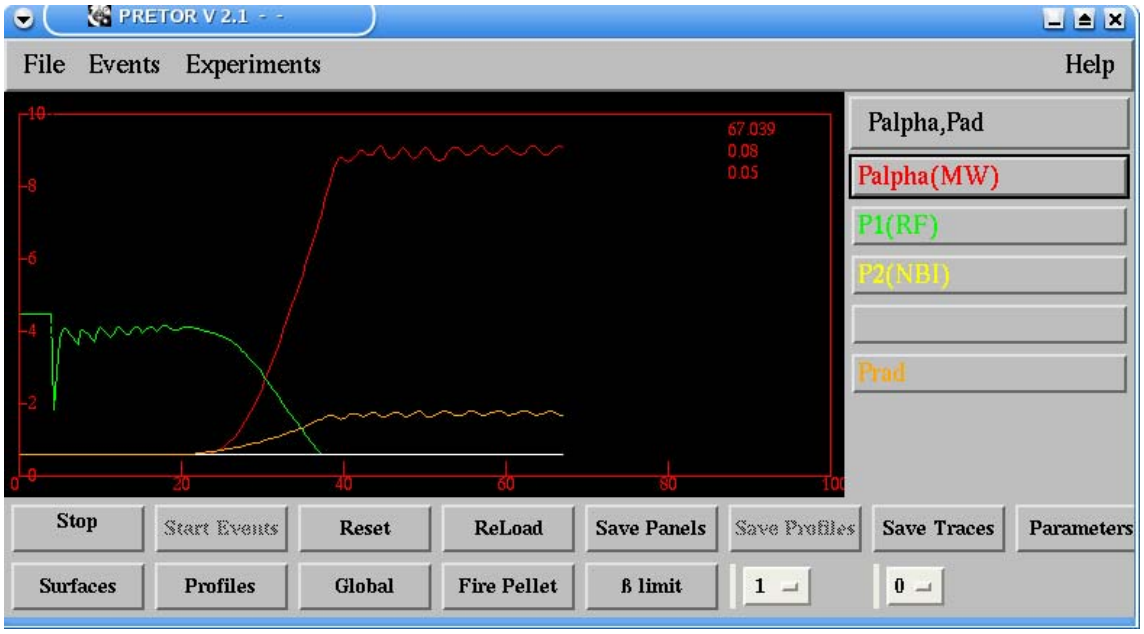

Figure 3.4 Alpha power, radiated power and RF heating time evolution as appear in the TOTAL_P code interactive screen.

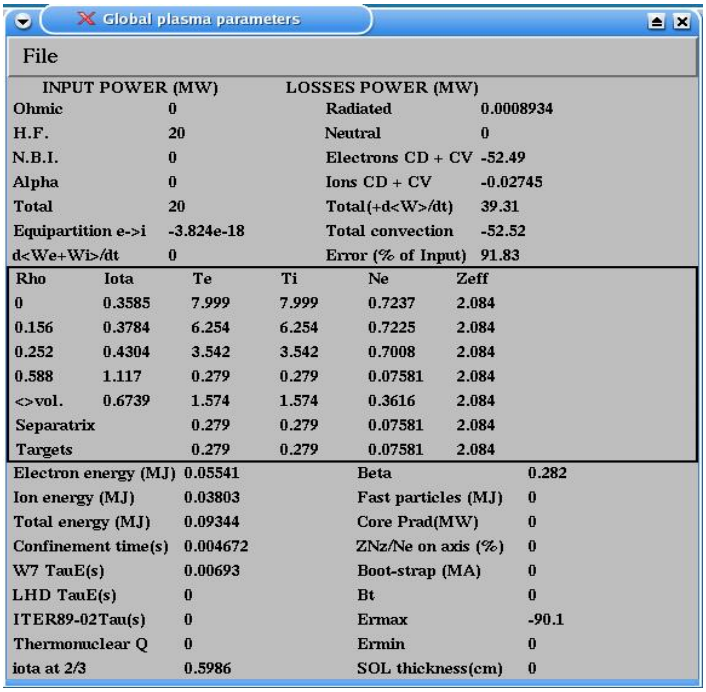

INPUT POWER (MW)		LOSSES POWER (MW)	
Ohmic	0	Radiated	0.0008934
H.F.	20	Neutral	0
N.B.I.	0	Electrons CD + CV	-52.49
Alpha	0	Ions CD + CV	-0.02745
Total	20	Total(+d<W>/dt)	39.31
Equipartition e->i	-3.824e-18	Total convection	-52.52
d<We+Wi>/dt	0	Error (% of Input)	91.83

Rho	Iota	Te	Ti	Ne	Zeff
0	0.3585	7.999	7.999	0.7237	2.084
0.156	0.3784	6.254	6.254	0.7225	2.084
0.252	0.4304	3.542	3.542	0.7008	2.084
0.588	1.117	0.279	0.279	0.07581	2.084
<>vol.	0.6739	1.574	1.574	0.3616	2.084
Separatrix		0.279	0.279	0.07581	2.084
Targets		0.279	0.279	0.07581	2.084

Electron energy (MJ)	0.05541	Beta	0.282
Ion energy (MJ)	0.03803	Fast particles (MJ)	0
Total energy (MJ)	0.09344	Core Prad(MW)	0
Confinement time(s)	0.004672	ZNz/Ne on axis (%)	0
W7 TauE(s)	0.00693	Boot-strap (MA)	0
LHD TauE(s)	0	Bt	0
ITER89-02Tau(s)	0	Ermax	-90.1
Thermonuclear Q	0	Ermin	0
iota at 2/3	0.5986	SOL thickness(cm)	0

Figure 3.5 Summary screen obtained in a simulation with TOTAL_P code.

3.5 PRETOR-Stellarator transport code description

3.5.1 Introduction

PRETOR [Bou92] is a transport simulation code originally designed for tokamak devices. It simulates time and radial variation of the main plasma physical variables by solving transport equations, which are quite similar to equations 3.1-3.5 previously described for TOTAL transport code. In order to solve these equations, PRETOR included only one anomalous transport model, Rebut-Llalia-Watkins, originally design for the JET.

PRETOR also included some other routines to simulate tokamak discharges properly, as NBI heating routines, ECR and ICR heating, fuelling by gas-puffing, radiation losses (Bremmstrahlung, synchrotron, line), neoclassical transport (tokamak-like version), alpha power and particle transport for example.

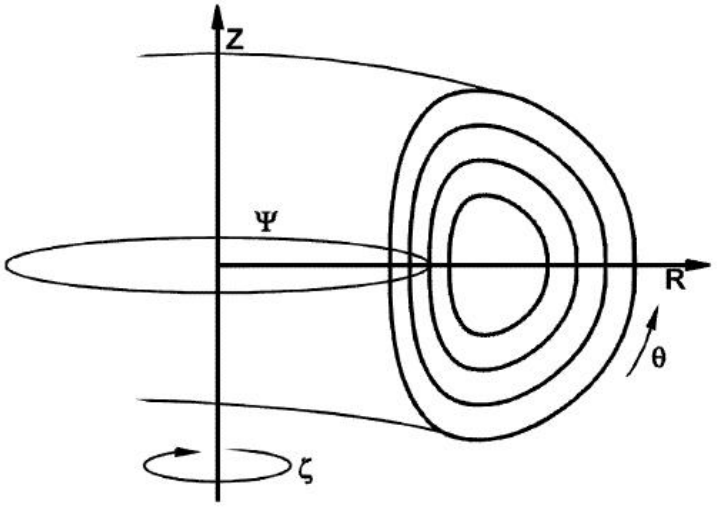

Figure 3.6 Cylindrical coordinates used in plasma description.

Related to magnetic topology, the plasma equilibrium is obtained by solving the Grad-Shafranov equation in cylindrical coordinates (R,Z,ξ) (figure 3.6) ,

$$R\frac{\partial}{\partial R}\left(\frac{1}{R}\frac{\partial \Psi}{\partial R}\right)+\frac{\partial^2 \Psi}{\partial Z^2}=-\mu_0\left(2\pi R\right)^2\frac{\partial P}{\partial \Psi}-4\pi R^2 B_t\frac{\partial B_t}{\partial \Psi} \qquad (3.21)$$

where Ψ is the magnetic poloidal flux, $P(\Psi)$ and $B_t(\Psi)$ are plasma pressure and toroidal magnetic field component respectively. The axisymmetric approximation for tokamaks $\frac{\partial}{\partial \xi} = 0$ has been used.

3.5.2 PRETOR code modifications

The original PRETOR code was modified in the "Departament de Física i Enginyeria Nuclear" with the aim of performing Stellarator simulations and analyze TJ-II data. This new code is PRETOR-Stellarator [Fon01]. The GUI used in PRETOR-Stellarator is very similar to the one used in the former PRETOR code (and in the TOTAL_P code), however some small changes were added, e.g. some screens with specific stellarator variables. The internal physics modification was performed taking account some important differences between tokamaks and stellarators,

- **Magnetic configuration**: Unlike in the tokamak case, the magnetic configuration is completely determined by the external coils.
- **Particle and energy transport**: Although tokamaks and stellarators share some important physical features, there are some important differences, e.g. Internal Transport Barrier formation, neoclassical transport or anomalous transport models.
- **Geometry**: The axisimmetryc lack makes difficult to treat some important variables, as neoclassical transport.
- **Scale laws**: Confinement time scale laws are completely different in tokamaks and stellarators.

All these features must be taken account in order to change from a tokamak transport code to a Stellarator one. A description of the changes made to PRETOR to obtain the stellarator version PRETOR-Stellarator is given in next sections.

3.5.3 Magnetic configuration and equilibrium

As it was pointed in the previous section, the magnetic equilibrium is calculated in the former PRETOR code by solving Grad-Shafranov equation. One important feature of this method is that the equilibrium is obtained in a very fast way. However, in a stellarator device, due to the complex geometry of the coils it is difficult to calculate the equilibrium and it is necessary to use more complex routines to overcome this issue. Therefore the magnetic equilibrium calculation was changed and the Variational Moments Equilibrium

Code (VMEC) routine, which is used to calculate magnetic equilibrium in the CIEMAT, was selected as the new calculation method.

A point on a magnetic surface can be described by cylindrical coordinates (R,Z,φ) where R is the major radius, Z is the height from the central plane and φ is the toroidal angle. That point can be also described by flux coordinates (ρ,θ,ζ) where ρ is the toroidal flux (or minor radius), θ is the poloidal angle and ζ is the toroidal angle (figure 3.7). The change of coordinate matrix is given in equation 3.22.

$$\begin{aligned} R(\rho,\theta,\zeta) &= \sum_{m,n} R_{m,n}(\rho)\cos\left(m\theta - n\zeta\right) \\ Z(\rho,\theta,\zeta) &= \sum_{m,n} Z_{m,n}(\rho)\cos\left(m\theta - n\zeta\right) \\ \phi(\rho,\theta,\zeta) &= \zeta \end{aligned} \tag{3.22}$$

Coefficients $R_{m,n}$ and $Z_{m,n}$ completely determine the magnetic surface. These coordinates are usually called VMEC coordinates. In the TJ-II case, a hundred coefficients are necessary to describe plasma surfaces due to their complex geometry. A schematic view of TJ-II plasma topology showing its bean shape is given in figure 3.8.

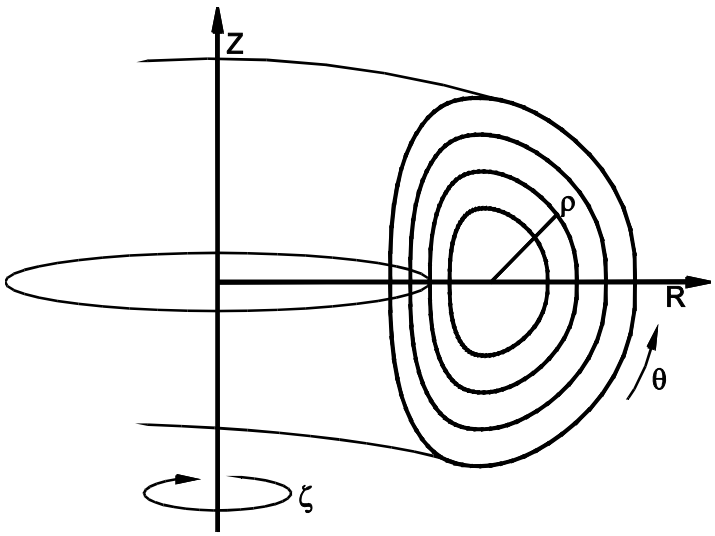

Figure 3.7 Flux coordinates schematic representation [Bou92].

The output data from VMEC are not just coefficients $R_{m,n}$ and $Z_{m,n}$ but other important variables, as rotational transform profile, toroidal flux, magnetic surfaces number,

incremental volume between surfaces or the toroidal and helicoidal ripple. Unlike in the former PRETOR code, where equilibrium was recalculated when the plasma beta or the current changed according to some condition, in PRETOR-Stellarator code all these parameters are read from the input file obtained from VMEC. Thus, magnetic equilibrium does not change during the simulation. This is a good approximation for ECRH plasmas with low beta, since magnetic conditions do not change very much.

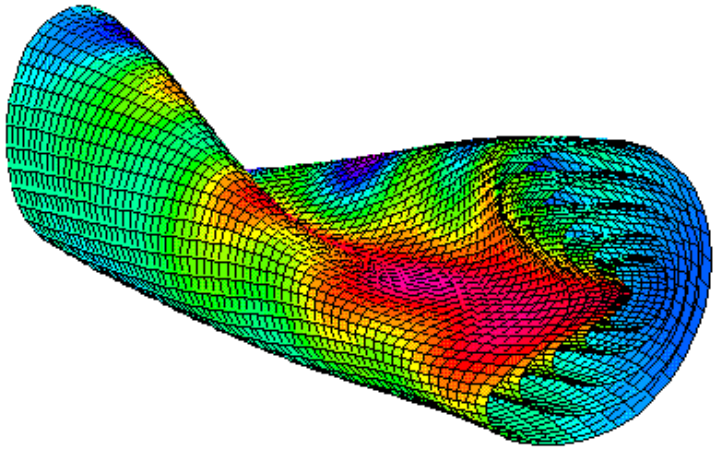

Figure 3.8 TJ-II plasma half period tridimiensional view with its characteristical bean shape [CIE05].

3.5.4 Geometry

As it was pointed previously, plasma geometry in a stellarator device is quite more complicated than in a tokamak device. Taking account the fact that the former PRETOR was a 1D code, it was absolutely necessary to change this plasma description to describe the 3D complex geometry of a stellarator. This purpose is achieved by introducing a factor, $\left\langle (\nabla\rho)^2 \right\rangle$, in the plasma heat transport, Q_e and in particle transport Γ_k , which takes account of this complex geometry,

$$Q_e = -1.6\times10^{-3} < (\nabla\rho)^2 > n_e \chi_e \frac{\partial T_e}{\partial\rho} + 1.6\times10^{-3} \frac{3}{2} T_e \Gamma_e \tag{3.23}$$

$$\Gamma_k = - < (\nabla\rho)^2 >_k \; D_k \; \frac{\partial n_k}{\partial\rho} + < |\nabla\rho| > \; n_k \; V_k \tag{3.24}$$

The factor $\left\langle (\nabla\rho)^2 \right\rangle$ can be regarded as a geometric average over the toroidal and poloidal directions. Its expression can be deduced from the metric tensor g_{ij}. This tensor is derived from the change coordinate matrix expression from flux coordinates to cylindrical coordinates, and it is defined as,

$$g_{ij} = \frac{\partial \vec{r}}{\partial \alpha_i} \cdot \frac{\partial \vec{r}}{\partial \alpha_j} \tag{3.25}$$

where each α_i = (ρ,θ,ζ) corresponds to the flux coordinates and $\vec{r}$ is the general position vector in cylindrical coordinates,

$$\vec{r} = \hat{e}_R + R\hat{e}_\phi + \hat{e}_Z \tag{3.26}$$

Therefore, evaluating explicitly the scalar product from equation 3.25 we get the final expression for the metric tensor g_{ij}

$$g_{ij} = \frac{\partial R}{\partial \alpha_i}\frac{\partial R}{\partial \alpha_j} + R^2 \frac{\partial \phi}{\partial \alpha_i}\frac{\partial \phi}{\partial \alpha_j} + \frac{\partial Z}{\partial \alpha_i}\frac{\partial Z}{\partial \alpha_j} \tag{3.27}$$

The factor $(\nabla\rho)^2$ is defined on a point over the plasma surface as [How90] as,

$$(\nabla\rho)^2 = \frac{1}{g}\left(g_{\theta\theta}g_{\zeta\zeta} - g_{\theta\zeta}^2\right) \tag{3.28}$$

with

$$\sqrt{g} = R \ \det\left(\frac{\partial x_i}{\partial \alpha_j}\right) = R\left(\frac{\partial R}{\partial \theta}\frac{\partial Z}{\partial \rho} - \frac{\partial R}{\partial \rho}\frac{\partial Z}{\partial \theta}\right) \tag{3.29}$$

where $x_i = (R,\phi,Z)$ are the cylindrical coordinates.

By introducing the general expressions of R(ρ,θ,ζ), Z(ρ,θ,ζ) y $\phi(\rho,\theta,\zeta)$ from equation 3.22, the expression for $(\nabla\rho)^2$ is obtained as follows,

$$(\nabla\rho)^2 = \frac{\left[\left(R_\theta^2 + Z_\theta^2\right)\left(R_\zeta^2 + R^2 + Z_\zeta^2\right) - \left(R_\theta R_\zeta + Z_\theta Z_\zeta\right)^2\right]}{R^2\left(R_\theta Z_\rho - R_\rho Z_\theta\right)^2} \tag{3.30}$$

where,

$$
\begin{aligned}
R_\theta &\equiv \frac{\partial R}{\partial \theta} = \sum_{m,n} - m\, R_{m,n}\, sin(m\theta - n\zeta) \\
R_\zeta &\equiv \frac{\partial R}{\partial \zeta} = \sum_{m,n} n\, R_{m,n}\, sin(m\theta - n\zeta) \\
R_\rho &\equiv \frac{\partial R}{\partial \rho} = \sum_{m,n} \left.\frac{\partial R_{m,n}}{\partial \rho}\right|_{\substack{\theta=ct \\ \zeta=ct}} \cos(m\theta - n\zeta) \\
Z_\theta &\equiv \frac{\partial Z}{\partial \theta} = \sum_{m,n} m\, Z_{m,n}\, \cos(m\theta - n\zeta) \\
Z_\zeta &\equiv \frac{\partial Z}{\partial \zeta} = \sum_{m,n} - n\, Z_{m,n}\, \cos(m\theta - n\zeta) \\
Z_\rho &\equiv \frac{\partial Z}{\partial \rho} = \sum_{m,n} \left.\frac{\partial Z_{m,n}}{\partial \rho}\right|_{\substack{\theta=ct \\ \zeta=ct}} sin(m\theta - n\zeta) \\
R &= \sum_{m,n} R_{m,n}\, \cos(m\theta - n\zeta)
\end{aligned}
\tag{3.31}
$$

The term $\left\langle (\nabla\rho)^2 \right\rangle$, which appears in equations 3.23 and 3.24, is the average of $(\nabla\rho)^2$ over a global plasma magnetic surface,

$$
\left\langle (\nabla\rho)^2 \right\rangle = \frac{\int_\psi (\nabla\rho)^2 \sqrt{g}\; d\theta\; d\zeta}{\int_\psi \sqrt{g}\; d\theta\; d\zeta} \tag{3.32}
$$

where $\sqrt{g}$ is the change coordinates matrix determinant defined in equation 3.29. The integral $\int_\psi \sqrt{g}\, d\theta\, d\zeta$ is the plasma volume contained by two plasma surfaces between minor radius ρ and $\rho + d\rho$.

3.5.5 Energy and particle transport

The former transport model implemented in PRETOR, Rebut-Llalia-Watkins, was not convenient to simulate transport in stellarators, therefore it was decided to change it by other pseudo-empirical models obtained from stellarator studies. The models implemented for the electron heat diffusivity were the following,

- Alcator with fixed shape
- Alcator with soft beta limit

- Pseudoclassic
- LHD empirical
- Empirical with density dependence

For the ion heat diffusivity,

- Alcator with fixed shape
- Hinton-Hazeltine
- Hinton-Hazeltine with Chang-Hinton correction
- Empirical with no density dependence

For the ion particle diffusivity,

- Neoclassical
- Fixed shape
- Alcator with fixed shape
- Alcator
- Pseudoclassic
- Proportional to electron heat diffusivity

A description of each transport model can be found in [Fon01]

3.5.6 Confinement time

The energy confinement time, defined as the energy remaining time in the plasma, is calculated by means of the expression $\tau_E = W / P_{ext}$, where W is the plasma energy and P_{ext} the injected power. Wide ranges of expressions for the confinement time have been obtained from the experimental data analysis done in many stellarator devices. Three expressions among them were introduced in PRETOR-Stellarator,

LHD $$\tau_E = 0.17 R^{0.75} a^2 B^{0.84} n_{e,20}^{0.69} P_{ext}^{-0.58} M^{0.5} \quad (3.33)$$

Gyro-Reduced Bohm $$\tau_E = 0.25 R^{0.6} a^{2.2} B^{0.8} n_{e,20}^{0.6} P_{ext}^{-0.60} M^{0.5} \kappa \quad (3.34)$$

Lackner-Gottardi $$\tau_E = 0.172 R a^2 B^{0.8} n_{e,20}^{0.6} P_{ext}^{-0.60} M^{0.5} \iota^{0.4} \quad (3.35)$$

where τ_E is expressed in seconds, R is the plasma major radius (in m), a is the plasma minor radius (in m), B is the magnetic field (in T), $n_{e,20}$ in the electron density (in 10^{20} m^{-3}),

κ is the plasma elongation, ι is the rotational transform and *M* is the plasma effective mass number.

Taking account the fact that TJ-II device can work in a wide range of rotational transform values (including high ι) it seems particularly important for TJ-II plasmas simulation the Lackner-Gottardi scaling, due to the explicit dependence on the rotational transform ι.

3.6 Summary

The extraordinary complicated equations involved in plasma physics field makes simulation codes absolutely necessary to study these plasmas as well as to analyze experimental data. Besides, with these codes, future commercial reactors design will be an easier issue.

Two transport codes have been used along this thesis: TOTAL and PRETOR-Stellarator codes.

TOTAL code was created by Dr. Kozo Yamazaki at NIFS institution in order to simulate helias devices. It solves the main plasma equations, as pressure equation and density equation, by using finite differences technique. Many physical models are available in this code, e.g. Bremmstrahlung, synchrotron (CYTRAN [Tam81] routine has been introduced recently) and line radiation, alpha power, neoclassical transport, anomalous transport, gas puffing, pellet injection, NBI and ECR heating. Plasma equilibrium is calculated by means of VMEC code before the simulation. However, VMEC coordinates are transformed in Boozer coordinates in order to have a better NBI simulation.

A modification of the former TOTAL code has been created by adding graphics user interface. This new version is the TOTAL_P code and it allows a fast interaction between the user and the code by changing many plasma variables when simulation is running. Besides, input and output data can be easily modified and analyzed.

PRETOR-Stellarator is a modification of the former PRETOR code made at the "Departament de Física i Enginyeria Nuclear" in the "Universitat Politècnica de Catalunya". The modifications consist in introducing necessary changes to simulate stellarator plasmas. Some of these changes are related to plasma equilibrium (VMEC code

is used), plasma geometry (factor $\left\langle (\nabla\rho)^2 \right\rangle$ is calculated in every magnetic surface), anomalous transport models and confinement time scaling laws.

PRETOR-Stellarator transport code simulations have been checked with TJ-II experimental data [Die02] and compared with other transport simulation codes as PROCTR [Fon99]. Since these validations have been always successful, we can conclude that PRETOR-Stellarator is a good code to simulate stellarator shots.

Chapter 4

Remote participation

4.1 Introduction

The collaboration between different fusion laboratories is becoming essential in order to improve fusion research. The reason is that fusion devices are difficult to build and design, therefore it is completely necessary the collaboration between different scientific and technological research centers which are specialist in different fusion device components. Moreover, due to the expensive cost of the large fusion devices, the collaboration between different countries also seems essential (as has been demonstrated in the ITER case).

In the European Union these ideas have been integrated in the JET (Joint European Torus) by means of the EFDA-JET agreement. The laboratories belonging to EURATOM (European Atomic Energy Community) design the experiments which are performed in the JET site in Culham. The responsible of the maintenance of JET is the UKAEA (United Kingdom Atomic Energy Association), whereas the rest of associations share the scientific goals. The data analyses are performed by using remote tools to the central computers at JET. Moreover, in order to share some of these results, several meetings and colloquia which are planned to be hold at JET can be followed by internet. However, a more sophisticated plan is being developed at the present time. It consists in sharing all the scientific data between members of EURATOM by allowing the access to the computers. However, a major drawback of this network is the connection security.

Another laboratory where remote participation is extensively used is the “Max-Planck Institute für Plasmaphysik” in Germany. This laboratory has three sites, one in Greifswald, another one in Garching and finally in Berlin. In the Garching site are located

the tokamak ASDEX upgrade and the stellarator W7-AS. Moreover, W7-X stellarator is currently being built in Greifswald. In order to share the main scientific results of the different sites, several videoconferencing meetings are planned for each campaign. In addition, it is expected that only the technicians who takes care of W7-X go to Greifswald whereas the main scientific staff can control the device from Garching (see figure 4.1).

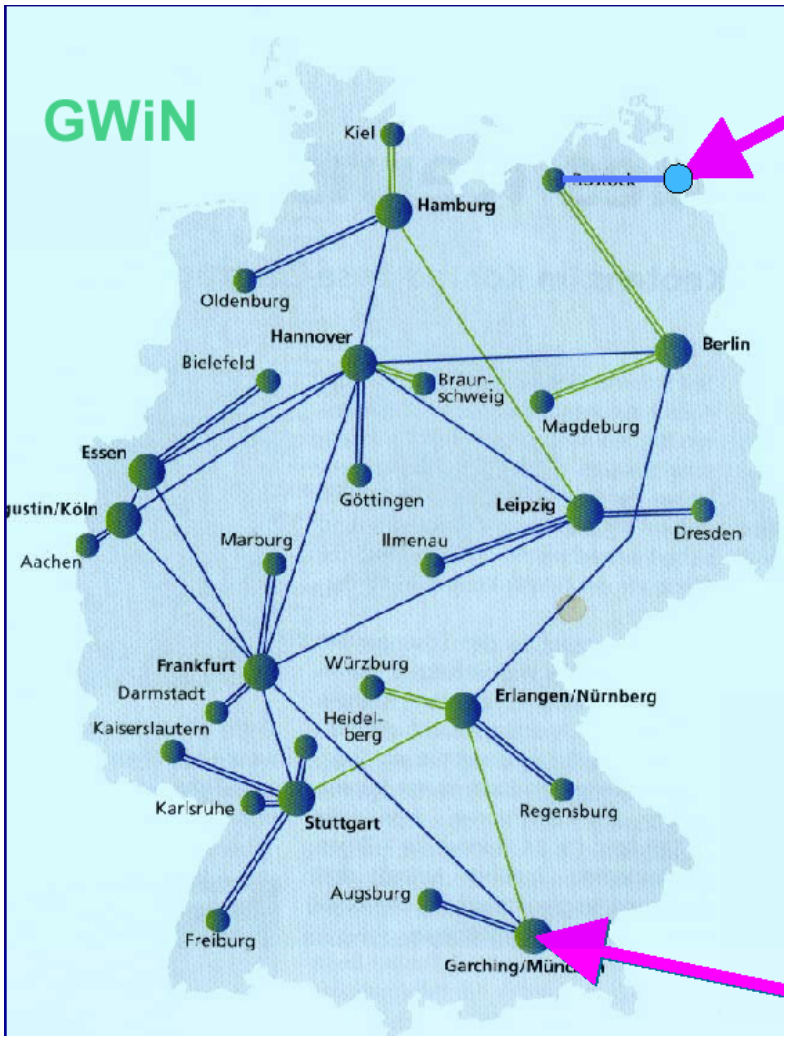

Figure 4.1 Internet high capacity connections network GWIN in Germany used for the remote participation system [Usc01].

Remote participation has been also developed in Spain. In the framework of the project “FTN2000-1743-C02-02” with title “Contribución al estudio remoto del transporte en TJ-II. Operación remota del espectrómetro de intercambio de carga” a collaboration between the “Laboratorio Nacional de Fusion Nuclear” and the “Departament de Física i Enginyeria nuclear” was established. As a result of this collaboration, a diagnostic (the

charge exchange spectrometer) has been controlled from Barcelona while the main operation of TJ-II was performed in Madrid. In addition, the TJ-II shot database can be accessed from Barcelona, therefore, transport studies and analysis can be performed is a faster way. Finally, periodic meetings via videoconference have been used to discus some of the results obtained. This former project has been extended in the framework of this thesis to the new one, ENE2004-05647-FTN, with title “TJ-II and LHD transport studies with semiempirical and theoretical models using remote participation techniques”.

All these techniques can be applied to other futures fusion devices, as ITER. The complexity of the ITER project, which needs several countries to be build, is a perfect example of the necessity of remote participation. The scientific staff from the different countries will be able to design their experiments in their own countries and to follow the results using remote participation. It will be also possible to organize meetings to share the main results with other scientific staff.

4.2 Remote participation tools

Remote participation techniques are formed by two different tools depending on the main goal of the remote interaction,

- Interaction between users
  - Videoconference systems
  - Instant messaging
  - Shared displays

In this case, the main goal of remote participation is to share information by means of meetings, colloquia, seminars or participation in the control room atmosphere. A lot of software has been developed with the aim of making possible this desire. Some of them are the following:

- **Virtual Room Videoconferencing System:** This system has been developed by Caltech (California Institute of Technology). It uses MBONE protocol, which allows two communications channels, one for images and another one for sound. In the latest versions H323 protocol is also available. This software can be used in two ways: point-to-point videoconference and multi-users videoconference. In this last case a virtual room must be reserved previously to the meeting. This program is becoming a standard in fusion community.

- **Microsoft Netmeeting:** This software uses H323 protocol and allows point-to-point videoconference, as well as, chat and desktop sharing. A drawback of this system is that it is necessary to know the I.P. direction of the other participant, and this fact, may lead to security problems.

- **iVisit:** It is a freeware software licensed by Eyematic Interfaces Inc. It uses MBONE protocol, like in the VRVS case, however this software is also available for Macintosh.

- **Microsoft Messenger:** This software is useful to have a permanent contact with the rest of the scientific community. It also allows point-to-point videoconference and file interchange between the users.

- **Yahoo messenger:** It is a program similar to the previous one but developed by Yahoo.

In addition to this type of remote participation there is another one which is more related to the direct development of the experiments,

- Interaction with experimental systems
  - Diagnostics
  - Whole experimental environment

No standard software has been developed to carry out this remote participation systems. Therefore, each laboratory has developed its own software.

4.3 TJ-II remote participation system

The TJ-II remote participation system can be summarized as follows [Veg03] (see figure 4.2),

- **Based on web technologies**
  - A web server is the most standard platform as communication front-end
  - A very scalable and flexible system architecture can be developed
  - All external accesses depend on a single protocol and a well-known communication port

- **User/system interplay based on JAVA technologies**
  - Network services are provided by means of resources supplied by JSP pages

- Client tools are web browsers and JAVA applications
- Deployment of JAVA software: there are ready-to-use solutions based on JNLP technology
  - Java Web Start

- **Distributed authentication and authorization system**
  - PAPI system

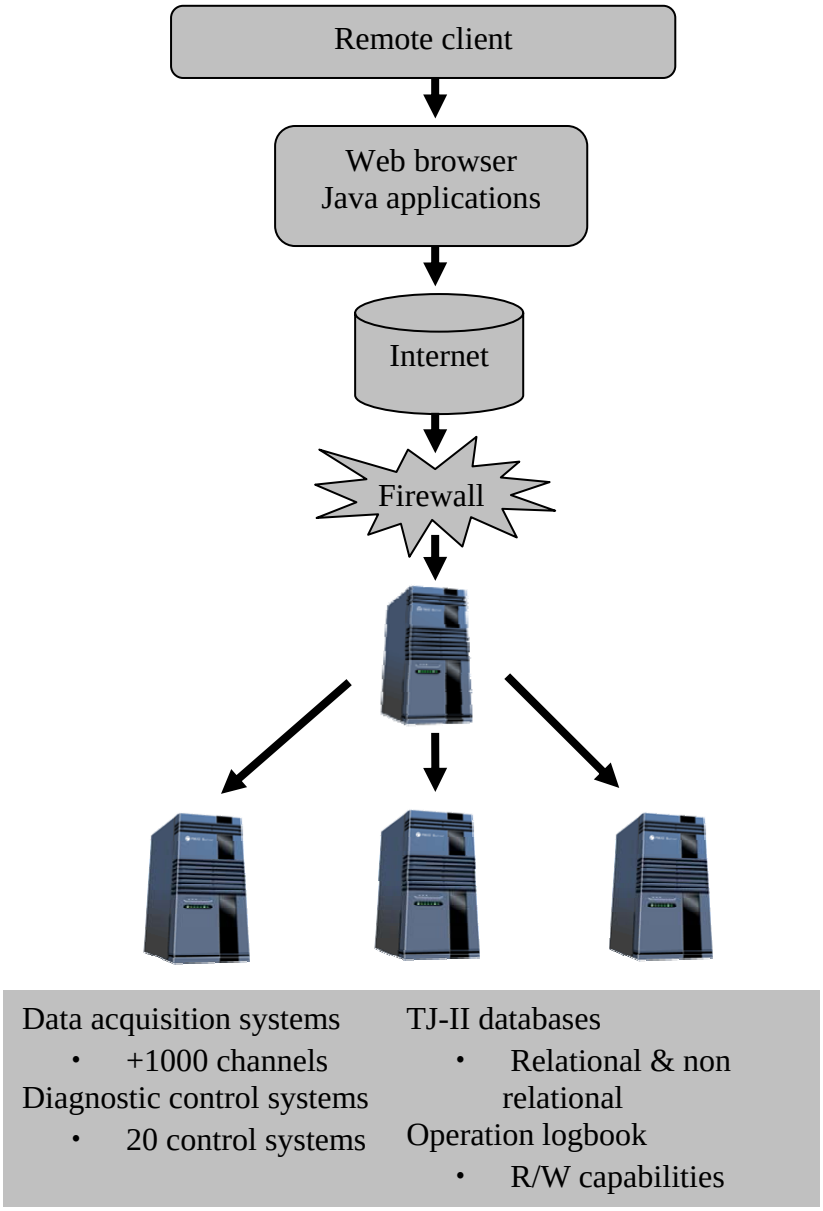

Figure 4.2 Flow chart of the remote participation program in TJ-II [Veg03].

The main characteristics of this system are the following:

- Same general tools for local and remote participants
- Unified system interface
- Distributed authentication and authorization system: PAPI
- Different user profiles
- Unique authentication per session
- Easy system administration
  - Firewall rules
  - Software distribution and version control
- Real multiplatform environment
- On-line access to software
- Scalability
  - Channels, systems and technologies
- Cost

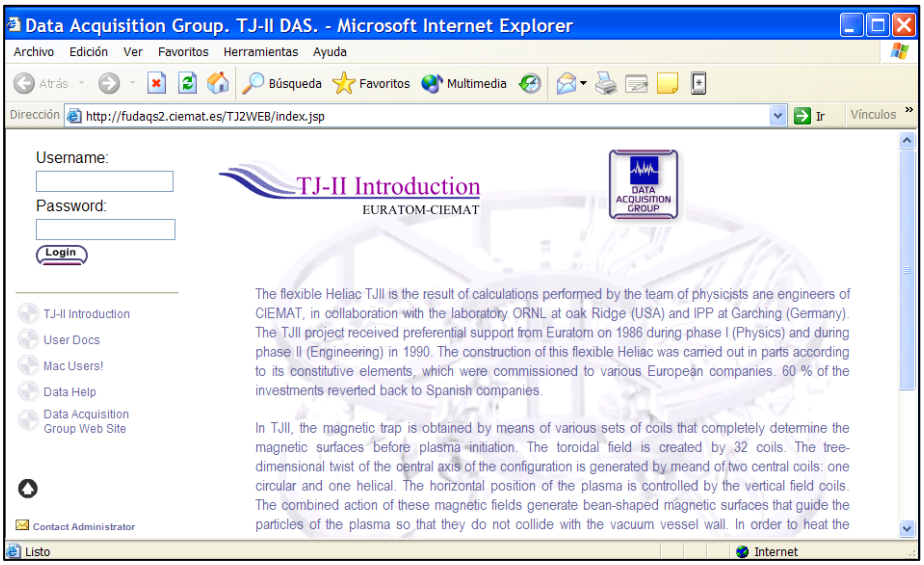

Figure 4.3 Access screen to the TJ-II remote participation system [Veg03].

The access screen to the TJ-II remote participation system is shown in figure 4.3. As can be seen just a web browser with internet connection is needed. In figure 4.4, the data visualization screen is showed. This screen is divided into two parts, in the right side several signal from different diagnostics can be selected in order to show the results in the graphic screen of the left side. The TJ-II remote participation system also allows the control of several diagnostics. In figure 4.5, the control screen of the wall diagnostic is shown. This remote control is fully operational, thus, it allows the full control of the

diagnostic, e.g. movements or open and close of valves. In this situation the TJ-II operation can be commanded from any laboratory with fast and safe internet connection. This fact is important since TJ-II experiment can be used by different laboratories leading to a great variety of experiments and results.

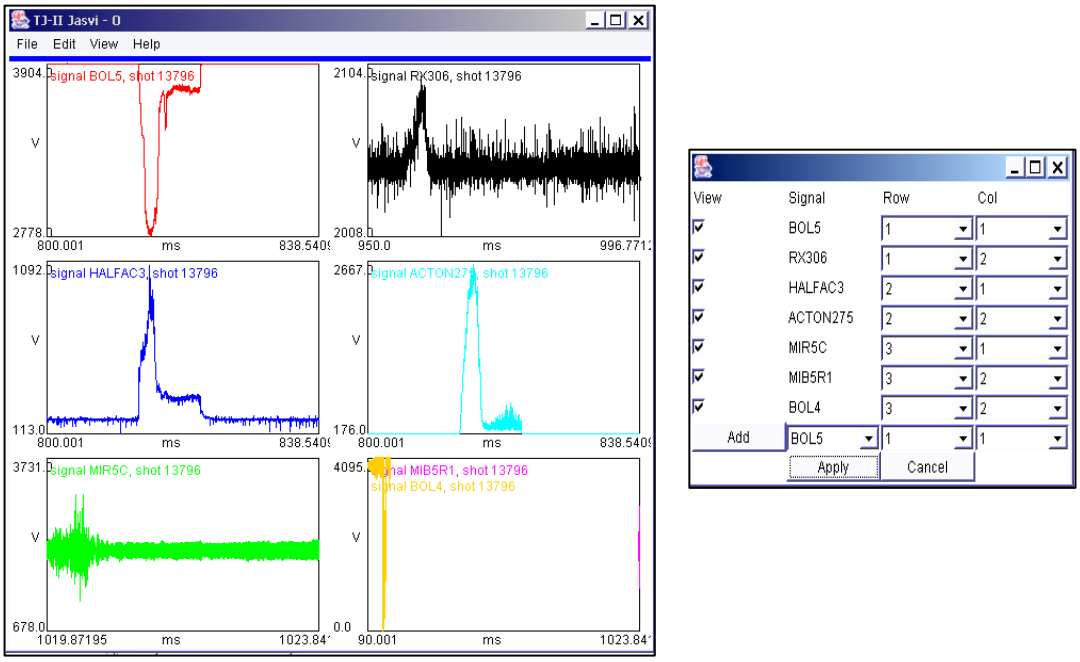

Figure 4.4 Data visualization screen of the main TJ-II diagnostics [Veg03].

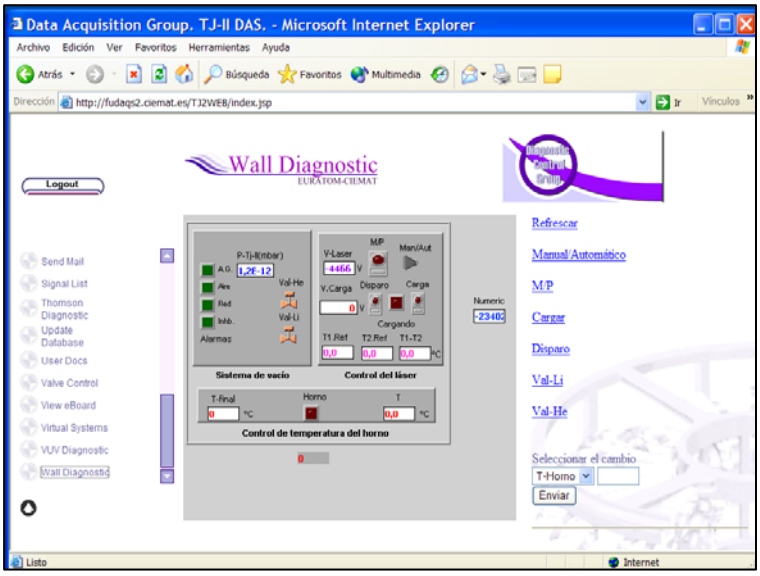

Figure 4.5 Remote control screen of the TJ-II wall diagnostic [Veg03].

4.4 Remote participation at the “Departament de Física i Enginyeria Nuclear”

The “Departament de Física i Enginyeria Nuclear¨ has been collaborating with CIEMAT for a long time. This collaboration has been focus in two main subjects, transport analysis of several TJ-II shots and the remote handling of the charge exchange spectrometer (CX diagnostic). In the first case, some selected computers in Barcelona were allowed to access to the main TJ-II shots databases with the aim of performing transport studies by means of PRETOR-Stellarator transport code. This feature has been very useful for this thesis, since the TJ-II shots analyzed have been selected, using remote participation tools, from a density scan experiment performed at TJ-II. In the second case, the CX diagnostic has been commanded (including movements and valves handling) from Barcelona with no major problems. However, in some situations internet had a very heavy traffic and the connection was a bit slow. In order to overcome this difficulty, a direct connection from the laboratory in Barcelona to the main internet provider (RedIris) was established.

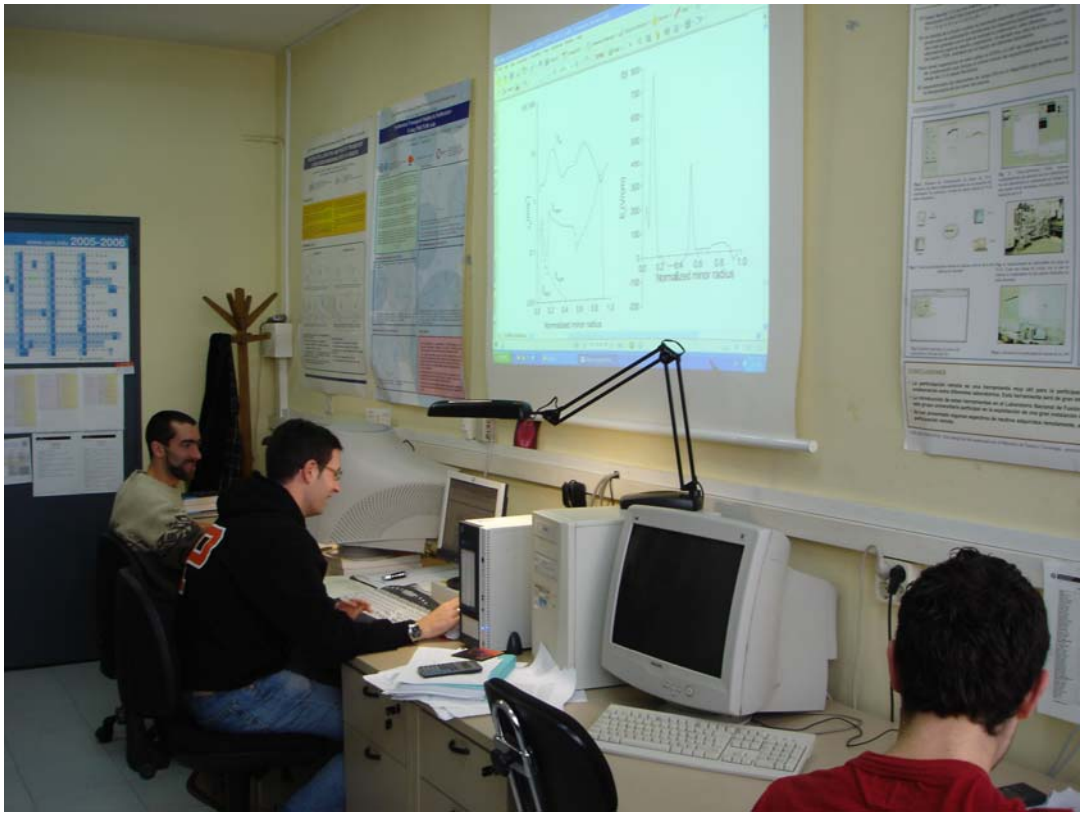

Figure 4.6 Remote participation laboratory at the “Departament de Física i Enginyeria Nuclear¨.

In addition to the remote participation operation previously pointed, some videoconferencing meetings have been carried out between the TJ-II staff and the “Departament de Física i Enginyeria Nuclear¨ to follow the operation. In order to perform these meetings, a webcam together with a microphone and a big screen were used (see figure 4.6).

In the framework of this thesis, remote participation has been extended to the National Institute for Fusion Science (NIFS) in Japan with the aim of following the development of the LHD transport studies performed in this thesis. The quality of the image and sound of the videoconferencing system was as good as the one obtained by the interaction with TJ-II laboratory.

4.5 Summary

Remote participation techniques are powerful tools that allow the interaction between different laboratories with the aim of sharing information in a fast way, performing experiments or fully command the control of a fusion device. In this framework, there is no need of staff displacement between long distance points yielding to an economic save. Moreover, the possibility that several laboratories can follow the experimental campaign of a fusion device can enhance the results of the physics studies performed with the data. These features will be particularly important in ITER, in which many different countries have collaborated.

The “Departament de Física i Enginyeria Nuclear¨ has been collaborating with the TJ-II team for a long time, controlling the CX diagnostic and analyzing several shots obtained directly from the main databases. In this thesis, this collaboration is being continued by studying the electron heat transport channel using semi-empirical and theoretical models by means of this remote participation tools. In addition, a new collaboration has been established with NIFS in order to perform the same studies in the LHD case.

Chapter 5

Study of neoclassical transport in LHD and TJ-II

5.1 Introduction

Electron Internal Transport Barrier (eITB) scenarios have been observed in several stellarator devices, e.g. LHD [Ida03], CHS [Fuj99], W7-AS [Str01b] and TJ-II [Cas02] with electron cyclotron heated (ECH) plasmas. In this situation, peaked electron temperature profiles with high central temperature and an improvement of confinement are obtained. Besides, a large electric field with a high electric field shear is obtained in those shots. Thus, one of the main conclusions of the experimental data analysis done is that these scenarios are driven mainly by neoclassical electric field. A reduction of anomalous transport levels to neoclassical values has been also observed broadly in these scenarios. Therefore, neoclassical transport has become an important subject of study in the stellarator transport research field in the last years, and several studies have been carried out in order to understand what type of interaction there is between neoclassical transport and the anomalous one.

Monte Carlo techniques are mainly used to study the neoclassical transport. The codes MOCA [Lot88] and DCOM [Wak01] are broadly used to study the particles trajectories and to obtain the diffusive coefficients of particles and energy transport, as well as the ambipolar electric field. These codes are very expensive in time consuming and have to be run with very fast computers, therefore, in order to have accurate results, a lot of time has to be spent. Moreover, as a consequence of the heavy calculations, these techniques

must be used to analyze the experimental results, not to perform a global simulation of the plasma.

Taking account the fact that the DFEN developed a transport simulation code in order to study stellarator plasmas, but this code lacked of neoclassical simulation, it was decided to introduce this kind of transport. However, in spite of Monte Carlo techniques are very accurate, they would slow the code too much in order to have a global and fast simulation. Therefore, to make simulations in real time, another approximation to the problem had been chosen. This approximation is based in the usual algebraic formulation of the ambipolarity relationship that uses, in the deviation of the particle from the flux surface, first order drift kinetic equation. Although these approximations may do not be so accurate like the ones obtained by means of Monte Carlo techniques, they can be useful to see different interactions between the plasma transport mechanisms. Particularly, this can be useful in TJ-II Stellarator, since the magnetic topology of the configuration is a key ingredient to explain the transport and it happens to be very complicated in TJ-II, being necessary to take into account about 150 terms in the Fourier description of magnetic field and magnetic surfaces, and this leads to very heavy Monte Carlo calculations. In this situation, previous studies done with DKES code [Rij89] [Tri01], present a poor convergence, and the error bars obtained from the calculation are pretty wide, making doubtful any result. Monte Carlo code MOCA is able to overcome this difficulty and to estimate neoclassical transport in the plasma core, although the results at the edge are still doubtful.

In order to check if these approximations can be used, the results obtained with Pretor-Stellarator simulation code will be compared with experimental data and Monte Carlo techniques.

5.2 Neoclassical transport in stellarators

Although neoclassical transport is quite similar in tokamaks and stellarators there is a significant difference between particle orbits in both cases. In stellarators, there are two different ripples, one is known as helical ripple and is generated by the helical coils in every stellarator. Another one is the toroidal ripple, which is generated along the toroidal curvature and is also present in tokamak geometries. The helical ripples have shorter periodic lengths than the toroidal ones. Since particles trapped in helical ripples also suffer from toroidal ripples, their orbit is not closed after one frequency period in the helical ripple. This type of motion leads to large particle excursion and high perpendicular transport. By analyzing these phenomena, it is concluded that the collision diffusion due to the trapped particles in the helical ripples is proportional to $1/\nu$, where ν is the collision

frequency. To see clearly the strong importance of these ripples in neoclassical transport, the dependence of the neoclassical diffusion coefficient D with ν is given in figure 5.1. The diffusion coefficients D_{gs}, D_p and D_{ps} correspond to banana diffusion, plateau diffusion and Pfirsch-Schlüter diffusion respectively and are relevant in the tokamak case. The coefficients D_e and D_h are only significant in the stellarator case and represent the neoclassical dependency on helical ripple. It is worth to point out that these coefficients are dependent of the electric field and the magnetic configuration, therefore depending on the device configuration, transport may be improved. This kind of challenges does not appear in the tokamak case and make this kind of transport a special matter of study in the stellarator neoclassical transport theory.

The existence of nonaxisymmetric quantities like the ones previously described, are responsible of the appearance of nonaxisymmetric particles and heat fluxes. These fluxes, are not automatically ambipolar in the stellarator case, thus $\Gamma_e \neq \Gamma_i$ (where Γ_e and Γ_i are the electron and ion particles fluxes respectively), unless there is an electric field, E_r, that allows to satisfy this condition. This electric field must be introduced explicitly in the equations of density and energy transport. In the tokamak case limit, this term vanishes.

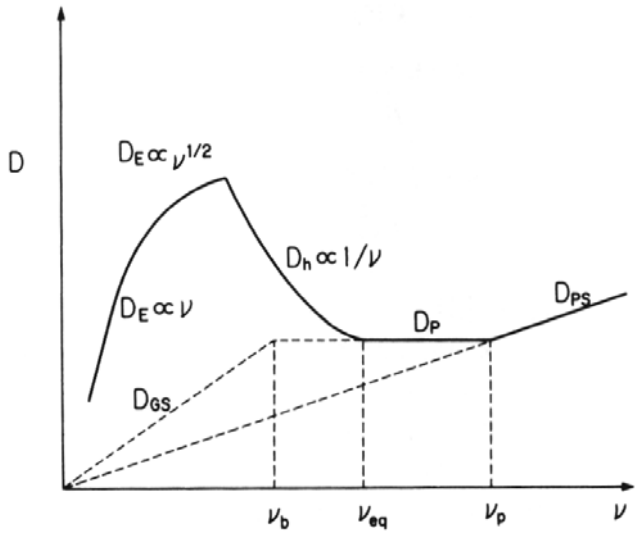

Figure 5.1 Diffusion coefficient dependence on collision frequency for heliotrons with $\varepsilon_h > \varepsilon_t$. Here $\nu_p = \nu_t/(qR)$, $\nu_b = \varepsilon_t^{3/2}\nu_p$ and $\nu_{eq} = \varepsilon_h^{3/2}\nu_p$ [Wak98].

5.2.1 Physics issues

Transport equations for electrons and ions can be deduced from Vlasov equation for the distribution equation f_k for each specie k [Wak98],

$$\frac{\partial f_k}{\partial t} + \vec{\mathrm{v}} \cdot \frac{\partial f_k}{\partial \vec{x}} + \frac{e_k}{m_k}(\vec{E} + \vec{\mathrm{v}} \times \vec{B}) \cdot \frac{\partial f_k}{\partial \vec{v}} = C_k(f_k) + S_k \tag{5.1}$$

where $C_k(f_k)$ is the collision operator. Integrating this equation respect the parity moments $(1, \mathrm{v}^2)$ particle and energy transport equations are obtained

$$\frac{\partial n_k}{\partial t} + \nabla \cdot (n_k u_k) = S_k \tag{5.2}$$

$$\frac{\partial}{\partial t}\left(\frac{1}{2} n_k m_k u_k^2 + \frac{3}{2} p_k\right) + \nabla \cdot \left[\left(\frac{1}{2} n_k m_k u_k^2 + \frac{5}{2} p_k\right)\vec{u}_k + \vec{\vec{\Pi}}_k \cdot \vec{u}_k + \vec{q}_k\right] = \left(e_k n_k \vec{E} + \vec{F}_{k1}\right) \cdot \vec{u}_k + Q_k + P_e \tag{5.3}$$

In order to obtain the energy equation with the extra term corresponding to the nonaxisymmetric case, a simplified version of equation 5.3, with no energy source and no global energy flow will be used. Moreover, for simplicity only electron-ion plasma will be discussed. The corresponding equations for electrons and ions are as follow

$$\frac{\partial}{\partial t}(p_e) + \nabla \cdot \vec{Q}_e = -Q_i + \vec{E} \cdot \vec{J} - \vec{u}_i \cdot (\vec{F}_{i1} + n_i e_i \vec{E}) \tag{5.4}$$

$$\frac{\partial}{\partial t}(p_i) + \nabla \cdot \vec{Q}_i = Q_i + \vec{u}_i \cdot (\vec{F}_{i1} + n_i e_i \vec{E}) \tag{5.5}$$

Taking small gyroradius expansion up to second order to evaluate the energy exchange term $\vec{u}_i \cdot (\vec{F}_{i1} + n_i e_i \vec{E})$ the next expression is obtained for the surface average

$$\left\langle \vec{u}_i \cdot (\vec{F}_{i1} + n_i e_i \vec{E}) \right\rangle = -e_i \left\langle n_i u_{i2} \cdot \nabla V \right\rangle \frac{\partial \varphi}{\partial V} + \left\langle \vec{u}_{i1} \cdot (\vec{F}_{i1} + n_i e_i \vec{E}) \right\rangle \quad , \tag{5.6}$$

where $\varphi(V)$ is the electrostatic potential and the subscripts in the ion flow velocity denote the order of the gyroradius. Using Hamada coordinates (V, θ, ξ) the magnetic field $\vec{B}$ can be expressed as $\vec{B} = \psi' \nabla V \times \nabla \theta - \chi' \nabla V \times \nabla \xi$ with $\psi' = \vec{B} \cdot \nabla \xi$ the toroidal component of the magnetic field and $\chi' = \vec{B} \cdot \nabla \theta$ the poloidal one. The ion flow velocity $\vec{u}_{i1}$ is given by

$$\vec{u}_{i1} = (u_{\|i1} / B)\vec{B} + \vec{u}_{\perp i1} \tag{5.7}$$

where $u_{\|i1}$ is the parallel component and $\vec{u}_{\perp i1}$ includes both drift $\vec{E} \times \vec{B}$ and diamagnetic velocities

$$\vec{u}_{\perp i1} = \frac{\vec{B}\times\nabla V}{B^2}\frac{\partial\varphi}{\partial V} + \frac{\vec{B}\times\nabla V}{n_i m_i \rho_i B}\frac{\partial p_i}{\partial V} \tag{5.8}$$

The factor $\langle n_i \vec{u}_{i2}\cdot\nabla V\rangle = \Gamma_i$ is simply the ion radial particle flux and it can be written as

$$\langle n_i \vec{u}_{i2}\cdot\nabla V\rangle = -\left(\frac{1}{e_i\chi'}\right)\langle\nabla V\times\nabla\theta\cdot(F_{i1}+n_i e_i E)\rangle + \left(\frac{1}{e_i\chi'}\right)\langle\nabla V\times\nabla\theta\cdot\nabla\cdot\vec{\vec{\Pi}}_i\rangle \tag{5.9}$$

Finally, after some algebra, the factor $\langle\vec{u}_i\cdot(\vec{F}_{i1}+n_i e_i\vec{E})\rangle$ is expressed as,

$$\langle\vec{u}_i\cdot(\vec{F}_{i1}+n_i e_i\vec{E})\rangle = \left(\frac{u_{pi}}{\chi'}\right)\langle\vec{B}\cdot(\vec{F}_{i1}+n_i e_i\vec{E})\rangle - \frac{\partial p_i/\partial V}{n_i e_i\chi'}\langle\nabla V\times\nabla\theta\cdot(\vec{F}_{i1}+n_i e_i\vec{E})\rangle - e_i\Gamma_i^{na}\frac{\partial\varphi}{\partial V} \tag{5.10}$$

where $\Gamma_i^{na} = \left(\frac{1}{e_i\chi'}\right)\langle\nabla V\times\nabla\theta\cdot\nabla\cdot\vec{\vec{\Pi}}_i\rangle$ is nonambipolar, nonaxisymmetric ion particle flux. As can be seen, this factor arises from the toroidal component of the viscosity. Indeed, in the tokamak case, this term vanishes and only the neoclassical axisymmetric term of equation 5.10, $\frac{\partial p_i/\partial V}{n_i e_i\chi'}\langle\nabla V\times\nabla\theta\cdot(\vec{F}_{i1}+n_i e_i\vec{E})\rangle$, remain. Finally, introducing these calculations in equation 5.4 the transport energy equation for electrons yields

$$\frac{\partial}{\partial t}(P_e) + \nabla\cdot\vec{Q}_e = -Q_i + \vec{E}\cdot\vec{J} - e\Gamma_e^{na}E_r \tag{5.11}$$

where $\vec{Q}_e = \vec{Q}_{asy} + \vec{Q}_t$, being $\vec{Q}_{asy}$ the asymmetric heat flux and $\vec{Q}_t$ is the total flux corresponding to the axisymmetric neoclassical flux and the anomalous one.

In order to calculate the electric field explicitly several methods are available. Usually, accurate methods are expensive in computational time, so it is difficult to analyze the interaction between neoclassical transport and other parameters of the plasma. Taking account the fact that the DFEN developed the code PRETOR-Stellarator to perform full simulations of stellarator plasmas an algebraic and faster method was selected to perform these calculations.

The method we selected is based in solving the ambipolar equation

$$\sum_k z_k\Gamma_k^{na} = 0 \tag{5.12}$$

where k denotes each specie of the plasma and z_k its electric charge. The nonambipolar flux Γ_k^{na} can be expressed as [Has85]

$$\Gamma_k^{na} = \frac{1}{V'(\rho)} \int \frac{d\theta}{2\pi} \int d\varepsilon d\mu \langle \dot{\rho} \rangle \tau_b f_k \tag{5.13}$$

where ε and μ are the energy and the magnetic moment respectively, $V'(\rho)$ is $\partial V / \partial \rho$ with V the volume inside the flux surface ρ, $\dot{\rho}$ is the bounce-averaged radial drift, and τ_b is the bounce time of a particle trapped in an helical well. The distribution function f_k can be obtaining by solving the linerialized bounce-averaged drift kinetic equation. Finally the expression for the radial asymmetric neoclassical flux associated with helical-ripple trapped particles Γ_k^{na} and heat flux Q_k^{na} of electrons (k=e) and ions (k=i) are given by [Has85]

$$\Gamma_k^{na} = -\varepsilon_t^2 \varepsilon_h^{1/2} \nu_{tj}^2 n_k \int_0^\infty x^{5/2} e^{-x} \tilde{\nu}_k \frac{A_k(x, E_r)}{\omega_k^2(x, E_r)} dx \tag{5.12}$$

$$Q_k^{na} + \frac{5}{2} \Gamma_k^{na} T_k = -\varepsilon_t^2 \varepsilon_h^{1/2} \nu_{tj}^2 n_k T_k^2 \int_0^\infty x^{7/2} e^{-x} \tilde{\nu}_k \frac{A_k(x, E_r)}{\omega_k^2(x, E_r)} dx \tag{5.13}$$

with

$$x = m_k v_{tk}^2 / 2T_k \tag{5.14}$$

$$A_k(x, E_r) = n_k' / n_k - Z_k e E_r / T_k + (x - 3/2) T_k' / T_k \tag{5.15}$$

$$\tilde{\nu}_k(x) = \nu_k^0 x^{-1.5} \varepsilon_h^{-1} \left\{ \left[(1 - 1/2x) erf(x^{1/2}) + \frac{e^{-x}}{(\pi x)^{1/2}} \right] + \bar{Z}_k \right\} \tag{5.16}$$

$$\omega_k^2(x, E_r) = 4.21 \frac{\tilde{\nu}_k^2}{F_m / F_s} + 1.5 (\varepsilon_t / \varepsilon_h)^{1/2} (\omega_E + \omega_{Bk})^2 \tag{5.17}$$

$$+ (\varepsilon_t / \varepsilon_h)^{3/2} \left[\frac{\omega_{Bk}}{4} + 0.6 |\omega_{Bk}| \tilde{\nu}_{tk} (\varepsilon_t / \varepsilon_h)^{3/2} \right]$$

$$\nu_k^0 = \frac{4\pi e^4 n_k \ln\Lambda}{m_k^2 v_{tk}^3} \tag{5.18}$$

Here ε_t is the toroidal ripple, ε_h is the helical ripple modulation, n_k and T_k are the plasma density and temperature of each specie k, v_{tk} is the thermal velocity of the specie k, ω_E is the $\vec{E} \times \vec{B}$ drift frequency and ω_B is the ∇B drift frequency. The prime denotes the derivative with respect the radial coordinate.

In equation 5.17 the first term is the contribution from the $1/\nu$ collisional regime, the second term comes from the non-resonant collisonless detrapping regime, the third term

comes from the resonant superbanana regime, and the fourth one comes from the resonant superbana plateau regime. The factor F_m/F_s takes account of the multi-helicity case and is quite important in TJ-II because of its complicated magnetic field structure. The validity of equation 5.17 for the multi-helicity case has been benchmarked in reference [Hir86]. Equation 5.12 reproduces correctly Monte Carlo simulations [Gar04] with no time consuming.

Equations 5.12 and 5.13 have been introduced in PRETOR-Stellarator code in order to elucidate whether they can be used to analyze neoclassical transport for both TJ-II and LHD devices. The results will be described in the following sections.

5.3 Study of the neoclassical transport in TJ-II

5.3.1 TJ-II density and temperatures profiles

In order to compare the model previously described with Monte Carlo results [Tri01], PRETOR-Stellarator is used with experimental fixed density and temperature profiles. Two different cases will be used for the neoclassical estimations, corresponding to high and low densities, both with the same heating power (P_{ECRH}=300 kW). In both cases an almost flat ion temperature profile is taken, which is similar to the obtained experimentally. The electron density and temperature profiles used in both simulations are plotted in Figure 5.2.

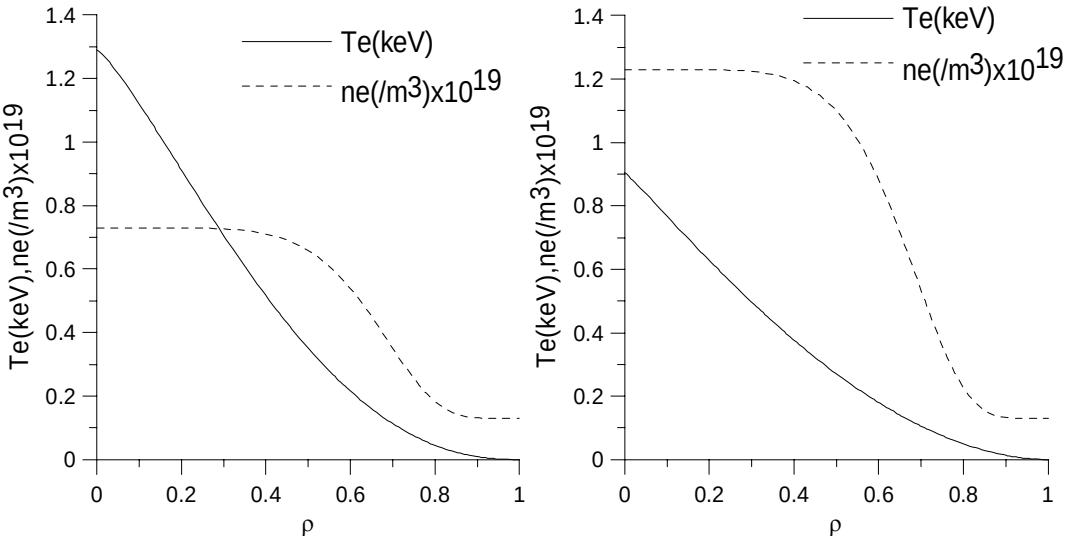

Figure 5.2 Density and temperature profiles in the case of low density scenario (left) and high density scenario (right).

The composition of the TJ-II plasmas in these shots is hydrogen and we have included 1% of carbon concentration as an impurity.

5.3.2 Neoclassical calculations

Two simulations are performed for low and higher density regimes. In figure 5.3 neoclassical electron and ion fluxes dependence on electric field at ρ=0.25 are given in the high density case (left) and low density case (right). In both cases there is only one root of the ambipolar equation. This situation is a common feature in TJ-II scenarios [Tri01] due to the ratio $Te/Ti \gg 1$, since there is no heating power for the ions. This ratio is the key point for the transition from one solution of the ambipolar equation to three solutions. The high electron fluxes observed in figure 5.3 are mainly due to high electron temperature gradients and in the case of ions, fluxes are due to electric field, because ion density and temperature are almost flat. These results are in concordance with the ones obtained previously by means of Monte Carlo techniques.

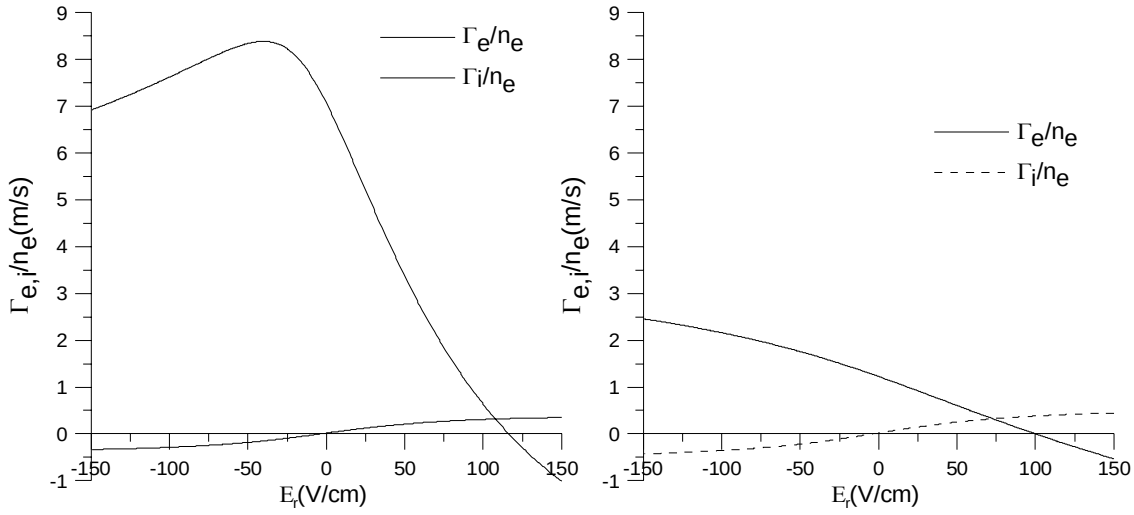

Figure 5.3 Neoclassical electron and ion fluxes dependence on electric field at ρ=0.25 in the high density case (left) and low density case (right).

The ambipolar equation is solved for every point in the plasma and the electric field obtained is plotted in Figure 5.4. There is a strong positive electric field at the center and a small negative one at the edge. This is a typical feature in stellarators with the same size than the TJ-II and heated with ERCH [Tod02] [Maa00], although in the TJ-II there is only one solution of the ambipolar equation, so the transition between positive (electron root) and negative (ion root) electric field should be soft according to this model. Comparing the results obtained with the model applied in this study and the ones obtained with Monte Carlo techniques, we can conclude that for these concrete shots results are different. In the

Monte Carlo case, the electric field obtained for the low density case is much higher in the central region (up to three times). In the high density case this value reduces to two times.

Perpendicular electron diffusivities (corresponding to diagonal terms of the transport matrix) for low density case are shown in Figure 5.5. Maximum values for electron diffusivities are 2.0 m^2/s and 5.5 m^2/s, in the high and the low density cases respectively. Comparing these results with previous studies made with Monte Carlo techniques, smaller electric field and higher thermal diffusivities are obtained when the model described in this paper is applied, although in both cases there is only one solution of the ambipolar equation. The reason why higher neoclassical diffusivities are obtained is that, with this model, the electric field obtained is lower, and in the neoclassical transport, a large electric field reduces such transport.

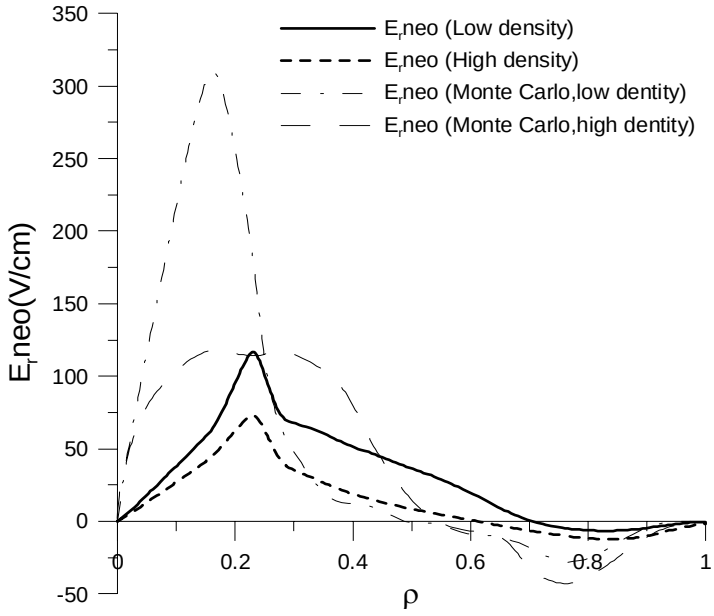

Figure 5.4 Comparison of neoclassical electric field (E_r^{neo}) obtained in this study with previous results using Monte Carlo techniques [Tri01] in the case of low density and high density scenarios.

From previous electron transport analysis [Fon01], the obtained central electron thermal diffusivities are in the range $4 < \chi_e < 6$ m^2/s for the standard shots and $2 < \chi_e < 3$ m^2/s for the enhanced confinement shots. Comparing these values with the neoclassical thermal diffusivities in the center obtained in the #2562 study, one can conclude that thermal transport in the plasma core is neoclassical in the enhanced heat confinement

shots. However in the standard shots the situation is not clear because central neoclassical values seem to be lower than the experimental ones. This issue will be clarified in next chapters.

The reason for the existence of only one solution of the ambipolar equation is that in general, the TJ-II works in the low collisionality regime in the center, because of the typical low ion temperatures and densities. Nowadays NBI injector has been installed and will be fully operative soon. In this case higher ion temperatures can be expected and higher ion collisionality regime can be obtained. In order to study this scenario, we have ran a shot in PRETOR-Stellarator with the same density and electron temperature profile than in the low density case previously used but with higher average ion temperature.

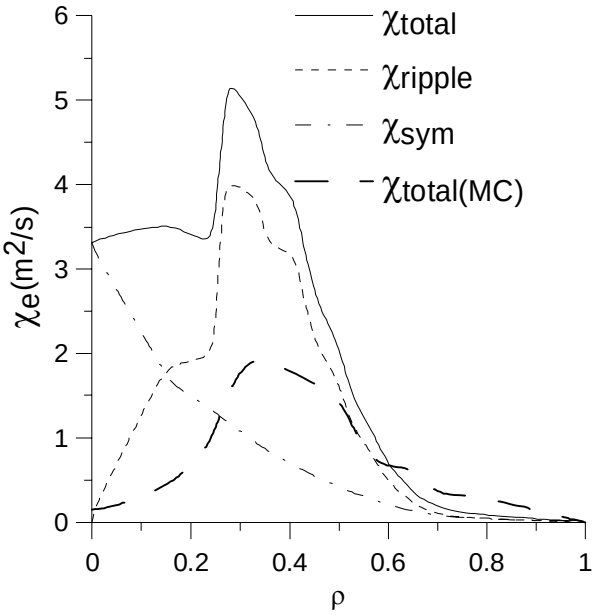

Figure 5.5 Comparison of neoclassical thermal diffusivities obtained in this paper with previous results using Monte Carlo(MC) techniques [Tri01] in the low density case for TJ-II.

The electron and ion fluxes obtained at r=a/4 are shown in Figure 5.6. In this case there are three roots of the ambipolar equation. The two extreme solutions are stable whereas the middle one is unstable. Therefore the electric field might suffer a sudden transition between positive to negative values at a point close to r =a/2. Besides, the electric field has a critical behavior, and depending of the density, sudden transition between electron and ion root might appear at the plasma core. These characteristics could affect not just neoclassical transport but anomalous transport too. Thus, more experimental studies should be done with NBI heating to analyze whether these results concerning to the

electric field are correct, and which are the effect over another parameters of the plasma. Anyway, it is worth to point out that, according to the model applied in this study, in this high ion temperature scenario the TJ-II would have the same behavior as others stellarator devices.

Finally, and according to the results presented, a new contribution of this thesis is that neoclassical transport in the TJ-II device can be analyzed by means of the model presented with very few consuming time. The results, although approximated, are in concordance with other studies and experimental data [Cas04].

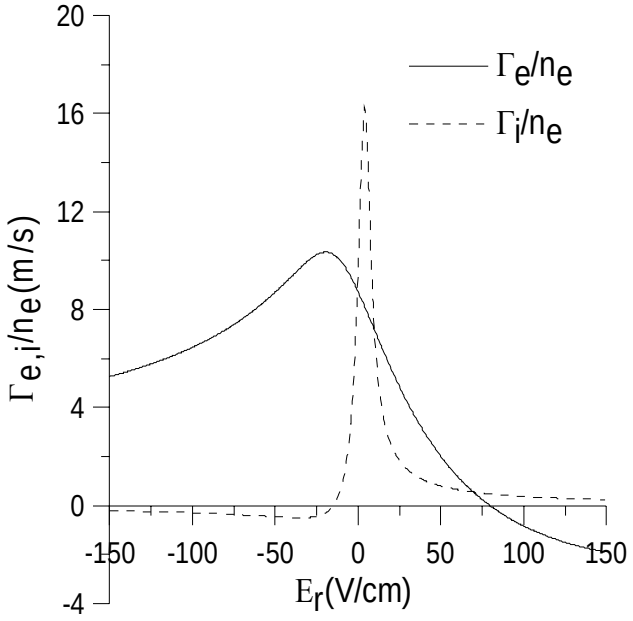

Figure 5.6 Normalized electron and ion neoclassical fluxes in the high ion collisionality regime for r=a/4.

5.4 Study of the neoclassical transport in LHD

5.4.1 LHD density and temperatures profiles

In order to use PRETOR-Stellarator not only to simulate TJ-II plasmas but LHD plasmas too (and possibly another Stellarators devices), it was decided to analyze the goodness of the previous neoclassical model to reproduce correctly some neoclassical results obtained in the LHD. The neoclassical diffusivities and electric field of the LHD shot #32940 [Ida03] are analyzed and compared with experimental data obtained by the

charge exchange spectroscopy (CXS). This shot is produced under the condition of major radius R=3.75m (the standard configuration), magnetic field strength of B≈1.52 T, average minor radius of a=0.51m and the species are Hydrogen and Helium. The experimental electron density and temperatures profiles used are shown in Figure 5.7.

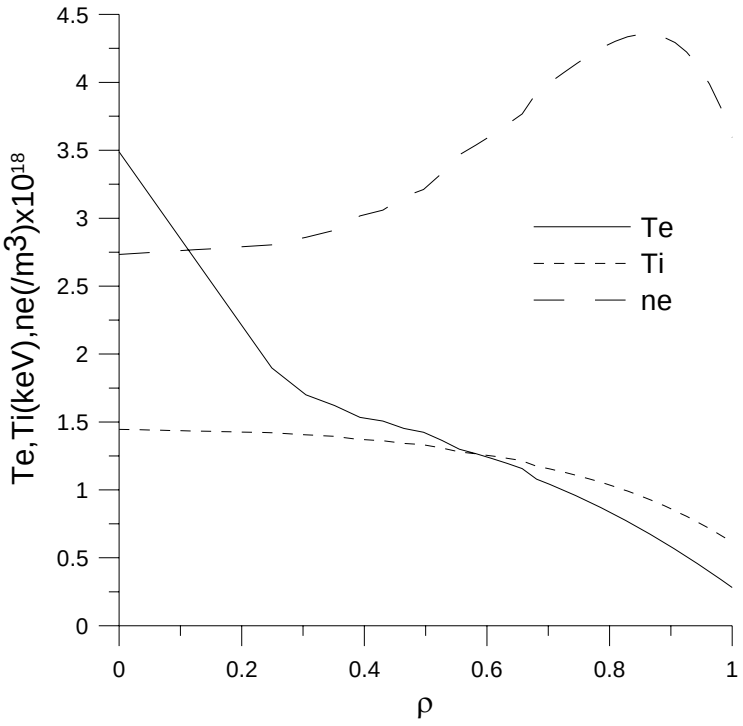

Figure 5.7 #32940 shot density and temperature profiles used in LHD simulations.

5.4.2 Neoclassical calculations

The electric field and neoclassical electron and ion fluxes at ρ=0.25 are given in figure 5.8. Neoclassical electric field (E_r^{neo}) has high positive values in the central region ($E_{r\,\max}^{neo}$≈130V/cm) and small positive values as far as normalized minor radius ρ=0.4. From this point to ρ=1 the electric fields tends to increase again obtaining high positive values. Experimental electric field, measured with the CXS, has a very similar profile, although central calculated value is a bit higher than experimental one and beyond ρ=0.4 tends to be smaller. Nevertheless, the global profile of the electric field is quite well simulated with the model used along this study. These results are quite comparable to the ones obtained for the same shot but using PROCTR code [Fun02]. However, one possible reason for these discrepancies is the existence of anomalous transport that is not

automatically ambipolar and, therefore, the electric field cannot be obtained only from imposing the ambipolar condition to neoclassical fluxes. Some other reasons are that ion temperature profile and ion and impurity density profiles are not completely determinate by experimental data. This fact is very important on the determination of the electric field sign mainly at the edge of the plasma. Thus, both experimental and calculated electric field values should be taken with caution in the region ρ>0.4.

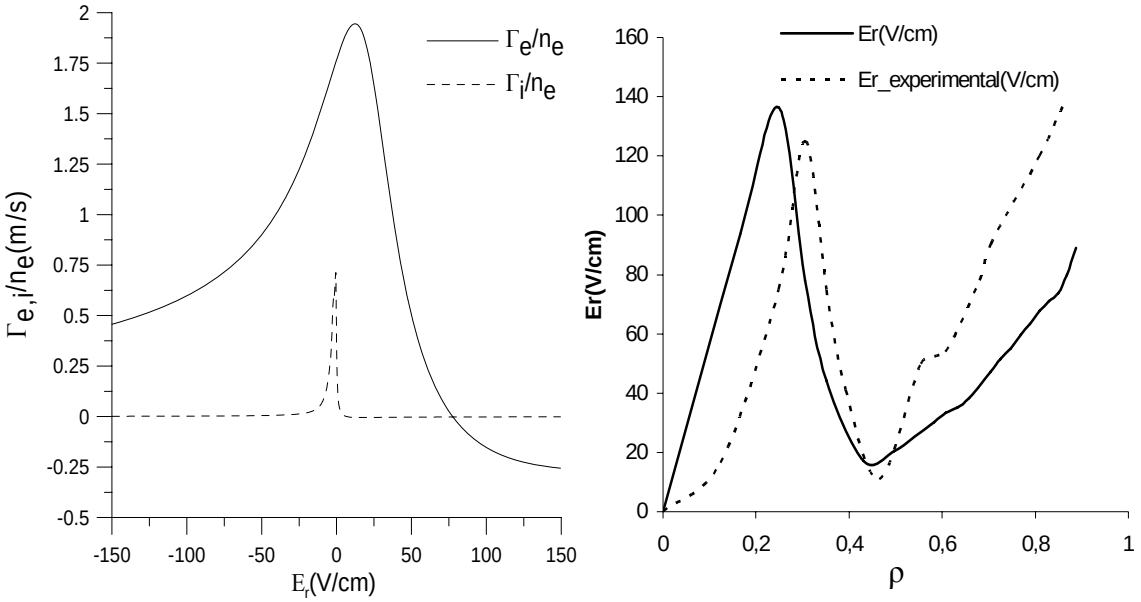

Figure 5.8 Calculated neoclassical electron and ion fluxes at ρ=0.25 (left). Neoclassical and experimental electric field (E_r) for #32940 LHD shot (right).

On the other hand, from figure 5.8 (left) one can deduce that in this shot the ambipolar equation seems to have just one solution. This characteristic is not very usual in the LHD and this result must be taken with some care, because the number of solutions of the ambipolar equation depends strongly on the ion density, which is not completely determinate in this shot. Thus, unlike the TJ-II scenarios, the existence of one solution for the ambipolar equation seems to be circumstantial.

Thermal electron diffusivities are show in figure 5.9. Neoclassical thermal diffusivity, χ_e^{neo}, is smaller than the experimental one, $\chi_e^{\exp}$, by a factor of 2 in the region 0.2<ρ≤0.7, and probably higher in central region. Although this shot correspond to an Internal Transport Barrier scenario (with low density and high electron temperatures) the neoclassical diffusivities values seem to be far away from the experimental (and therefore anomalous) ones in the region ρ>0.2. So, even in the high temperature shots, it seems that neoclassical transport may be only dominant at the plasma core. Comparing these results

with the previously ones obtained in the TJ-II #2562 shot one can conclude that there similarities in both devices. Further analysis will be done in thesis in order to check these preliminary results.

The values obtained are comparable to the ones obtained for the same shot by means of another transport codes [Fun02], however PRETOR-Stellarator transport code seem to overestimate the symmetric part of the neoclassical diffusivity at he plasma core.

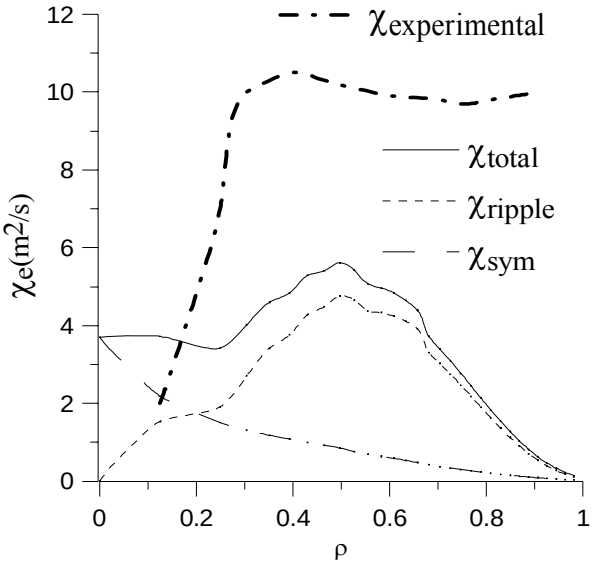

Figure 5.9 Neoclassical and experimental electron thermal diffusivities for #32940 LHD shot.

5.5 Conclusions

Neoclassical transport models for the radial electric field and diffusivities have been implemented in PRETOR-Stellarator code which has been developed in the "Departament de Física i Enginyeria Nuclear". The results for TJ-II standard shots show an electric field with a high positive value at the plasma center and a small negative value at the edge with only one solution of the ambipolar equation, but this situation may change in the future with NBI heating, because ion temperature will increase and three solutions will be possible. These results also show that transport in the plasma center is probably neoclassical for ECRH heated plasmas in the Enhanced Heat Confinements shots, and outside, it is anomalous.

Previous studies of neoclassical transport for the same conditions were made with Monte Carlo techniques. Some of the conclusions of those studies were that probably the real electric field obtained was too large and thermal diffusivities were too low due to the approximations made for the calculations. Comparing the results of this thesis with previous ones, smaller electric field and higher diffusivities are obtained in a wide region in the plasma core and according to that, the main conclusions of this thesis seem to be correct, although in both cases, results close to the edge are doubtful due to low collisionality. In fact, the transport coefficient obtained from the analysis of experimental results rises strongly close to the edge, differently of what it is obtained from the neoclassical analysis.

Anyway, the electric field results obtained in this thesis are quite similar to the experimental shots obtained with similar temperature and density profiles in TJ-II [Cas04]. In this case one can conclude that, as a first approximation to the neoclassical transport problem, the model presented in this thesis is acceptable. Therefore, a new contribution of this thesis is that, as a first approximation to the neoclassical transport, we have a fast routine able to calculate electric field, perpendicular and off-diagonal neoclassical transport coefficients for TJ-II device.

A study of the LHD #32940 shot has been done with PRETOR-Stellarator too. The electric field obtained is larger than the experimentally measured in the plasma core but their profile are quite similar in the whole plasma radius. This result is similar to the ones obtained with other codes [Fun02]. The ambipolar equation has only one solution for this configuration. This is not a very usual result, because three solutions are expected if the ion temperature is high. However these solutions depend strongly on the ion density, which is not automatic determined by the experiment. Therefore these results must be taken with care. Anyway, the solution obtained in this thesis wouldn't change too much in the presence of three solutions of the ambipolar equation, since, as can be seen in figure 5.8, the large and positive solution would be approximately the same one.

The calculated neoclassical diffusivity in this thesis is smaller than the experimental one by a factor of 2 in the $0.2<\rho\leq0.7$ range and higher in the $0<\rho\leq0.2$. These results are similar to the analysis of the same shot performed elsewhere [Ida03], however, in this work the symmetric part of the neoclassical transport seems to be overestimated in the plasma center. In the future, more LHD studies will be done in order to check the goodness of the code to simulate LHD shots.

As a final conclusion, a new contribution of this thesis is that the neoclassical transport model introduced in PRETOR-Stellarator allows performing neoclassical

transport simulations and analysis with much less computer time than other techniques. The results, although not so accurate as the ones obtained with Monte Carlo techniques, are closely enough to the experimental data, allowing fast analysis of dependences between the plasma variables. It is worth to point out that, as a new contribution of this thesis, the model presented and introduced in PRETOR-Stellarator is able to simulate neoclassical transport in both LHD and TJ-II. This feature allows comparing neoclassical results in both devices. This advantage will be used extensively in next chapters.

Chapter 6

Preliminary study of anomalous electron heat transport in TJ-II

6.1 Introduction

The study of plasma transport is very important in plasma physics as well as in engineering reactors design. The knowledge of the main characteristics of energy and particle transport could lead to a complete description of the plasma in a thermonuclear reactor as well as in space plasmas. These studies are particularly important in the design of the future commercial reactors since these designs depend strongly on the temperature, density and beta needed for plasma fusion. Therefore, the knowledge of the transport behaviour seems to be and important issue.

The heat transport in tokamaks and stellarators can be divided into two really different categories: neoclassical and anomalous transport. Neoclassical transport is derived from collisional transport in toroidal geometry and it is well formulated. As it has been shown in the previous chapter it can be studied using different techniques, e.g. Monte Carlo techniques as well as drift kinetic solvers. On the other hand, plasma turbulence (anomalous transport) occurs inside the plasma when it is driven away from its equilibrium state. The further is the plasma away from equilibrium the anomalous transport tends to be stronger. Many mechanisms in a magnetic fusion device enhance this kind of transport, as Neutral Beam Injector (NBI) or Electron Resonant Cyclotron (ERC) heating. However, a

universally occurring departure from the equilibrium is the existence of spatial gradients across the magnetic surfaces and the existence of intrinsic fluctuations in the plasma.

It seems clear from the analysis of experimental data obtained in tokamaks and stellarators devices that heat losses due to neoclassical transport tend to be much smaller compared to anomalous ones. So the study of turbulent transport is an extremely important issue in plasma physics.

Unfortunately there is no global formulation of the turbulent transport problem in plasma physics, so usually the problem of turbulence is treated by adding an extra term, χ_{an}, to the neoclassical diffusion, χ_{neo}, in the heat diffusion equation, as showed in equation 6.1. This method must be understood as a first approximation to the problem, since there is no general framework for the turbulence problem in any research field.

$$Q_e = -n_e \left(\chi_{an} + \chi_{neo} \right) \left\langle \left| \nabla \rho \right|^2 \right\rangle \frac{\partial T_e}{\partial r} \tag{6.1}$$

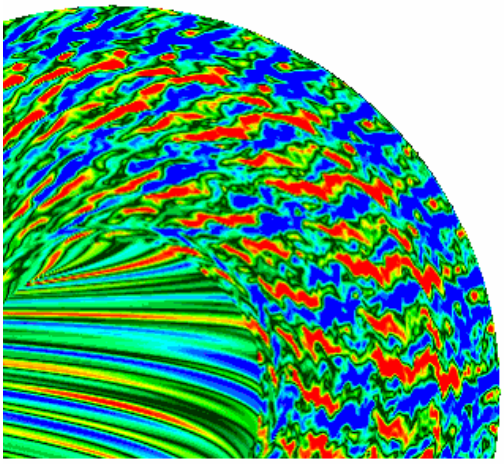

Figure 6.1 Plasma temperature eddies (in normalized units) from a plasma turbulence simulation [PPP05b].

The main technique to study anomalous transport in thermonuclear plasmas is to introduce some expressions for the anomalous diffusivity (transport models) and to compare the results obtained for temperature and densities with the experimental ones. The transport models can be obtained from quite different techniques. A possibility is to analyze the experimental electron temperature results and make a scaling for the anomalous diffusivity which depends on various important parameters of the plasma, e.g. electron temperature, density, total power deposition or major radius. These models are

called pseudo-experimental. Another possibility is to use dimensionless analysis of local scaling expression for thermal diffusivity. This method is suitable in order to extrapolate the results of the present fusion devices to future reactors. Bohm and Gyro-Bohm scaling belong to this type of analysis. Finally, there are some transport models derived from theoretical research e.g. drift wave models, Ion Temperature Gradient (ITG) models or Electron Temperature Gradient (ETG) models [Hor03]. Theoretical models can be derived from the analysis of the fluctuations inside the plasma. In the drift wave case model, the fluctuations arise from the analysis of the magnetic and electric field behaviour. But, in fact, more fluctuations are present in the plasma as the Rayleigh-Taylor fluctuation. It is worth to point out that the existence of extremely high temperature gradients from the core plasma to the outer wall implies a high source of instabilities, as can be seen in figure 6.1. ITG can be applied in the case of high ion temperature gradients, whereas in electron transport, ETG is more suitable.

Usually in the "Departament de Física i Enginyeria Nuclear" the anomalous transport analysis have been carried out using the LHD pseudo-experimental model [Die02]. With this model, temperature simulations obtained were reasonably good compared with the experimental data. However, in the Enhanced Transport Scenarios, this model had to be modified in order to get good agreement with experimental data. Thus, in order to get a transport model suitable in a wide range of experimental conditions, a complete study of anomalous transport must be done.

Some studies of this type have been done previously for the TJ-II using PRETOR-Stellarator code as well as PROCTR code, obtaining comparable results with both codes [Die02]. In this thesis, these studies will be improved by using some new transport models. Therefore, some new electron heat diffusion models have been added to PRETOR-Stellarator transport code in order to check the goodness of each one to simulate TJ-II shots. The results could be interesting in order to improve the transport calculations in TJ-II or confirm the validity of the usual model used. The implementation of some theoretical transport models may also help to enlarge the validity of these theories developed for tokamak plasmas which have not been used in stellarators plasmas.

For this purpose two different discharges have been simulated to test the validity of the models. One of the two discharges is a typical discharge of TJ-II and the second one is an enhanced heat confinement one.

The models implemented are the following:

- LHD pseudo-experimental
- LHD local
- LHD power
- W7X
- W7-AS
- Electromagnetic (Em)
- Electrostatic (Es)

The first five models are experimental ones and the last two models are theoretical ones. Both theoretical models are drift wave turbulence (DWT) models.

The aim of this study is to get some preliminary results about the electron heat transport physics in the TJ-II in order to understand the key mechanism for this kind of transport. It is also important this study in order to know how electron heat transport may change from shots with high density and low temperature to the called Enhanced Transport Scenarios, which have very low densities and high peaked temperatures. These last scenarios will be studied deeper in next chapter but a sketch of their structure will be given in this chapter.

6.2 Experimental data

The experimental data is collected from TJ-II stellarator. Several shots of TJ-II stellarator have been used previously to validate the modifications introduced in PRETOR-Stellarator code leading to good results. TJ-II [Ale90] is a medium size four periods stellarator (heliac type, $B \leq 1.2T$; $R=1.5$ m; $\langle a \rangle \leq 0.2$ m) with a wide rotational range $0.9 \leq \iota(0)/2\pi \leq 2.2$ in low, negative shear configurations ($\Delta q/q < -6\%$). The TJ-II plasmas are produced and heated with ECRH, two gyrotrons of 300 kW each at 53.2 GHz, 2^{nd} harmonic, X-mode polarization.

In this case two discharges from a density scan are selected. The first one, #2559, is a "standard" one whereas the other one, #2562, corresponds to an enhanced heat confinement shot [Cas02]. The data used is the electron temperature and density measured by a multi-point Thompson scattering [Her00]. The electron and density profiles are given figure 6.2 and a summary of both shots is showed in table 6.1.

As can be seen from figure 6.2 the electron temperature is higher in shot #2562 with a high gradient at effective radius $\rho \approx 0.1$. For effective radius greater than 0.15, both temperature profiles are very similar. The #2559 shot electron temperature gradient is

roughly constant throughout the entire plasma radius. The density is hollow [Cas00] in the centre of the plasma radius, this feature is clearer in shot #2562 corresponding to the enhanced heat confinement. The density for effective radius beyond 0.5 is similar in both shots whereas in shot #2562 it is lower for the inner radius.

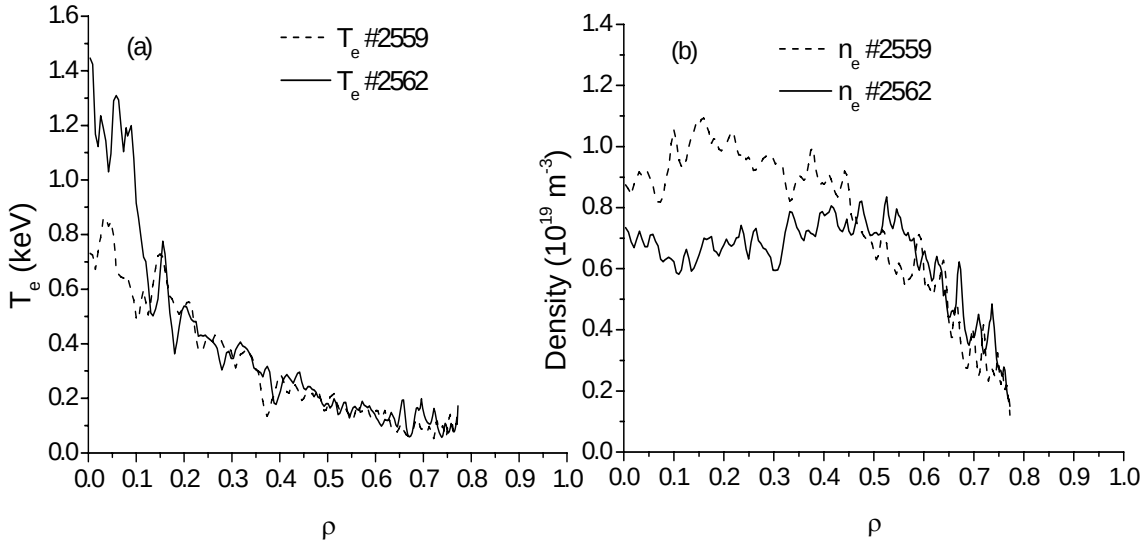

Figure 6.2 Electron temperature (a) and density (b) profiles collected from Thompson scattering for shots #2559 and #2562.

Plasma parameter	Shot #2559	Shot #2562
Major Radius (m)	1.5	1.5
Minor radius (m)	0.18	0.18
Central electron temperature (keV)	0.72	1.45
Average electron temperature (keV)	0.36	0.52
Central electron density ($\times 10^{19}\, m^{-3}$)	0.88	0.74
Average density($\times 10^{19}\, m^{-3}$)	0.86	0.72
Confinement time (ms)	1.42	1.55
Radiated power (kW)	81	77

Table 6.1 Plasma characteristics for #2559 and #2562 TJ-II shots.

The plasma, composed by hydrogen, is heated with 300 kW of ECR heating provided by one gyrotron and transmitted to the plasma by a quasi-optic transmission line. The power deposition has been modelled as ($\rho_{wid} = 0.2$),

$$P_{ECH} \propto \exp(-(\rho / \rho_{wid})^2) \tag{6.2}$$

which is a good fit for the experimental data [Egu03].

6.3 Implemented Models

6.3.1 LHD pseudo-experimental [Sud90]

In this case there are three fitting parameters, one of them controls the central temperature and the other two serve to fit the shape. This model calculates the experimental thermal diffusivity at ρ=2/3, scaled to the LHD confinement time and then normalizes the diffusivity to this value and gives a thermal diffusivity shape.

$$\chi_e = C_1 \chi_{2/3} \frac{1+f_{esc}(\rho)}{1+f_{esc}(2/3)} \qquad \chi_{2/3} = \frac{W_e(2/3)}{\tau^{LHD} n(2/3) \nabla T_e(2/3) S(2/3)} \tag{6.3}$$

$$f_{esc} = \begin{cases} C_2 e^{-\frac{1-\rho}{\Delta\rho}} \\ C_2 \left[1 - \frac{1}{1+e^{\rho/C_3 - 1}/\Delta\rho} \right] \end{cases}$$

where S is the magnetic surface. The τ^{LHD} is the LHD scaling time defined as,

$$\tau^{LHD} = 0.17 < n_e >^{0.69} B_T^{0.84} a^2 R^{0.75} P_{ECH}^{-0.58}$$

In this case n_e is expressed in 10^{20} m^{-3}, B_T in T, R and a in m and P_{ECH} in MW.

6.3.2 LHD local dependence [Yam92]

In this case there are four parameters to adjust thermal diffusivity. One of them is fixed (*fimpre*), and it is used to adjust global confinement, the other three are adjustable with the parameters screen of PRETOR-Stellarator in order to obtain good agreement with electron temperature profile.

$$\chi_e = 15.8 B_T^{-2} R^{-0.4} \left(\frac{n_e}{1 \cdot 10^{20}} \right)^{-0.26} \left(\frac{T_e}{1 \cdot 10^3} \right)^{1.38} fimpre^{-2.38} \frac{1 + Ct1 \rho^{Ct2}}{1 + Ct1 \cdot Ct3^{Ct2}} \tag{6.4}$$

6.3.3 LHD power dependence [Yam92]

This model is similar to the previous one but has heating power dependence. Here the diffusivity shape is controlled by two external parameters.
If *Ct1*=1 then

$$\chi_e = 15.8 B_T^{-2} R^{-0.4} Ct2^{-2.38} \left(\frac{n_e}{10^{20}}\right)^{-0.26} \left(\frac{T_e}{10^3}\right)^{1.38} \tag{6.5}$$

If *Ct1*≠ 1 then

$$\chi_e = 15.8^{Ct1} 1.47^{1-Ct1} Ct2^{-(1+1.38Ct1)} B_T^{-(0.84+1.16Ct1)} R^{-0.75+0.35Ct1} P_{elec}^{0.58-0.58Ct1} \left(\frac{n_e}{10^{20}}\right)^{-0.69+0.43Ct1} \left(\frac{T_e}{10^3}\right)^{1.38Ct1} \tag{6.6}$$

where the units are the same as the previous model.

6.3.4 W7-AS model [Rin90]

The model has only one parameter to fit the central temperature.

$$\chi_e = 0.64 \left(\frac{R0}{2}\right)^{-0.75} B_T^{-0.6} \iota_0^{-0.49} P_{elec.}^{0.76} \left(\frac{n_e}{1{\cdot}10^{20}}\right)^{-0.95} \frac{1}{Ct1} \tag{6.7}$$

It is worth to point out that in this case appears the rotational transform in the center.

6.3.5 W7X model [Yam92]

This model has three fitting parameters that multiply the W7X scaling.

$$\chi_e = \frac{2.4}{R} \left(\frac{2.2}{B_t}\right)^2 T_e^{3/2} \frac{1}{\left(1.1 - \left(\frac{\rho}{Ct1}\right)^{Ct2}\right)^{Ct3}} \tag{6.8}$$

It has a simple dependence on temperature and a geometrical factor that allows correcting the temperature shape.

6.3.6 Theoretical electromagnetic drift wave DWT [Hor88]

Electromagnetic drift wave models have been used successfully with tokamak devices. In this thesis, this kind of model has been extended to helical devices with the D_{EMh} factor which takes account of the helical ripples. Although it is a theoretical model, it has also two parameters to fit the experimental electron temperature profile. In this case the parameters allow weighting the importance of two types of transport, the toroidal and helicoidal-trapped particle transport,

$$\begin{aligned} \chi_e &= \frac{5}{2} D_{ANe} \\ D_{ANe} &= Ct1 D_{EMt} + Ct2 D_{EMh} \\ D_{EMt} &= \varepsilon_t^{1/2} \left(\frac{c}{\omega_{pe}} \right)^2 \omega_{bet} \\ D_{EMh} &= \varepsilon_h^{1/2} \left(\frac{c}{\omega_{pe}} \right)^2 \omega_{beh} \end{aligned} \tag{6.9}$$

where ε_t is the toroidal ripple, ε_h is the helical ripple, $\omega_{pe} = \sqrt{n_e e^2 / \varepsilon_0 m_e}$ is the electron plasma frequency, and the other two frequencies are the electron bounce frequencies defined as,

$$\omega_{bet} = \varepsilon_t^{1/2} v_t \frac{\iota}{R}$$
$$\omega_{beh} = \varepsilon_h^{1/2} v_t \frac{N}{R}$$

where v_t is the electron thermal velocity, $\iota = \frac{\iota}{2\pi}$, R the major radius and N the number of periods of the device.

6.3.7 Theoretical electrostatic drift wave DWT [Cru88]

In this case a first assumption has been made in order to calculate the coefficient. In this model it is necessary an average value of perpendicular wavelength, $k_\perp$, in order to obtain a dispersion relation. From experimental data [Woo90] it is known that $k_\perp \rho_s$ value does not change too much in electrostatic turbulence in $0<k_\perp \rho_s<1$ range, and in this case, the assumption $k_\perp \rho_s=1/3$ has been chosen following others studies done for the LHD [Yam92]. ρ_s is the Larmor radius with the ion sound velocity. This assumption has been made to take into account that the electrostatic models have long wavelength.

With this model the electron thermal diffusivity is calculated as:

$$\chi_e = \frac{5}{2} D_{ANe}\left(1 + 3C_{ei}\frac{L_n}{R}\eta_i f_{ITGth}\right)$$
$$D_{ANe} = Ct1 D_{CE} + Ct2 D_{TEt} + Ct3 D_{TEh} \tag{6.10}$$

In this case the parameter C_{ei} is taken as 0 because this part of the formula counts the contribution of the ion temperature gradient turbulence but in the shots used in this study the ion temperature profile is almost flat, so there is not ion temperature gradient. The other parameters serve to weight the importance of the different types of transport.
The different values of the different types of transport are the following:

$$D_{CE} = \max(D_{CCE}, D_{XCE})$$
$$D_{CCE} = \frac{\omega_{*e}}{k_\perp^2}\frac{\omega_{*e}}{\omega_{tet}} \tag{6.11}$$
$$D_{XCE} = \frac{\omega_{*e}}{k_\perp^2}\frac{\omega_{*e}}{\omega_{tet}}\frac{\nu_{ei}}{\omega_{tet}}$$

where $\omega_{*e}=k_\perp T_e/L_n eB$ ($L_n=n/n'$ is the characteristic density length) is the electron diamagnetic frequency; and $\omega_{tet}=v_t(\iota/R)$ is the electron transit frequency.

$$D_{TEt} = \min(D_{CTEt}, D_{DTEt})$$
$$D_{CTEt} = \varepsilon_t^{1/2}\frac{\omega_{*e}}{k_\perp^2} \tag{6.12}$$
$$D_{DTEt} = \varepsilon_t^{1/2}\frac{\omega_{*e}}{k_\perp^2}\frac{\omega_{*e}}{\nu_{efft}}$$

In this case $\upsilon_{efft}=\upsilon_{ei}/\varepsilon_t$ is the effective toroidal collision frequency.

$$D_{TEh} = \min(D_{CTEh}, D_{DTEh})$$
$$D_{CTEh} = \varepsilon_h^{1/2}\frac{\omega_{*e}}{k_\perp^2} \tag{6.13}$$
$$D_{DTEh} = \varepsilon_h^{1/2}\frac{\omega_{*e}}{k_\perp^2}\frac{\omega_{*e}}{\nu_{effh}}$$

In this case $\upsilon_{effh}=\upsilon_{ei}/\varepsilon_h$ is the effective helical collision frequency.

6.3.8 Models summary

Several electron heat diffusion models have been implemented in PRETOR-Stellarator. Three of them related to LHD scaling,

- LHD pseudo-experimental
- LHD local
- LHD power

The first one uses experimental heat diffusion coefficient at ρ=2/3 and fits the profile with a minor radius depending function. The second and third one use temperature and density dependences, however, LHD power model also uses total power heating dependence.

Two models related to W7AS scaling,

- W7AS
- W7X

The W7AS semi-local scaling is derived by using the total absorbed heating power P, and major radius dependence has been added in order to estimate the performance of different devices. The W7X model has simple temperature dependence and an adjustable minor radius fitting function.

Two drift waves models have been introduced too,

- Electromagnetic
- Electrostatic

The first one corresponds to magnetic field fluctuations, and the other one to electric field fluctuations.

6.4 Simulations

The simulation criteria are the following,

- The smoothed experimental electron density is introduced in the code, so electronic particle transport is not simulated.

- The ion density in the centre is comparable to maximum electron density and it is monotonic decreasing.
- The electron temperature is fixed at the plasma edge as 0.01 keV in both shots.
- All of the parameters are the same in any transport model case.
- The ion temperature is 0.12 keV in the center and 0.05 keV at the edge with a parabolic profile. In this situation temperature gradient is very small, corresponding to an almost flat profile.
- The ion temperature profile is simulated with the Hinton-Hazeltine [Hin76] model with Chang-Hinton [Cha82] correction.
- The parameters of the diffusion models are chosen to fit the experimental electron temperature central value.

The simulation results obtained for the #2559 simulation are shown in figure 6.3. As can be seen from the figure, electrostatic drift wave and LHD power dependence yield to quite flat temperature profiles. These results might be expected from other experimental results obtained in the LHD since in the simulations carried out for some shots with quite flat temperature (see next chapter) simulations performed with electrostatic models (or GyroBohm scaling) in the LHD were the best ones to fit experimental data. However, in the #2559 shot case, the global electron temperature gradient is appreciable even not being an Enhanced Heat Transport shot. Nevertheless, in the region where the temperature has no steep gradient, ρ>0.5, experimental and simulated temperatures have a similar profile in the electrostatic drift wave model case.

On the other hand, even that electromagnetic drift wave model tends to give an acceptable profile, mainly in the plasma core and in the outer part of the plasma, it seems that overestimates the global temperature gradient in the region $0.15 \le \rho \le 0.3$. This feature can be explained by the fact that electromagnetic models are related with ETG models and this kind of heat transport tends to enhance the existence of steep gradients. This characteristic will be clarified in next chapter. However, it is worth to point out that outside the region $0.15 \le \rho \le 0.3$ (even in the outer part of the plasma) experimental and simulated results are very similar. Taking account this fact and knowing that this kind of transport is suitable for shots with steeped temperature gradient, a good performance can be expected in #2562 shot.

It seems clear from figure 6.3 that the best results are obtained from W7X and W7-AS models. The W7X model has a GyroBohm-like dependence, $\chi_e \propto T_e^{3/2}$, however it has explicitly minor radius dependence too, thus it seems difficult to evaluate what kind of

transport physics can be expected of this model. Unlike the W7X model, the W7-AS results are quite remarkable, since in this case there is only one free parameter and there is no explicitly minor radius dependence. Particularly important seems to be the appearance of the rotational transform in the plasma center ι_0. The existence of this parameter in the transport model might explain the goodness of the results. This important fact will be clarified in the future.

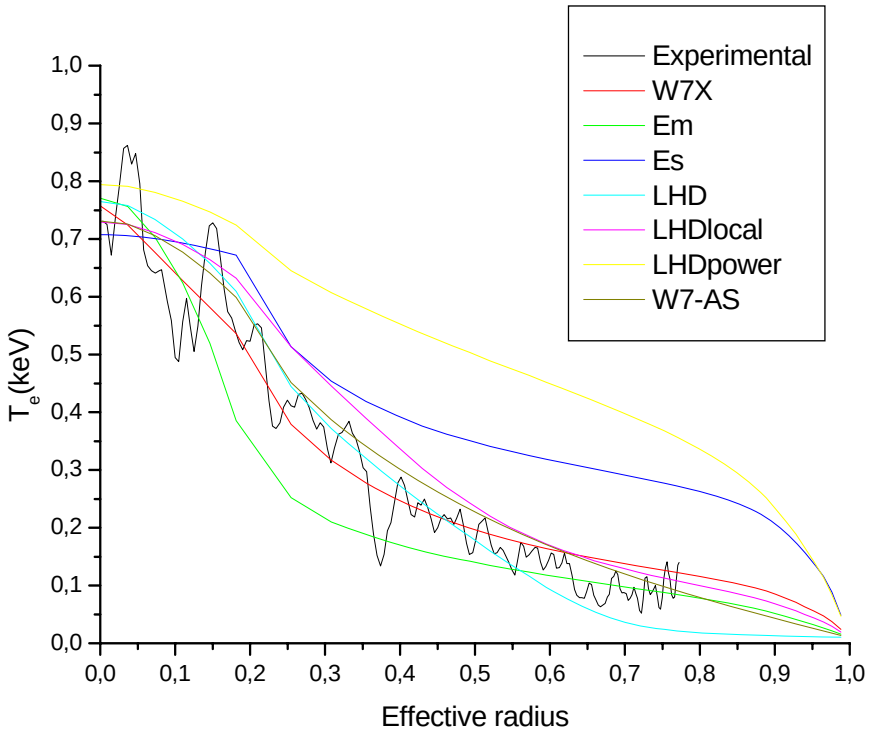

Figure 6.3 Experimental and simulated electron temperature obtained using the diffusion models in the case of shot #2559.

The simulations performed in the #2562 case are given in figure 6.4. In this kind of shot the temperature is worst simulated than in the "standard" one because this scenario is taken from an enhanced heat confinement profile, and the previous models were designed for standard profiles. Nevertheless, some of the models seem to have a good qualitative agreement, like in the W7X and the theoretical electromagnetic model case. The good agreement with the LHD model results from a modification in the model that manages to reduce the central electron thermal diffusivity. This modification is the following [Cas02]

$$\chi_e = \chi_{LHD}\left(1 - he^{-\left(\frac{\rho-\rho_b}{w}\right)^{\alpha}}\right) \tag{6.14}$$

where χ_{LHD} is the diffusivity from the LHD semi-empirical model, h takes account the transport reduction, ρ_b corresponds to the center of the transport reduction zone, w is the width of the transport reduction zone and α is a factor that takes account the shape of the transport reduction zone.

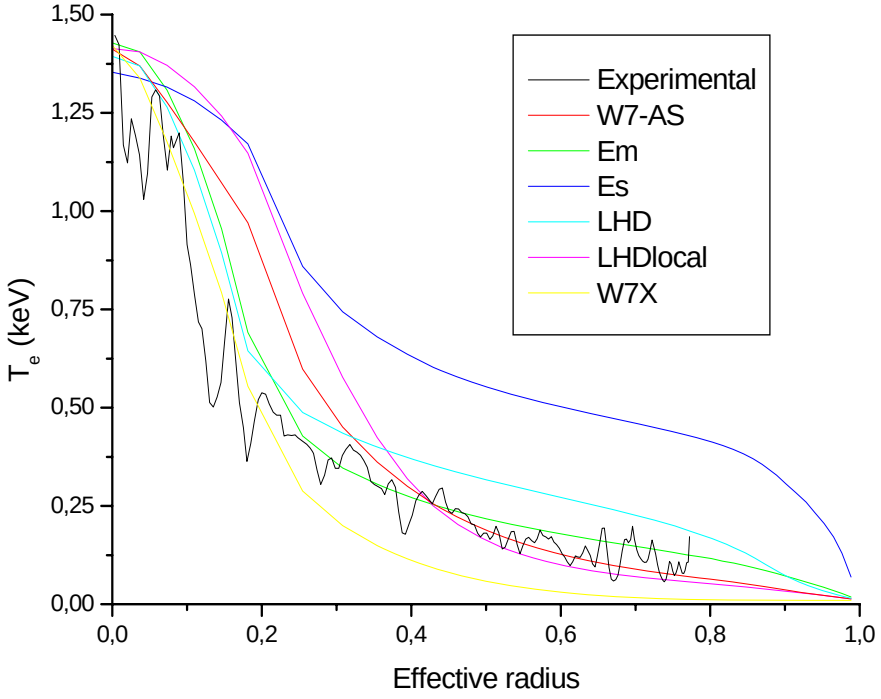

Figure 6.4 Experimental and simulated electron temperature obtained using the diffusion models in the case of shot #2562.

It is worth to point out that, in the same way than in the previous shot, the electromagnetic drift wave model tends to give a remarkable correct temperature profile, unlike the electrostatic drift wave model. Hence, as a new contribution of this thesis, this result might lead to the conclusion that in some way, electromagnetic processes are involved in the electron anomalous transport in the TJ-II.

6.5 Results analysis

The error in the simulated profile is measured as follows,

$$\sigma = \frac{\sqrt{\sum_i (T_i^{\exp} - T_i^{simul})^2}}{\sqrt{\sum_i (T_i^{\exp})^2}}$$

With this definition of error the results are given in table 2.

	Models						
Shot	**EM**	**ES**	**LHD**	**LHD local**	**LHD power**	**W7-AS**	**W7X**
#2559	28.1%	44.9%	18.2%	22.1%	76.7%	15.3%	17.3%
#2562	25.4%	87.7%	32.2%	57.2%	----	39.7%	19.2%

Table 6.2 Errors in the simulated temperature for each shot.

As can be seen from the table above, the best results are for the simulations of the #2559 shot for all the models. All of the models increase theirs errors by at least 15% more, except in the electromagnetic model in which there is no increasing but decreasing.

From the results obtained, it seems that the theoretical electromagnetic description is a good model in order to simulate plasmas in TJ-II because its error is similar to those of the best experimental models. Nevertheless, it is seen that the best model to simulate shots with no enhanced heat confinement is the W7-AS model, although more studies have to be done in order to check this conclusion.

	Models						
Shot	**EM**	**ES**	**LHD**	**LHD local**	**LHD power**	**W7-AS**	**W7X**
#2559	1.1 ms	1.9 ms	1.2 ms	1.5 ms	2.3 ms	1.4 ms	1.5 ms
Error	22.5%	33.8%	15.5%	5.6%	62%	1.4%	5.6%

Table 6.3 Simulated confinement time for the different models in the #2559 shot case.

	Models						
Shot	**EM**	**ES**	**LHD**	**LHD local**	**LHD power**	**W7-AS**	**W7X**
#2562	1.3 ms	2.5 ms	1.6 ms	1.3 ms		1.3 ms	1.3
Error	16.1%	61.3%	3.2%	16.1%		16.1%	16.1%

Table 6.4 Simulated confinement time for the different models in the #2562 shot case.

The goodness of the LHD model in shot #2562 is due to the correction implemented in the calculation of the thermal diffusivity. Although this correction the result is not better than the electromagnetic one, the best fitting model in this shot.

The confinement time obtained with each model and the error compared with the experimental one is shown in table 6.3 and 6.4. The results of the confinement time are similar among them for the models that match better the experimental electron temperature. Those that have a greater error in the experimental temperature results a higher confinement time since in these shots the temperature is overestimated along all the plasma radius and not only in the centre of the plasma.

The comparison between simulated radiated power and the experimental one are given in tables 6.5 and 6.6 in the #2559 and #2562 case respectively. In this case all the simulations give similar results, always smaller for the shots with higher errors in the temperature. LHD model is an exception, it gives the lesser radiated power in both shots. In the case of the #2559 shot this value is pretty bellow the others.

	Models						
Shot	**EM**	**ES**	**LHD**	**LHD local**	**LHD power**	**W7-AS**	**W7X**
#2559	83.8	82.9	77.4	85.2	80.5	84.7	83.8
Error	3.4%	2.3%	4.4%	5.2%	0.6%	4.6%	3.4%

Table 6.5 Radiated power (in kW) for the different models in the #2559 shot case.

	Models						
Shot	**EM**	**ES**	**LHD**	**LHD local**	**LHD power**	**W7-AS**	**W7X**
#2562	79.8	76.2	74.9	78.8		78.9	79.9
Error	3.6%	1.0%	2.7%	2.3%		2.5%	3.7%

Table 6.6 Radiated power (in kW) for the different models in the #2562 shot case.

The electron thermal diffusivities are shown in figure 6.5. As can be seen from the figure almost all the models have the same qualitative shape in both shots. The only exceptions are the LHD, due to the correction introduced, and the electrostatic model, that has a very different shape. Most of the models have a small value of the thermal diffusivity at the centre increasing at the edge.

Taking into account only the best fitting models, thus disregarding electrostatic and LHD power models, it can be seen that almost all of them have an almost flat value at the

centre. The only exceptions are the W7-AS and the electromagnetic models, which are always increasing, although this last model, an almost flat zone can be regarded in the middle zone. These models are the best fitting models in both shots. At the edge, all of them increase until ρ~0.9 and then decrease. The only exception is the LHD model that grows in the entire effective radius, resulting a too low temperature at the edge.

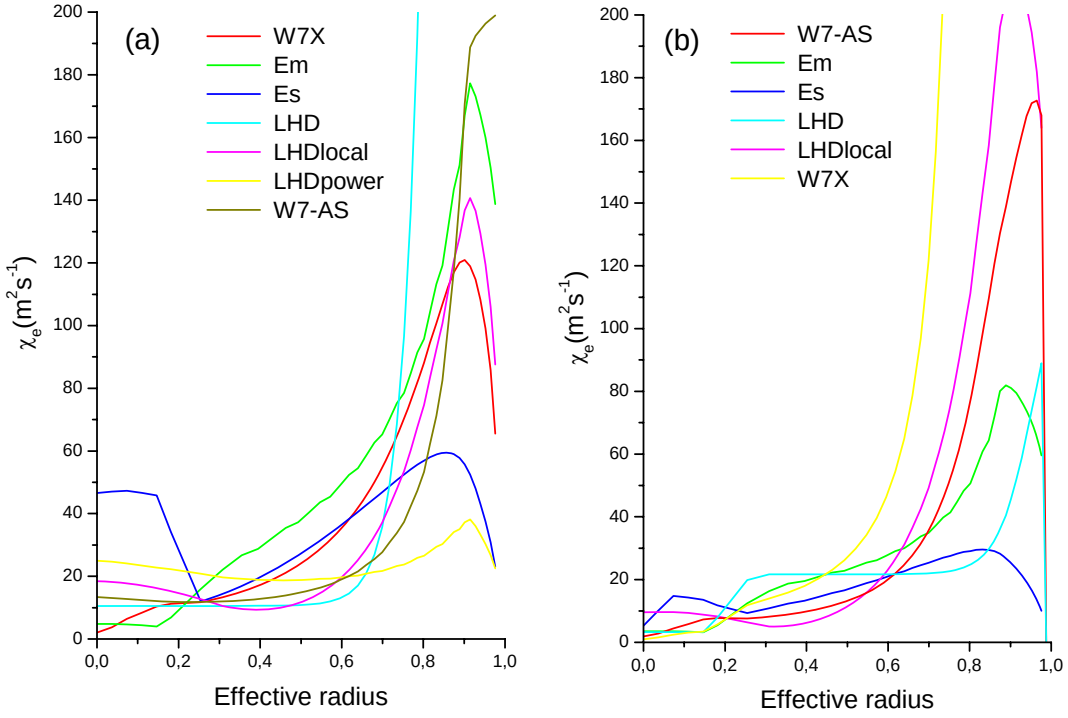

Figure 6.5 Electron thermal diffusivity for the different models, in the case of shot #2559 (a) and shot #2562 (b).

The comparison between the two shots results in a lower central thermal diffusivity in the shot #2562, as expected to have a higher value of the central temperature. The best fitting models have a similar shape in the shot #2562, a very low value at the centre, a flat profile region in the medium effective radius increasing to high values at the edge. The values of the thermal diffusivity are always smaller than values in the #2559 shot all along the plasma radius up to ρ~0.6. After that value the behaviour is different from model to model. An exception is the LHD case, because in the middle range has higher values in the enhanced heat confinement shot than in the "standard" one. This feature may be due to the modification introduced to simulate this kind of shots.

So, although the electromagnetic drift wave turbulence model was developed for tokamaks also fits well these discharges. In this model, the drift wave gives rise to $v_{||}\delta B/B$

diffusion, thus the model depends on the variation of the magnetic field. In a stellarator as TJ-II this variation could be the standard magnetic field of the device since, it is more complex than the magnetic field of a tokamak.

It is worth to point out that, as a new contribution of this thesis, the results obtained with the electromagnetic model are quite comparable with the results obtained with the LHD modified model used in this study as well as in other ones. Particularly important seems to be the diffusivity flat shape obtained by means of both models in the middle plasma and its similar central value. This result is quite important because this model has no modification throughout this study, and the errors obtained are reasonable in both standard and enhanced shot. However, although the errors obtained are reasonable, a more accurate simulation should be regarded as the final step towards a definitive thermal electron transport model for the TJ-II. This issue will be clarified in next chapter.

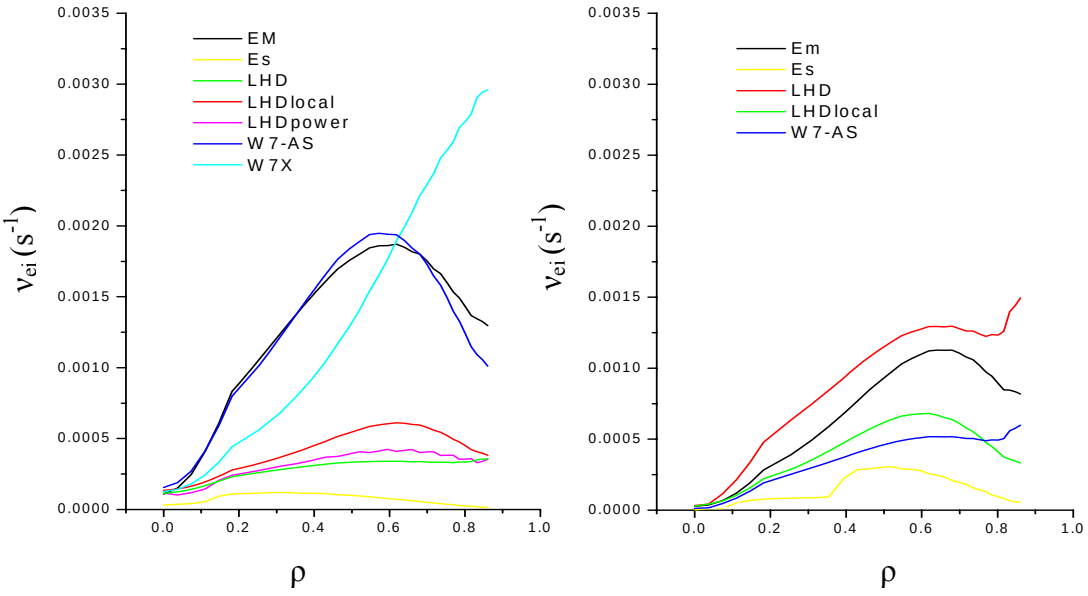

Figure 6.6 Electron-ion collisionalities for each model in the #2559 case (left) and the #2562 one (right).

Some similar study to the one presented in this thesis has been carried out using the shot #6998, which is very similar to the #2562 used here [Lop03], having both a low average density with hollow profile and steeped electron temperature profile. The results obtained using the ASTRA code seem similar to the ones obtained here. Particularly remarkable is the similarity of the thermal electron diffusivities obtained (which result to be almost always growing in the minor radius). As a new contribution of this thesis, it is also important to point that both studies (using different transport codes) share the

conclusion that in enhanced heat confinement scenarios, the LHD scaling is not applicable and that a electromagnetic drift wave-like model is necessary.

In order to compare the models not just using the temperature but with some more variable, a comparison of the collisionalities obtained with each model is showed in figure 6.6. In the #2559 case, the collisionalities obtained in the electromagnetic, W7-AS and LHD models are quite similar, whereas the rest of the models tend to have a slightly different collisionalty. In the #2562 case, the electromagnetic model and the LHD modified version have a similar profile whereas in this case, the collisionality obtained with W7-AS model tends to be a little bit different. These results confirm that, globally speaking, the drift wave electromagnetic physics seems to play an important role in the electron thermal transport in the TJ-II.

6.6 Conclusions

In this thesis some new electron heat transport models are added to PRETOR-Stellarator with the aim of performing a benchmark with experimental data from TJ-II. Two different types of discharges are simulated: a “standard” shot and one with enhanced heat confinement. Both discharges have the same plasma parameters with the exception of density profile.

As a new contribution of this thesis, it has been shown that the best model implemented in PRETOR-Stellarator to simulate discharges of TJ-II in the standard configuration is W7-AS model despite LHD pseudo-experimental is the most commonly model used to simulate heat transport in this device. It is worth to point out that with only one free parameter and no explicitly minor radius dependence the W7-AS model fits with accuracy the electron temperature. This model has an explicitly dependence on the rotational transform, and this factor may be an important parameter. In the future, in order to evaluate its importance, more studies with this model should be done by means of different shots with similar parameters and by changing the rotational transform in the center.

Although the theoretical electromagnetic model was derived for tokamaks, it fits reasonably well the experimental data in the case of “standard” shot and also agrees with the enhanced heat confinement shot. However no completely satisfactory behaviour has been obtained (mainly in the standard shot) due to the appearance of too high electron temperature gradients. Thus, a soft modulation should be obtained for this model between standard and enhanced heat confinement shots. Anyway, this model is a good candidate to

begin a study of anomalous transport in both situations, since electromagnetic drift waves seem to drive anomalous transport in the TJ-II. In this situation a possible explanation for the enhanced confinement scenarios is a reduction of the turbulence due to drift waves.

Future studies might be to compare other parameters of the plasma that would help to decide the best fitting model to simulate this device. Also some of the models could be modified in order to improve the simulation of the enhanced heat confinement regime.

Further analysis of the theoretical electromagnetic model should be done in order to clarify the factors that make this model fits with accuracy the enhanced heat confinement scenarios. Some of these issues will be clarified in the next chapter.

Chapter 7

Internal Transport Barrier analysis in LHD and TJ-II

7.1 Introduction

Low temperatures and low confinement is usually achieved in confined plasmas due to the high heat transport caused by turbulence. However, high electron temperature plasmas with peaked profiles have been obtained in the Large Helical Device (LHD) [Ida03] as well as in others stellarator devices, as the Compact Helical System (CHS) [Fuj99] and the TJ-II [Cas02]. These scenarios have been named electron Internal Transport Barrier (eITB) scenarios. These shots share the common characteristic of having a high positive electric field in the plasma core with a large shear. Both, electric field and its shear are supposed to suppress neoclassical transport and anomalous one respectively.

Different from tokamaks electron transport barrier scenarios (where magnetic field shear seems to play a significant role), transition between ion root (large neoclassical flux with small electric field (E_r)) to electron root (small neoclassical flux with a large positive E_r) in the plasma core seems to drive the transport barrier in stellarators [Ide93] when collisionality is low enough [Str01]. These facts are related strongly to the appearance of a density limit, below which, eITB is formed. Besides, the power deposition profile, as well as, ion temperature profile, seems to be important for the eITB formation.

In order to study the electron transport channel in LHD and TJ-II and to clarify the electron thermal diffusivity dependence with plasma parameters when a eITB is formed, some transport models have been added to TOTAL and PRETOR-Stellarator transport codes. These models can be divided into two categories: Bohm and GyroBohm-like models and drift wave models.

The Bohm and GyroBohm-like models used in this thesis are inspired from the Joint European Torus (JET) mixed-model [Tal01], shown later as equation 7.3. Generally speaking, the Bohm models establish that the electron heat diffusivity, χ_e, has the form $\chi_e \propto T_e$, and the GyroBohm $\chi_e \propto T_e^{3/2} / L$ where T_e is the electron temperature and L is the characteristic length of the reactor device. Physically speaking, the two models clearly distinguish the size of the convective cells formed by turbulence. The Bohm scaling arises from the mesoscale with characteristic length $\Delta x = (\rho_s L_T)^{1/2}$ where $\rho_s = (m_i T_e)^{1/2} / eB$ and $L_T^{-1} = \left|\nabla(lnT_e)\right|$. When the convective cell size reduces to scale as $\Delta x = \rho_s$ the GyroBohm scaling is applied.

These models have been empirically deduced to explain the electron temperature of tokamak plasmas in the turbulent mode, and have been broadly checked in the JET. Later, some improvements (as electron temperature gradient dependence) have been added in order to explain the enhanced confinement scenarios.

On the other hand, drift wave model can be divided into short (called electromagnetic drift waves) models (see equation 7.4 and 7.5) and long wavelength (called electrostatic drift waves) models. The long wavelength drift wave models arise from the fluctuations of the electric field of the plasma and the short ones arise from the fluctuations of the magnetic field. The characteristic length of the electrostatic waves, $\Delta x_{es} = q\rho_s \frac{R}{L_T}$ [Hor03], where q is the safety factor and R the major radius, is similar to the size of the convective cells of the GyroBohm scaling, and actually, both models are closely related leading to similar predictive results. Contrary to the long pattern of the electrostatic drift waves, the short wavelength have lead to coherent structures of the collisionless skin depth $\Delta x_{em} = c / \omega_{pe}$, where c is the light speed and $\omega_{pe} = \sqrt{n_e e^2 / \varepsilon_0 m_e}$ is the plasma frequency. In a typical tokamak, this length is of order of a few millimeters and is much smaller than long wave that is on the scale of several centimeters [Hor03]. Studies of electron transport in the spectrum range of the electromagnetic waves show the stochastization of the guiding center orbits and the fast propagation of the electron heat flux with small correlation time [Kim90].

Analyzing the mixing lengths Δx_{es} and Δx_{em} one can find that both type of transport can exits in the plasma. The condition $\Delta x_{es} = \Delta x_{em}$ leads to the expression for the plasma beta $\beta_{crit} = L_T^2 / q^2 R^2$ at the transition between the two regimes. Therefore, in a plasma with eITB, where the electron temperature is very high in the plasma core and the electron density profile is almost flat, the β_{pe} may be higher than β_{crit} at the plasma core and lower outside that region. In order to study whether these tokamak ideas may be applied to stellarators a sketch of mixed short and long wavelength models has been derived for this study (Eq. 7.6) as a good candidate for the reduction of the turbulence to the eITB levels.

The effect of anomalous transport reduction by the electric field shear has been introduced by means of the factor $\frac{1}{\left(1+(\tau f_{ExB})^{\gamma}\right)}$ as described in equation 7.7. This factor takes account of the $E \times B$ flux and has been previously checked as a good candidate to suppress anomalous transport in tokamak plasmas [Jac00], as well as, also derived from theoretical models [Fig03] [Ito96].

The aim of this study is, to search for best models that reproduce a LHD and TJ-II eITB shots, and show their dependence with electron density, in order to obtain the critical behaviour previously described. By using these best fitted transport models, we might easily extrapolate the present data to the future reactor plasmas design.

This study is divided into two parts: the first one containing the eITB studies corresponding to the LHD stellarator and another one to the TJ-II stellarator.

7.2 LHD study

7.2.1 Introduction

In order to study the electron transport channel and to clarify the electron thermal diffusivity dependence with plasma parameters, some transport models have been added to TOTAL [Yam92] code. These models can be divided into two categories: Bohm and GyroBohm-like models and drift wave models.

7.2.2 Experimental set-up

The shot analyzed (#26943) corresponds to the fifth campaign of the LHD experiment, the high peaked electron temperature profile has been obtained by using 1 MW of Electron Cyclotron Heating (ECH) heating power [Fuj99]. Figure 7.1 shows the electron temperature and density profile measured by 200-channel YAG Tohmsom scattering system [Yam02] and 11-channel FIR interferometer [Nar01]. The density profile was obtained by Abel inversion method with 3-dimensioanl self-consistent equilibrium calculated by using extended radial magnetic coordinates to treat with ergodic regions in the PRE-TOTAL code.

Only central value of ion temperature is measured to be 2.0 keV by the crystal spectrometer technique, and the parabolic profile of ion temperature was assumed for equilibrium reconstruction. The central deposition profile of ECH ray-tracing analysis critically depends on the magnetic axis position and plasma equilibrium, and it is difficult to determine the deposition profile at $\rho < 0.1$. Therefore, the following profile with the width of $\rho_{wid} = 0.15$ is adopted:

$$P_{ECH} \propto \exp\left[-\left(\rho / \rho_{wid}\right)^4\right] \tag{1}$$

which agrees well with the results of the ray-tracing analysis at $\rho \geq 0.1$.

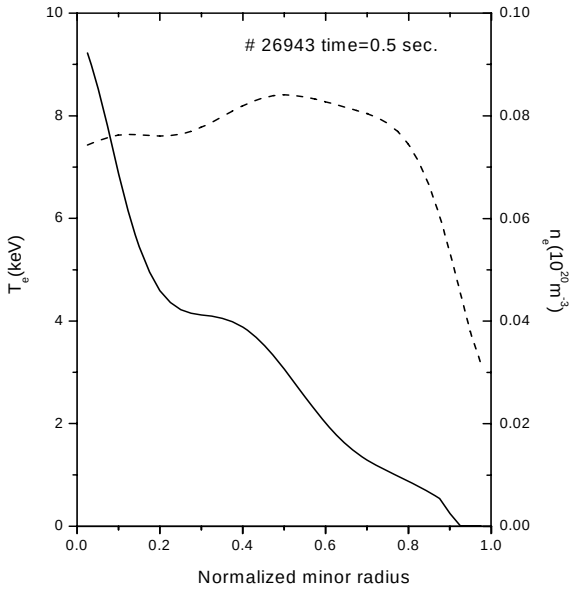

Figure 7.1 Experimental electron temperature and density profiles obtained in LHD.

7.2.3 Model equations for neoclassical transport

The neoclassical transport model used in this study has been previously described in chapter three.

7.2.4 Anomalous transport models

The following list contains the models used throughout this study:

7.2.4.1 GyroBohm-like model

$$\chi_e = \alpha_e^{gB}\chi_{gB},\ \chi_{gB} = (cT_e/eB)(\rho_i/L_{Te}),\ L_{Te} = \left|\frac{\nabla T_e}{T_e}\right|^{-1} \tag{7.1}$$

7.2.4.2 Bohm-like model

$$\chi_e = \alpha_e^{B}\chi_B,\ \chi_B = (cT_e/eB)(q^2 a/L_{Pe})\langle L_{Te}\rangle^{-1}, L_{Pe} = \left|\frac{\nabla p_e}{p_e}\right|^{-1},$$
$$\langle L_{Te}\rangle^{-1} = \left|(T_e(\rho=0.8) - T_e(\rho=1))/T_e(\rho=1)\right| \tag{7.2}$$

7.2.4.3 Mixed Bohm-GyroBohm

$$\chi_e = \alpha_e^{gB}\chi_{gB} + \alpha_e^{B}\chi_B,\ \chi_{gB} = (cT_e/eB)(\rho_i/L_{Te}),$$
$$\chi_B = (cT_e/eB)(q^2 a/L_{Pe})\langle L_{Te}\rangle^{-1}, L_{Pe} = \left|\frac{\nabla P_e}{P_e}\right|^{-1}, L_{Te} = \left|\frac{\nabla T_e}{T_e}\right|^{-1}, \tag{7.3}$$
$$\langle L_{Te}\rangle^{-1} = \left|(T_e(\rho=0.8) - T_e(\rho=1))/T_e(\rho=1)\right|$$

7.2.4.4 Short wavelength version 1 (Sw1)

$$\chi_e = C_1 \varepsilon_t^{1/2} \frac{v_t}{R}\frac{c^2}{\omega_{pe}^2} \tag{7.4}$$

7.2.4.5 Short wavelength version 2 (Sw2)

$$\chi_e = C_1 \frac{v_t}{(L_{Te}R)^{1/2}}\frac{c^2}{\omega_{pe}^2} \tag{7.5}$$

7.2.4.6 6-Regimes drift wave [Yam92]

7.2.4.7 Mixed short wavelength-long wavelength model

$$\chi_e = C_1 \varepsilon_t^{1/2} \frac{v_t}{R} \frac{c^2}{\omega_{pe}^2} H(\beta_{crit}) + (1 - H(\beta_{crit})) C_2 (cT_e / eB)(\rho_i / L_{Te}) \tag{7.6}$$

where θ is the Heaviside function.

7.2.4.8 Anomalous transport suppression factor

$$\chi_{e,shear} = \frac{\chi_e}{1 + (\tau f_{ExB})^{\gamma}} \tag{7.7}$$

where $f_{ExB} = \partial_r (E_r / B_\theta)$ with E_r the plasma radial electric field and B_θ the poloidal magnetic field. The following values, τ=5.5 × 10^{-4}s and γ=1.5, have been used throughout this study. The constant τ can be seen regarded as the correlation time for the fluctuations without $E \times B$ flow.

7.2.5 Simulation results

7.2.5.1 Drift wave models

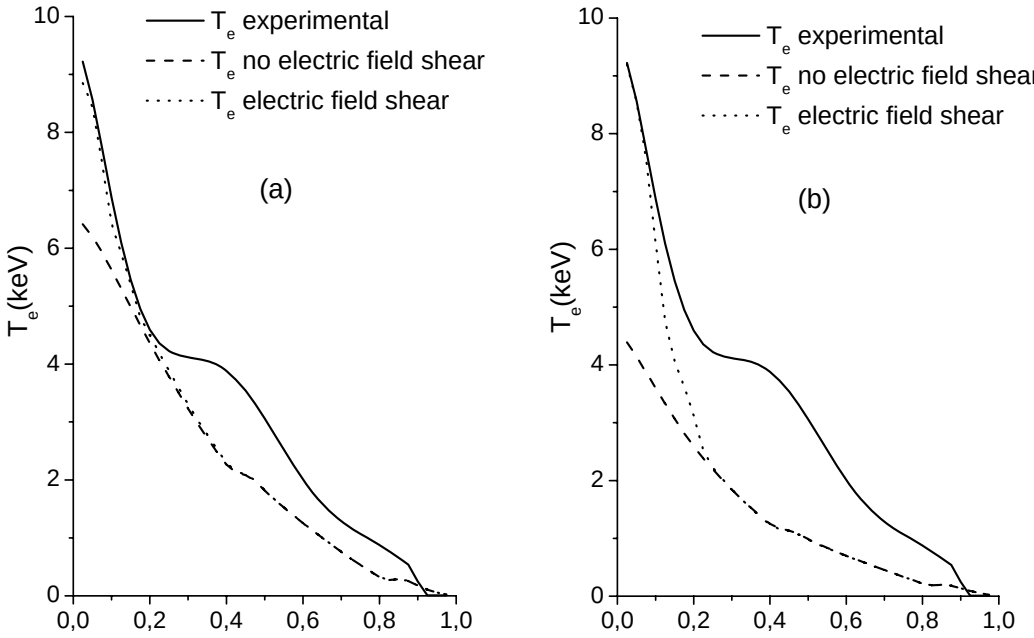

Figure 7.2 Electron temperature profiles obtained with short wavelength sw2 model (a), short wavelength model sw1 (b) and experimental electron temperature profile, with and without electric field shear effect.

In figure 7.2 and figure 7.3 the electron temperature profiles for the models Sw1, Sw2 and 6-regime drift wave with and without electric field shear effect are compared with the experimental electron temperature. From the figures, one can see that short wavelength models (in particular sw2) can reproduce the temperature profile in the plasma core in the range $0 \le \rho < 0.2$.

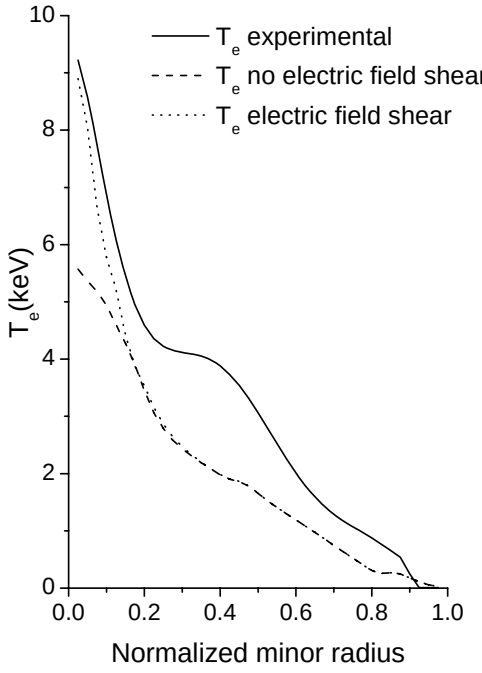

Figure 7.3 Electron temperature profiles obtained with 6-regimes drift wave model and experimental electron temperature profile, with and without electric field shear effect.

However, outside this range, the plasma profiles are completely wrong, with temperatures quite different from the experimental ones. In this situation, one can think about the existence of a transition between one kind of transport in the plasma core and another type outside this zone. This point will be clarified along this study.

Related to the electric field shear effect, the electron temperature profiles become peaked (a high electron temperature gradient appears at the plasma core) and higher central electron temperature are obtained by means of the introduction of this effect in the calculation, while the rest of the plasma profile is very similar in both situations.

7.2.5.2 Bohm and Gyro-Bohm like models

In figure 7.4 and figure 7.5 the electron temperature profiles for three models Bohm, GyroBohm and mixed model with and without electric field shear effect are compared with the experimental electron temperature. First of all, one can see from the figures that all the three models lead to similar results. This is due mainly to the fact that in this scenario (with almost flat density profile) the values of the factors L_{Te} (from the GyroBohm model) and L_{Pe} (from the Bohm model) are very similar, however GyroBohm model tends to give a flater profile outside the core plasma.

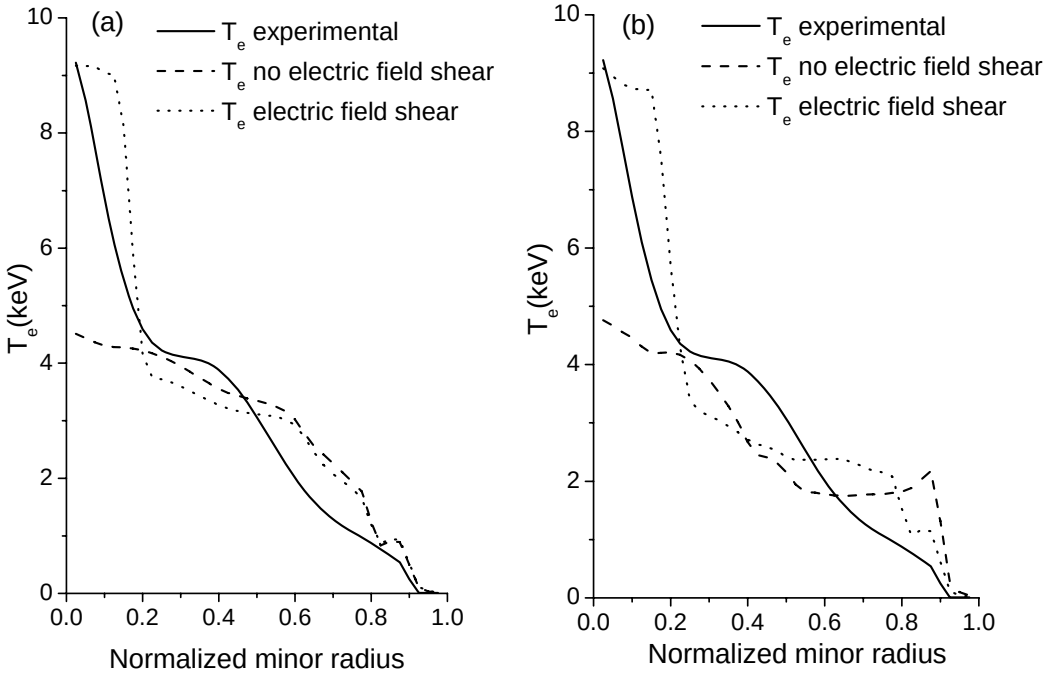

Figure 7.4 Electron temperature profiles obtained with Bohm-like model (a), GyroBohm-like model (b) and experimental electron temperature profile, with and without electric field shear effect.

The central temperature profile obtained with these models has a more parabolic shape compared to the drift wave models and the temperature gradient in the region $0 \le \rho < 0.1$ is much smaller. However a high gradient (comparable to the ones obtained in the drift wave profiles) is obtained in the region $0.1 \le \rho < 0.2$. These values of the temperature are compatible with the experimental values and always fit within the error bars.

The main difference between these models and the ones studied in the previous section is that outside the plasma core (where the influence of the electric field shear is negligible) models reproduce the experimental profiles with reasonably accuracy. Moreover, the transition point (between a region with high temperature gradient and a small one) observed in the experimental profile at $\rho \approx 0.2$ is well simulated.

Clearly, one can see that the influence of the electric field shear on the profiles is stronger in this case than in the drift wave scenarios. This is due to the fact that the electric field obtained has a higher shear in this case and its effect over a quite flat temperature profile is stronger than in the case of drift wave, where the electron temperature gradient is always high at the plasma core even without electric field shear.

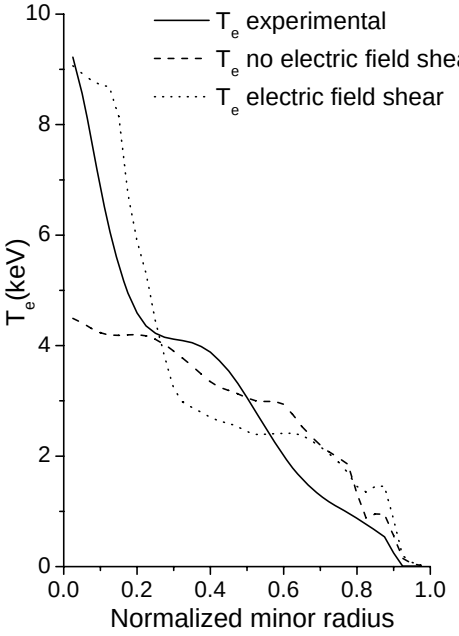

Figure 7.5 Electron temperature profiles obtained with Mixed Bohm-GyroBohm, model and experimental electron temperature profile, with and without electric field shear effect.

7.2.5.3 Mixed drift wave models

It has been shown in section 7.1 that a model based in short wave length can simulate the eITB LHD shot #26943 in the region $0 \le \rho < 0.2$, however it seems more adequate a long wavelength based model to simulate the plasma electron temperature outside this region. With the aim of having a global transport model, a combination of short

wavelength a long wavelength drift model has been derived in this thesis (equation 7.6). The transition between both regimes depends of the parameter $\beta_{crit}(\rho)$. As a first step using this model, this value has been imposed to get the transition point at $\rho = 0.2$. In next sections, it will be calculated using the condition that the characteristic length of both models is same.

From figure 7.6, one can see that the simulated profile has a steep gradient in the plasma core and a more flat shape at the edge. The high peaked gradient is due to two effects coupled: one fact that the high sheared electric field obtained using this model reduces electron anomalous heat transport and the fact that the short wavelength model is an Electron Temperature Gradient (ETG) like model and this type of thermal flux enhances the appearance of high electron temperature gradients along the plasma due to the existence of short coherent structures.

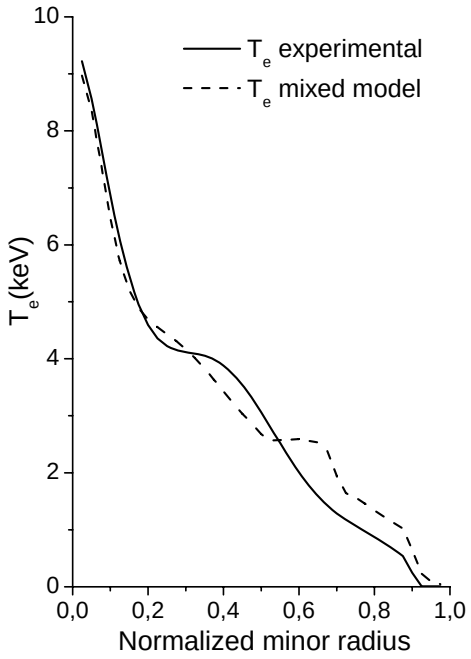

Figure 7.6 Electron temperature profile obtained with mixed short wavelength-long wavelength model, and experimental electron temperature profile.

However, in this case, such high gradients are limited by the transport model because of their limitation to the range $0 \le \rho < 0.2$. Outside this region, the gradients are softer, and as a new contribution of this thesis, the simulated profile fits reasonably well the experimental one.

7.2.6 Density study

The eITB formation in plasmas is strongly linked with the average density. In the LHD plasmas, it has been experimentally shown that exits a critical density below which (and if the power deposition is centred enough) the eITB is formed. In order to study the validity of the previous transport models, not just for one shot with eITB, but for a wide range of plasma parameters, with the aim of reproducing the critical transition between a non-eITB scenario and an eITB one, some simulations have been carried out with the same electron density profile than in the previous section but with different average densities.

The electron density profiles are given in figure 7.7 (left) and the average density of each profile in table 7.1.

Density profile	Average density (x 10^{20} m^{-3})
1	0.07
2	0.09
3	0.11
4	0.22
5	0.32
6	0.52

Table 7.1 Average electron densities used in the density study.

The first model applied is the mixed short wavelength long wavelength model. As a first step and in order to see the importance of the factor β_{crit}, it has been kept fixed along the simulations, and its value is the same one used for the experimental eITB shot. This corresponds to the situation which has the transition point between the two regimes at $\rho = 0.2$. The results are given in figure 7.7 (right) and, as can be seen, although the eITB shot is well simulated, there is no clear transition between eITB and non-eITB scenarios because of the lack of a critical transition between high peaked temperature profiles with high electron temperature gradients and temperatures profiles with small gradients.

It is worth to point out that in the high densities scenarios, which have small negative electric field values at the plasma core (and consequently there is no clear anomalous transport suppression), while high temperature gradients are obtained in the range $0 \le \rho < 0.6$. This situation confirms the results about short wavelength model obtained in

the previous section, which showed that this model tends to make the electron temperature profiles to have relatively high gradients even with no electric field shear suppression.

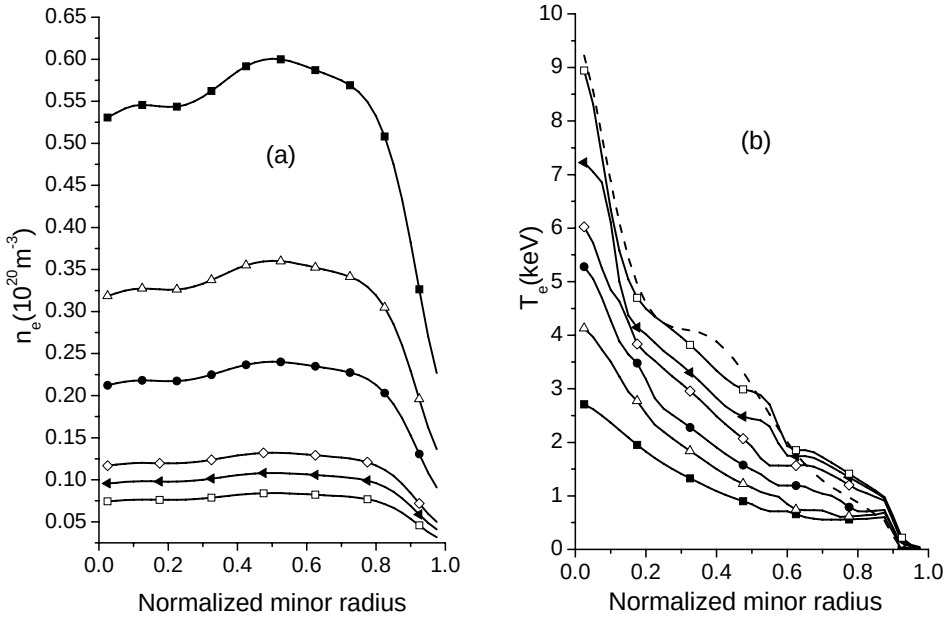

Figure 7.7 Density profiles used along the simulations (a). Electron temperature profiles (b) obtained with the short-long drift wave model and fixed β_{crit} (the same one than the one used in shot #26943).

In order to avoid this behaviour, the transition point β_{crit} has been calculated imposing the condition that the characteristic lengths of both type of transport are similar. This condition leads to expression $\beta_{crit} = L_T^2 / q^2 R^2$ for the critical beta. The electron temperature profiles obtained, using this value in equation 7.6, are shown in figure 7.8 (left).

In this case, a clear transition between some scenarios with eITB and some other ones without eITB is obtained. The critical transition is obtained for an average density $< n_e > \approx 0.2 x 10^{20} m^{-3}$. In order to analyze the central electron temperature dependence on the average density, both variables have been plotted in figure 7.8 (left) as well as in figure 7.9 (left). There are two regimes quite different. The first one, corresponding to eITB scenarios, has temperature dependence $T_e(0) \propto < n_e >^{-0.57}$, whereas in non-eITB scenarios, this dependence is $T_e(0) \propto < n_e >^{-0.39}$. Clearly, the temperature dependence of density in eITB cases is stronger.

Comparing these results with experimental data [Ida03], and as a new contribution of this thesis, one can conclude that this model, with this experimental set-up, can simulate the plasma behaviour with reasonable accuracy.

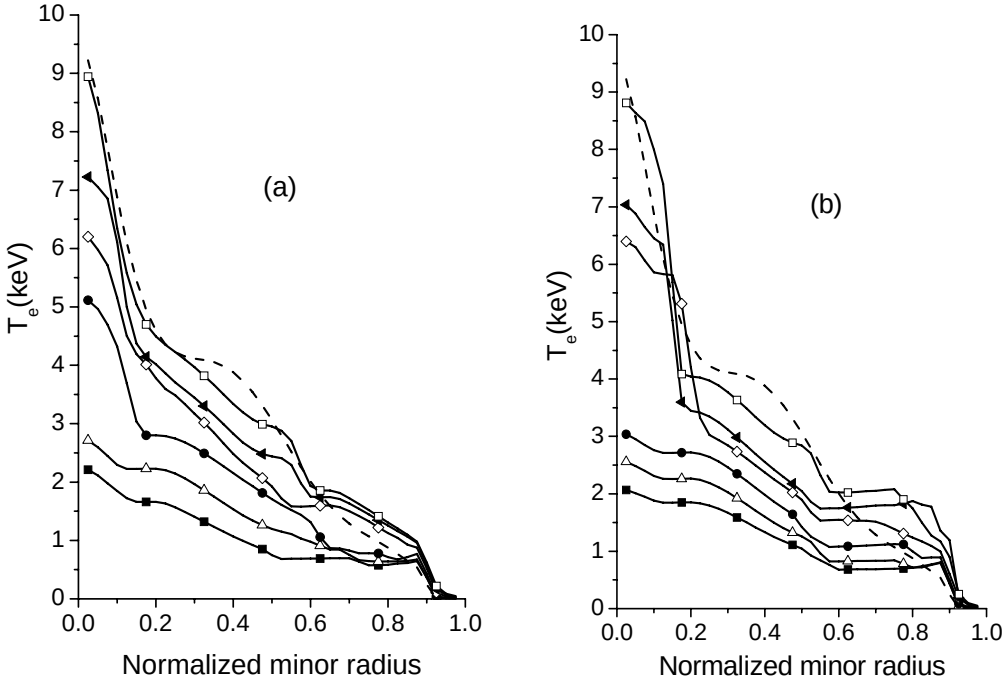

Figure 7.8 Electron temperature profiles obtained with the mixed short-long drift wave model (a) and variable β_{crit}. Electron temperature profiles obtained with the GyroBohm-like model (b).

Finally, a complete GyroBohm-like scaling (equation 7.1) has been applied to analyze its dependence with density. In this case a similar behaviour is obtained, although the central temperature profiles seem to be more "parabolic". The critical density is now lower, $< n_e > \approx 0.1x10^{20} m^{-3}$, than the previously one obtained. Analyzing the central temperature dependence, $T_e(0) \propto < n_e >^{-0.72}$ in the eITB case and $T_e(0) \propto < n_e >^{-0.42}$ in the non-eITB one, it is deduced that, outside the core regions, both transport models lead to similar results, but in the plasma core, the dependence of the GyroBohm-like model is much stronger. This fact makes the critical transition to be steeper and clearer but not similar to the experimental evidence. Anyway, this dependence should be clarified with more experimental results to decide what type of transport is dominant at the plasma core in the case of eITB shots.

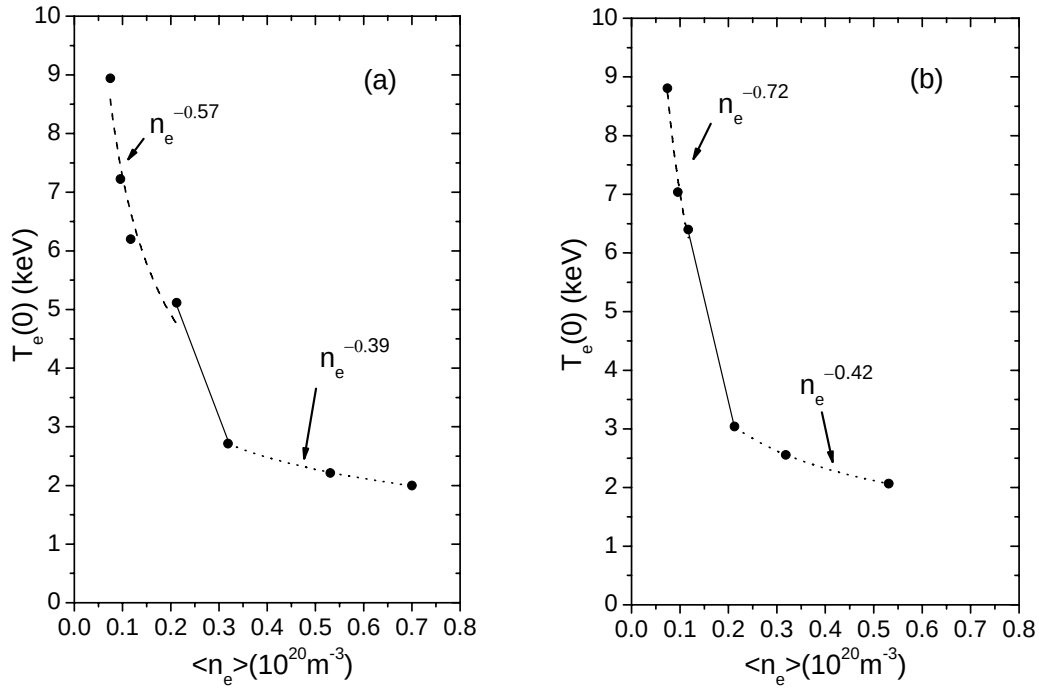

Figure 7.9 Central electron temperature dependence with density obtained with the short-long drift wave model (a). Central electron temperature dependence with density obtained for the GyroBohm-like model (b).

7.2.7 Analysis of the electric field and electron thermal diffusivity

In order to analyze the previous results, not just comparing the experimental temperature profile, but some more variables, a comparison of the electric field and the electron thermal diffusivity has been carrying out for the LHD shot #26943. The electric field is calculated using the ambipolar condition, $\Gamma_e^{na} = \sum_k z_k \Gamma_k^{na}$, where Γ_e^{an} is the asymmetric part of the neoclassical electron flux, Γ_k^{an} and z_k are the asymmetric neoclassical ion flux and the ion charge for each species k respectively.

Electric field and thermal diffusivities profiles for the mixed drift wave case are given in figure 7.10, and for the GyroBohm-like model in figure 7.11. The electric field for both simulations is quite similar, with a high central value $E_r \approx 750$ V/cm and high electric field shear $\left|dE_r / dr\right| \approx 125$ V/cm^2. In the outer part of the plasma, the electric field tends to be small with either positive or negative values and very small electric field shear.

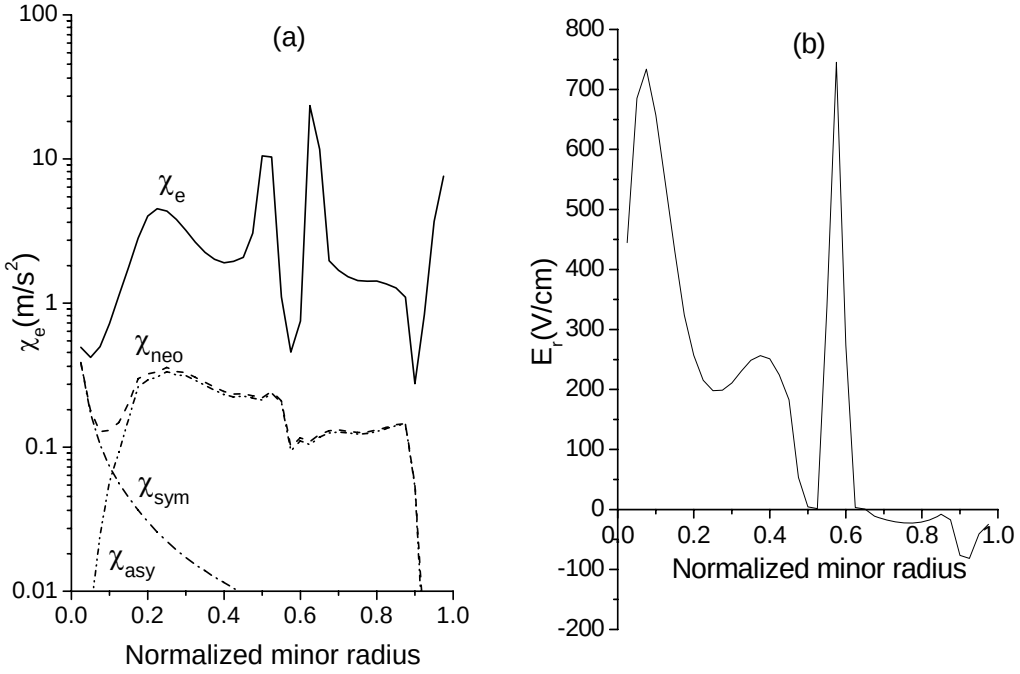

Figure 7.10 Electron thermal diffusivity χ_e obtained with the mixed model, asymmetric neoclassical diffusivity χ_{asy}, symmetric neoclassical diffusivity χ_{sym} and total neoclassical diffusivity χ_{neo} (a). Electric field obtained with this model (b).

Comparing these results with the analysis of the fixed experimental profiles of the shot #26943 [Yam02], we can conclude that the results fits reasonably well with the experimental studies.

As for the thermal diffusivities, differences between both models are more significant. Comparing the results of the figures 7.10 and 7.11, one can see that for both simulations the electron thermal diffusivity is small in the region $0 \le \rho < 0.1$, and grows up to $\chi_e \approx 6$ m/s^2 in the drift wave case and up to $\chi_e \approx 10$ m/s^2 in the GyroBohm-like case in the region $0.1 \le \rho < 0.2$. After that, it drops again in the range to $0.2 \le \rho < 0.4$. This behaviour is the one expected from an eITB scenario [Ida03]. However, although in both cases the electron thermal diffusivity is higher than the neoclassical one, in the case of drift wave simulation, both type of transport seem to be comparable in the region $0 \le \rho < 0.1$, whereas for the GyroBohm-like simulation they are not. This feature is closely related to the shape of the electron temperature at the plasma core. In the drift wave case it is very peaked with a high temperature gradient in the whole range $0 \le \rho < 0.2$, while in the GyroBohm-like case the shape is parabolic.

The issue of solving what type of transport is dominant in the plasma core cannot be answered at this point because of the error bars of the experimental temperature profile. However from the dependence of the central temperature with the average density, it seems that the drift wave simulation is closer to the experimental data. Therefore, the electric field shear seems to affect the heat transport by short drift waves in a manner that reduces its value close to neoclassical levels. In order to compare whether this conclusion may applied to other stellarators this result will be studied again in the TJ-II case in following sections.

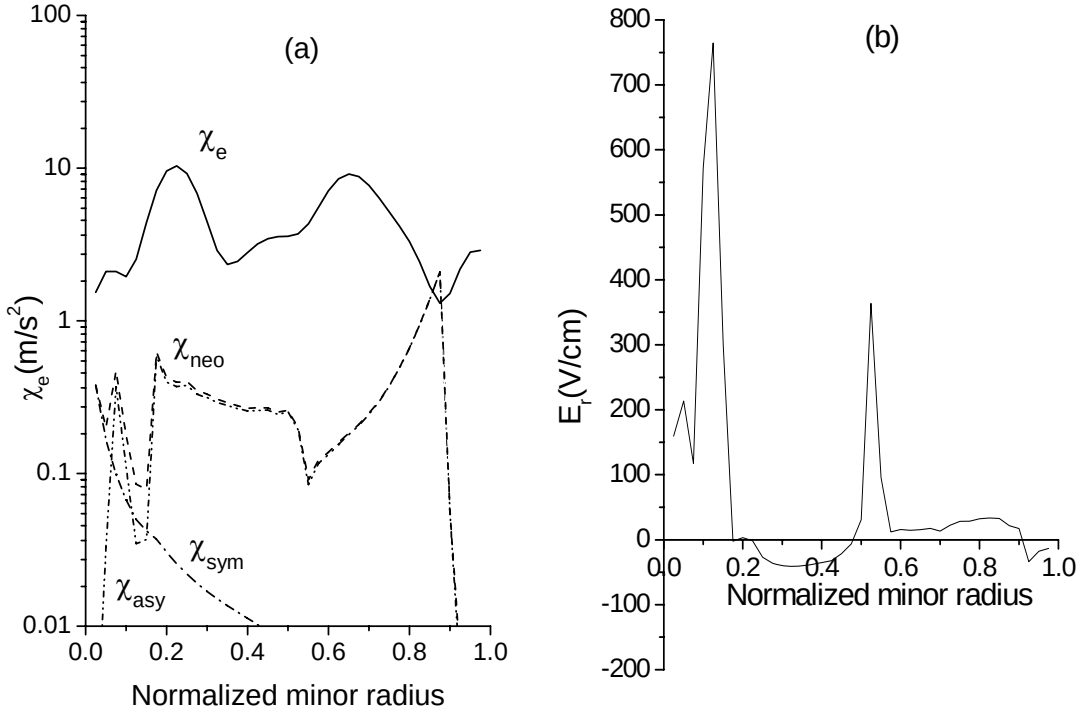

Figure 7.11 Electron thermal diffusivity χ_e obtained with the GyroBohm-like model, asymmetric neoclassical diffusivity χ_{asy}, symmetric neoclassical diffusivity χ_{sym} and total neoclassical diffusivity χ_{neo} (a). Electric field obtained with this model (b).

7.3 TJ-II study

7.3.1 Introduction

TJ-II [Ale90] is a medium size four periods stellarator (heliac type, B≤1.2T; R=1.5 m; <a> ≤ 0.2 m) with a wide rotational range 0.9≤ ι(0)/2π≤2.2 in low, negative shear configurations (Δq/q< -6%). The TJ-II plasmas are produced and heated with Electron

Cyclotron Resonance Heating (ECRH), two gyrotrons of 300 kW each at 53.2 GHz, 2nd harmonic, X-mode polarization.

Typical central electron temperature values in TJ-II are about 0.8-1.2 keV with 600kW ECRH injected power. However in low-density scenarios with high ECRH absorbed power density in plasma center, 1.5-2 keV central electron temperature is reached. Total plasma energy is increased, but not as expected since the peaked temperature is localized in a narrow region in plasma centre. These scenarios, with the same density and ECRH heating conditions, have been observed in Compact Helical System (CHS), Wendelstein7-AS (W7-AS) and the LHD, as previously analyzed in this study. It is known from several studies and from the previous section of this thesis, that a sheared electric field is the key element for the reduction of anomalous transport [Boe02] [Gar06]. In this situation, a common process should explain the reduction in heat transport in plasma centre. Theoretical and experimental studies have been done in W7-AS on electron heat transport reduction triggered by neoclassical transport. For this purpose, a complete study of electric field is necessary in order to understand the eITB formation and the heat transport reduction. It is well known that the generation of this electric field in helical systems is due to neoclassical transport, and that an electric field shear is the key process in order to reduce anomalous transport.

In order to analyse a possible common source for the turbulence and its suppression in the TJ-II and LHD, the transport model from equation 7.4 (short wavelength) has been added to PRETOR-Stellarator code. This code has been widely applied to study the TJ-II and it seems suitable to make this study. The turbulence suppression by the electric field shear has been also added by means of the factor from equation 7.7.

7.3.2 Experimental data

The data is collected from TJ-II stellarator. The magnetic configuration used is the 100_40_63. In this case two discharges from a density scan are selected. The first one, #2559, is a “standard” one whereas the other one, #2562, is an enhanced heat confinement shot. The data used is the electron temperature and density measured by a multi-point Thompson scattering. The data is plotted in the figure 7.12.

As can be seen from figure 7.12 the electron temperature is higher in shot #2562 with a high temperature gradient at $\rho \approx 0.15$, for effective radius greater than 0.15 both temperatures being quite similar. The electron temperature gradient of shot #2559 is roughly constant throughout the entire plasma radius. The density is flat (or even hollow)

in the centre of the plasma radius for #2562 shot. This feature is characteristic in all the enhanced heat confinement shots in TJ-II. In fact, low densities with hollow profiles are the key point for eITB scenarios. A possible explanation to this kind of behaviour will be explained along this paper. The density ρ>0.5 has similar values in both shots whereas in shot #2562 it is lower for the inner radius.

The plasma composed by hydrogen is heated with 300 kW of ECR heating provided by one gyrotron and transmitted to the plasma by a quasi-optic transmission line.

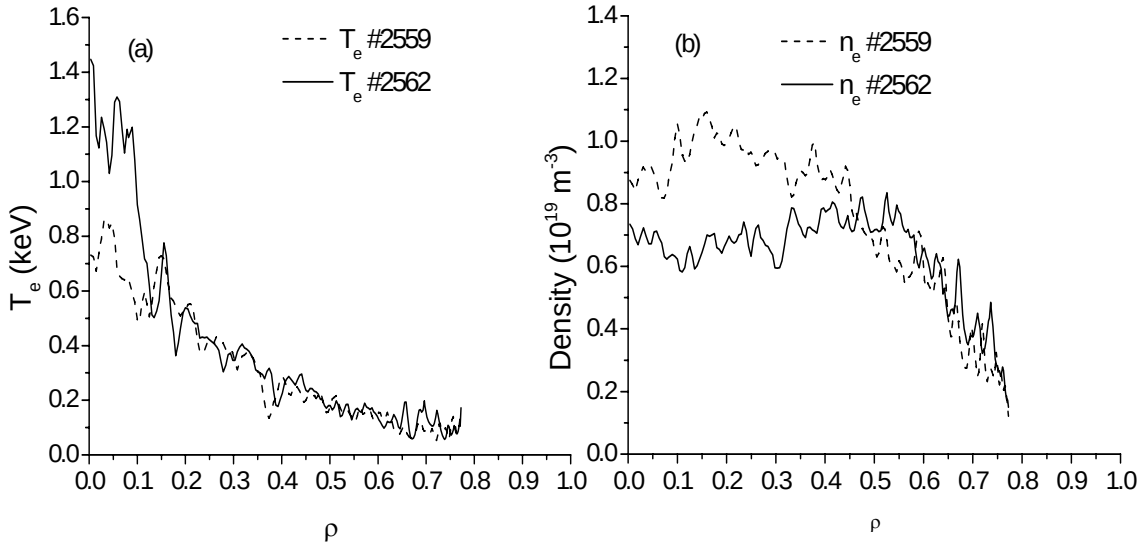

Figure 7.12 Electron temperature and density profiles collected from Thompson scattering in shots #2559 and #2562.

7.3.3 Model equations for neoclassical transport

The equations used for the neoclassical transport as well as the global transport equations are the same used previously for the LHD study. However, in this case, the power deposition has been modelled as ($\rho_{wid} = 0.2$),

$$P_{ECH} \propto \exp(-(\rho / \rho_{wid})^2) .$$

which is a good fit for the experimental data [Egu03].

7.3.4 Anomalous transport model

Previously to this study for the TJ-II, a complete analysis of the goodness of diverse transport models has been carried out in the previous chapter using PRETOR-Stellarator [Die04]. Some conclusions of that work were that electromagnetic drift waves had reasonably results with both non-eITB and eITB shots, although there were better models. Taking account the fact that, the electric field obtained using PRETOR-Stellarator has been compared with another more sophisticated techniques, and the results have been satisfactory [Gar04], now, we have the possibility of the inclusion of the turbulence suppression by the effect of electric field shear. On the other hand, electromagnetic drift wave models have been used successfully with tokamak devices, and have simulated also ECRH plasmas in LHD, as described previously in this study.

So, as a first step to make a comparison between the two devices, the model from equation 7.4, and the factor form equation 7.7 have been added to PRETOR-Stellarator to study the transition between non-eITB and eITB shots. This model is quite similar to the current diffusive ballooning mode, although in this case no magnetic shear dependence factor has been added because TJ-II is an almost shearless device. In this case, the constant for the correlation time of the fluctuations has been changed after a sensitivity study. The new result for the TJ-II is $\tau = 5.5 \times 10^{-4}$s.

The ion temperature profile is simulated with the Hinton-Hazeltine [Hin76] model with Chang-Hinton [Cha82] correction. This model shows good agreement with most experimental TJ-II data. The equilibrium ion temperature is 0.12 keV at the center and 0.05 keV at the edge with a parabolic profile. In this situation temperature gradient is very small, corresponding to an almost flat profile.

7.3.5 Transport analysis

Using PRETOR-Stellarator a transport study has been done. The electron density is fixed during simulation to fit experimental profile because enhanced heat confinement shots are very sensitive to density fluctuations. The results of temperature simulation compared with experimental data are show in figure 7.13 (a) for #2562 shot and in figure 7.13 (b) for #2559 shot. The neoclassical electric field structure for both shots is shown in figure 7.14 and the neoclassical asymmetric electron and ion fluxes at $\rho = 0.25$ for #2562 shot are shown in figure 7.15. As can be seen from the graphics, experimental temperatures are simulated with reasonable accuracy by this transport model. The electric field is

calculated using the ambipolar condition, as calculated in section 7. The composition of the TJ-II plasmas in these shots is hydrogen and we have included 1% of carbon concentration as an impurity.

The neoclassical electric field has a high value, $E_r \approx 130V/cm$ in the plasma core in the case of shot #2562 and a small one, $E_r \approx 40V/cm$, for the standard shot #2559. In both shots it has a transition between electron and ion root around $\rho \approx 0.5$. The measured radial electric field in plasmas which present eITB is in the range of 100-150 V/cm, and without eITB is in the range 40-50 V/cm, hence, as a new contribution of this thesis, the results obtained by using the electromagnetic model together with the anomalous transport suppression by electric field shear show good agreement with experimental ones [Cas04].

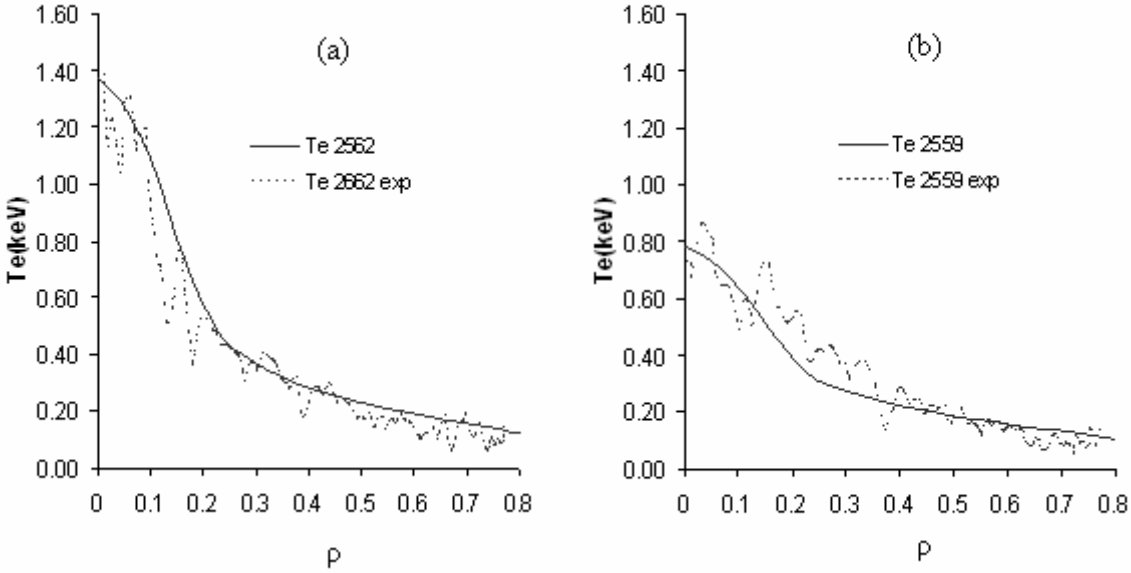

Figure 7.13 Comparison between electron temperature profiles simulations of shots #2562 (a) and #2559 (b) made with the model previously described and experimental profiles.

It is worth to point out that, by using only the neoclassical asymmetric fluxes in the ambipolar equation, it is assumed that the anomalous transport is automatically ambipolar. The good agreement between calculated electric field and experimental one seems to confirm that, in these discharges, the anomalous transport is in fact ambipolar.

The ambipolar equation has only one solution in whole plasma range for this plasma configuration, as is shown in figure 7.15. These results are in concordance with previous studies using the same transport code, as showed in previous chapters. This situation is a common feature in TJ-II scenarios due to the ratio $Te/Ti >> 1$, since there is no heating

power for the ions. This ratio is the key point for the transition from one solution of the ambipolar equation to three solutions.

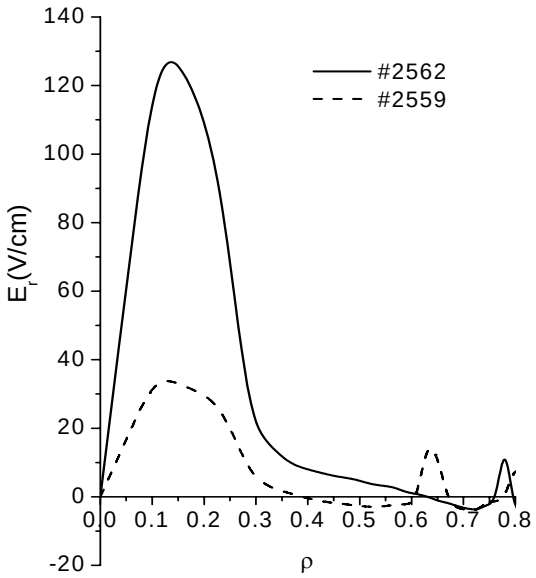

Figure 7.14 Calculated electric field profiles in the case of #2559 and #2562 shots.

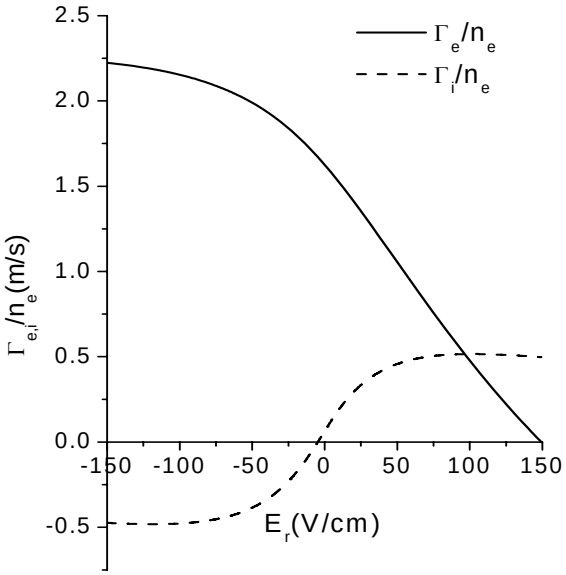

Figure 7.15 Neoclassical electron and ion fluxes at ρ=0.25 for #2562 shot.

From figure 7.14, it can be seen that not just electric field is increased but electric field shear too in #2562 shot. In order to quantify this change the electric field shear has been plotted in figure 7.16. The maximum value is at the plasma center corresponding to #2562 shot, $dE_r/dr \approx 500$ kVm^{-2}, whereas for #2559 shot is $dE_r/dr \approx 180$ kVm^{-2}. But for $\rho \approx 0.1$ $dE_r/dr \approx 300$ kVm^{-2} in #2562 case and $dE_r/dr \approx 0$ kVm^{-2} in #2559 shot. These values are comparable to similar eITB shots observed in tokamak experiments [Bur97] as well as in stellarators [Min04].

Both the electric field and electric field shear could be important parameters for the eITB formation. Nevertheless, the hollow density profile indicates that ECRH-pump out flux is far from being negligible. In CHS it has been observed a diminishing of turbulence, but no particle transport reduction is seen.

It is worth to point out that even the transition between positive and negative electric field is soft, the electric field has a great shear in the plasma core. However, if the ion temperature increases a sudden transition is possible and the effect of transport reduction may become even more important.

Comparing these results with the ones obtained in the LHD case, one can conclude that in the eITB case, the electric field obtained is very similar in both cases. It has a high value and a high shear at the plasma core, whereas in the outer part of the plasma, it has small values. Looking at the neoclassical electron diffusivities in figure 7.17, and comparing with the ones obtained in the LHD case (see figure 7.10), one can conclude that electron neoclassical transport levels may be more important in the plasma core in the TJ-II case than in the LHD one. This feature is closely related to the fact that the TJ-II device is not designed to optimize neoclassical transport.

From the analysis, electron thermal diffusivities are obtained. It is shown in figures 7.18 and 7.19 that there is a significant drop of the electron thermal diffusivity in the eITB plasma, $1 \le \chi_e \le 10\,\mathrm{m^2/s}$, compared with non-eITB shot, $1.5 \le \chi_e \le 14\,\mathrm{m^2/s}$ in the range $0 \le \rho \le 0.5$. The neoclassical diffusivity for the #2562 shot is rather similar to the obtained with Monte-Carlo techniques [Cas04], however, in the case of #2559 although central values are different, the profile is similar.

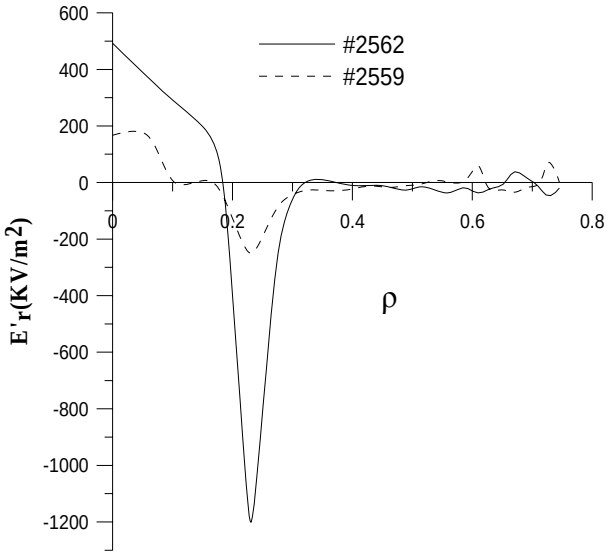

Figure 7.16 Electric field shear for #2562 (solid) and #2559 (dashed) shots.

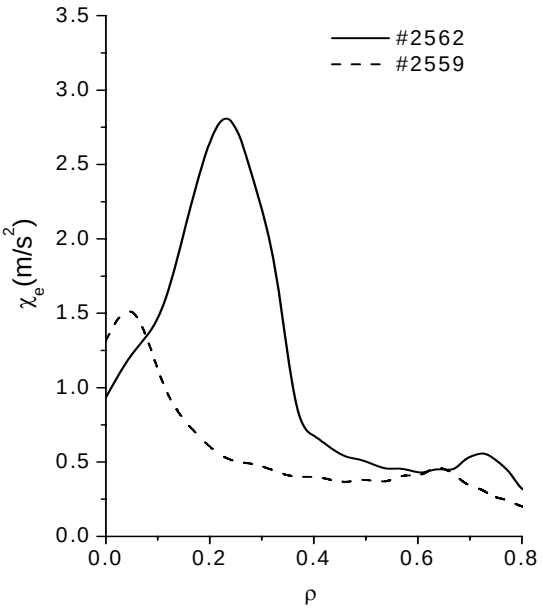

Figure 7.17 Neoclassical electron diffusivities profiles.

In order to see clearly the transport reduction to neoclassical values a comparison of experimental diffusivity and the neoclassical one has been done for every shot in the range $0 \le \rho \le 0.5$ in figure 7.18 and figure 7.19. It is clear from figure 19 that in #2562 shot those experimental and neoclassical values are comparable (consequently anomalous

transport is smaller) in the $0 \le \rho \le 0.2$ range. From figure 7.19 there are just comparable values of both profiles in $0 \le \rho < 0.05$ range for #2559 shot. According to these data, it seems clear that there is an electron diffusivity reduction in plasma center to neoclassical values in the case of low-density scenarios. This reduction is localized in the plasma range where $dE_r / dr > 0$.

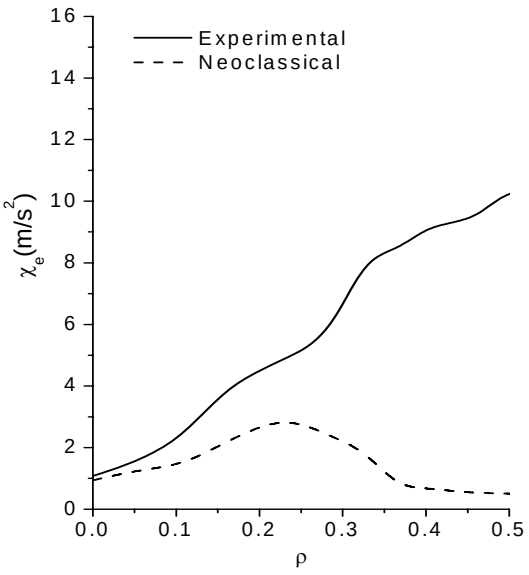

Figure 7.18 Comparison between experimental and neoclassical electron diffusivity profiles in the plasma core for shot #2562.

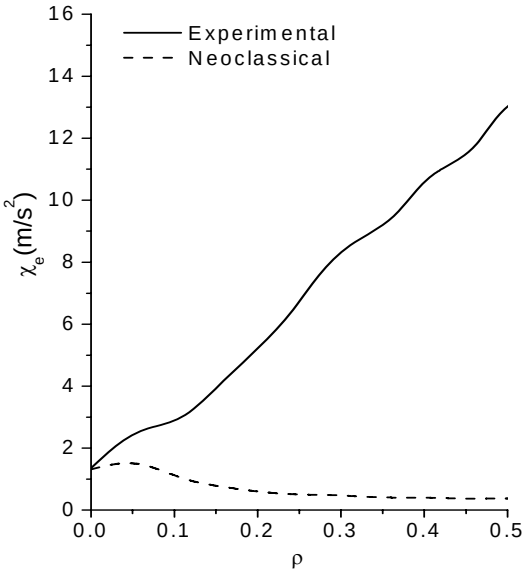

Figure 7.19 Comparison between experimental and neoclassical electron diffusivity profiles in the plasma core for shot #2559.

As a new contribution of this thesis, comparing the eITB TJ-II results with the ones obtained previously for the LHD case, one can see that the heat transport behaviour at the plasma core is quite similar (anomalous transport being even smaller than neoclassical one at the plasma center) although in the TJ-II case the neoclassical transport seems to play a more important role than in the LHD case, as deduced from figure 7.18.

7.3.4 Hollow density profile explanation

From experimental data and transport analysis it is known that plasma regions with high E_r correspond with high electron temperature gradient, $|\nabla T|_e$ [Ida03], thus in the plasma core $E_r \propto |\nabla T|_e$. In the model previously described the sheared electric field is

responsible of anomalous transport reduction, we can conclude that $E_r^{'} \propto \left(-\frac{\partial^2 Te}{\partial r^2} \right)$. So, if we consider that $T_e \propto n_e^{-\beta}$ in a small volume of the plasma center we conclude that $E_r^{'} \propto \left(\frac{1}{n_e^{\beta+1}} \right) \left(\frac{\partial^2 n_e}{\partial r^2} - \frac{(\beta+1)}{n_e} \frac{\partial n_e}{\partial r} \right)$ with $0 < \beta \leq 1$ in a narrow region of the plasma core. This expression shows that the key factors for the onset of a high electric field shear are low densities, in this plasma regime, $\frac{\partial^2 n_e}{\partial r^2} \geq 0$ plasma zones and $\frac{\partial n_e}{\partial r} \leq 0$ regions. Particularly important seems to be the factor $\frac{\partial^2 n_e}{\partial r^2}$, which reflects the fact that the more hollow the density profile, the steeper the eITB is. And this happens when a positive radial electric field appears which is always accompanied by a sheared $E \times B$ flow. The key factor to provoke all these features is the relation between absorbed power density and electron central density. These characteristics are common in almost all the enhanced heat confinement shots in TJ-II.

7.4 Conclusions

Some new transport models have been added to the TOTAL code for analysing the eITB formation in the LHD. The shot #26943 as well as a study of the eITB density sensitivity has been carried out.

Results show that the anomalous transport is reduced at the plasma core by the electric field shear leading to the eITB formation. The factor $\left(1+(\tau f_{ExB})^{\gamma}\right)^{-1}$ introduced in the TOTAL code is able to simulate the transition between the regime with non-eITB and the eITB scenarios. As this dependence on the $E \times B$ flow has been also used with eITB tokamaks plasmas leading to satisfactory results, we can conclude, as a new contribution of this thesis, that although the source of the electric field is different for tokamaks and stellarators, its shear seems to suppress heat turbulent transport in both devices.

Related to the heat transport channel, it has been shown that, at the plasma core, electromagnetic drift waves are probably responsible of the anomalous transport in the eITB scenarios. With this model, the high electron temperature gradients located at the plasma core have been obtained. However, outside the central region, short drift waves are not able to simulate electron plasma temperature because the profiles obtained have too high temperature gradients. In this region, more suitable models are related to long wavelengths models (as electrostatic drift wave or GyroBohm-like models). In this

situation, and as a new contribution of this thesis, a new model mixing both types of transport has been proposed. The transition is located calculated using the expression $\beta_{crit} = L_T^2 / q^2 R^2$, derived from the condition that the characteristic length of both type of transport was the same. Using this model and different electron average densities with the same profile, the experimental central temperature dependence, $T_e(0) \propto < n_e >^{-0.57}$, on density as well as the whole profile have been reproduced with reasonably accuracy, simulating the critical transition between non-eITB and eITB shots. Therefore, and as a new contribution of this thesis, a new model electron heat transport model has been created mixing short and long wavelengths, which is able to simulate eITB behaviour.

From the results previously described, a transition from large convective cells to small ones is expected at the transition from non-eITB to eITB scenarios at the plasma core when $\beta > \beta_{crit}$. However, the presence of large convective structures even at the plasma core cannot be discarded. The electron temperature profiles obtained with a GyroBohm-like model show that the critical transition between non-eITB and eITB scenarios is well simulated. However, the profiles obtained, even inside the error bars, seem to be more parabolic that the experimental data. Moreover, the central temperature dependence on density, $T_e(0) \propto < n_e >^{-0.72}$, is not so similar to the experimental one like the one obtained from the electromagnetic model. However, the dependence in the non-eITB scenarios is well simulated.

In this situation, electromagnetic drift waves are expected to drive anomalous transport in the eITB scenarios but more experiment must be done to check it.

In order to compare these results with the ones obtained in the TJ-II case, the electric field and thermal electron diffusivities have been analyzed for the electromagnetic and GyroBohm-like scenarios in the eITB case. In both cases the profiles obtained for the thermal diffusivities are very similar and they are always higher than the neoclassical ones. However, in the electromagnetic case, the thermal diffusivity at the plasma core is very close to neoclassical values. This characteristic is related to the fact that in the electromagnetic case, steeper electron temperature gradients are obtained. As this type of profile seems to be closer to experimental data than the one obtained with GyroBohm-like models, it seems reasonably conclude that in a narrow region in the plasma core, the transport seems to be neoclassical in the eITB scenarios of the LHD.

A new transport model (electromagnetic drift wave) has been added to transport code PRETOR-Stellarator in order to analyze the transport properties of eITB shots in TJ-II. The

main characteristic of this transport model is its strong dependence with electric field shear.

The results show that this transport model has simulated reasonable well the temperature profile of shots with eITB and without eITB. For both discharges the electric field obtained has a high value at the center and a small one close to the edge, but in the case of eITB, this central value is much higher, 130 V/cm, compared to 38 V/cm. Although there is only one solution of the ambipolar equation (due to the fact that $Te/Ti >> 1$) the electric field structure shows that a high electric field shear associated with the formation of the eITB. These calculations are in concordance with studies made at CHS, LHD and W7-AS. Both effects (high electric field and high electric field shear) seem to be the key factors for the eITB formation, although more studies have to be done in order to clarify what effect is stronger.

Neoclassical calculations show that a reduction of thermal diffusivities to neoclassical values appears at plasma center in the eITB scenarios. Nevertheless, neoclassical transport cannot explain global transport because thermal diffusivities only coincide with neoclassical values for the eITB shots in the range $0 \le \rho \le 0.2$, whereas it is higher outside.

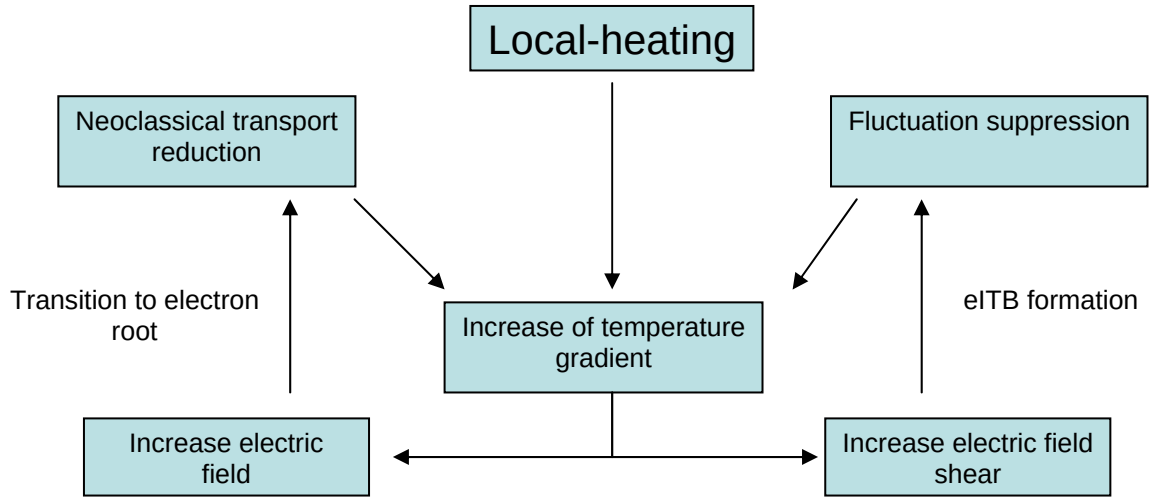

Figure 7.20 Flow chart of the electric field role on the eITB formation in a stellarator fusion device

As a new contribution of this thesis, these results yield to the conclusion that the reduction of anomalous (turbulent) transport is due to the combined effect of a high electric field with a high electric field shear and the appearance of small convective cells due to short electromagnetic drift waves.

Finally, the role of the ambipolar electric field has been summarized in figure 7.20. This flow chart is important not just for eITB formation due to low densities scenarios, but for scenarios where the eITB is formed independently of the average density values. In those cases, the eITB is formed due to the existence of rational values of the rotational transform that make possible the appearance of magnetic islands. In this case, as well as in the low density cases, the electric field and its shear are expected to suppress anomalous transport. Further studies with PRETOR-Stellarator will be done in order to check this hypothesis.

Chapter 8

Analysis of non-diffusive electron heat transport phenomena

8.1 Introduction

Transport is usually described in fusion plasmas using local approaches for fluxes (particle and energy), independently whether the transport is neoclassical or anomalous. With this local approach, the heat flux can be described as,

$$q_e(r,t) = -n_e(r,t)\chi_e(r,t)\nabla T_e(r,t) \tag{8.1}$$

where the total electron thermal diffusivity, χ_e, is the result of adding to the neoclassical thermal diffusivity, $\chi_{e,neo}$, the anomalous one, $\chi_{e,an}$, $\chi_e = \chi_{e,neo} + \chi_{e,an}$. In this framework, the pressure equation for electrons

$$\frac{\partial}{\partial t}\left(\frac{3}{2}n_e(r,t)T_e(r,t)\right) = -\nabla q_e(r,t) + \sum Q(r) \tag{8.2}$$

where, n_e, T_e, q_e and $Q(r)$ represent the electron density, electron temperature, electron heat flux and sources/sinks respectively, can be closed easily. The "local approach" means that the variables involved in equation 8.2 depend exclusively on the point r where each one is calculated. Although some turbulent properties of the plasma can be explained in this framework, it remains the problem of whether heat dependence on the local

temperature gradient is physically consistent. The lack of a universal description of $\chi_{e,an}$ for all the magnetic confinement devices and in any situation is a fact that indicates the possibility of better descriptions of this issue.

Moreover, some characteristics of the plasmas are hardly understood in the framework previously described. Some examples are the fast response of the plasma core to the some plasma changes, e.g. plasma transition L-H, propagation of sawteeth, heating power switching, impurity injection or ballistic propagation of cold pulses. These phenomena are treated in general, by adding a convective term in the heat flux definition, conserving, however, the local dependence on the temperature gradient. In any case, some problems arise of adding this term to the heat flux definition. Perhaps the main one is that its physical significant is not clear yet. Moreover, this term should cancel in some situations and active in other ones, but any of the present models has this characteristic and it seems difficult to introduce such features in any diffusive model.

The cold pulses propagation are particularly studied is in the confined plasmas. When a sudden perturbation (cooling the plasma) is localized at the plasma edge, it propagates inward with a velocity which would be not expected from a diffusive transport model. Cold pulses with these characteristics have been observed in many devices as: JET [Gal98], TFTR [Kis96], TEXT [Gen97], W7-AS [Kop00], LHD [Ina04] and TJ-II [Mil02]. A similar behaviour is obtained when a perturbation is localized in the plasma core. The propagation is outward in this case, but its behaviour is similar to the cold edge pulse.

Another important characteristic of this transport is that the system seems to adjust itself to accommodate larger and smaller fluxes with the same plasma parameters. This phenomenon has been called “non-local” transport. The main characteristic of the non-local transport is that its values do not depend only on the local values of the plasma variables, but on the values of the same variables calculated at another points.

Some physical studies have been done related to this non-local behaviour of heat transport. Experimental measures done at the edge plasmas of some fusion devices [Bud03] suggest the existence of non random behaviour of plasma fluctuations with non-Gaussian statistics. Instead of that, fractal properties have been discovered. The existence of such fluctuations could lead to a kind of structure with stochastic processes known as Levy-type process [San05], which would generate long correlated fluctuations and the ballistic transport previously described. Particularly important seem to be that the correlations between different points in the plasma are far from being Gaussian. This fact could be related to a reduction in the system’s degrees of freedom. It also important to point that these long correlated structures imply faster coherent events propagation

compared with the classical diffusion transport. The velocities could reach the 150-2000 m/s range, up to ten times faster than in the diffusion case. Analyzing these facts, one can conclude that these Levy-type processes could be the source of the anomalous transport together with small scale diffusion.

Previous studies with non-local transport models have been done with successfully results. A similar model than the one used in this thesis has been applied to simulate transient responses, e.g. power switching and power modulations experiments. In a similar way, the transient response of the core plasma after a L-H transition has been correctly explained using non-local models. Recently [San05], probabilistic transport models (with non-local effects) have been also applied in order to study the behaviour of the plasma density. However, none of these studies have been able to explain all the non-local transport features.

The purpose of the study performed in this thesis is the analysis of anomalous transport from the non-local point of view by means of a non-local transport model. In this model, the local heat flux is expressed in terms of the local flux of the rest of the plasma via an integral description. This approach gives the possibility of the study of a global heat flux in fusion plasmas.

In order to reach this purpose, this study is divided into two parts. In the first one, steady- state plasmas in the LHD are studied with a non-local model. In the second part, strictly non-local phenomena as cold pulses are studied.

8.2 Model description

In neoclassical transport theory the transport coefficients are computed averaging the moments of the first order correction to the distribution function over each flux surface. Therefore, neoclassical fluxes describe only the local diffusive transport. This approach is valid for some magnetic configurations, however, for configurations where many particle orbits have large deviations from their birth surface, non-local contributions to the particle flux have to be considered. The impact of these non-local fluxes is especially severe for transport in stellarators because of their strong dependence on the radial electric field, which in turn becomes non-local. The existence of these non-local particle fluxes may lead to non-local heat fluxes too. Thus, in order to study this possibility, a non-local neoclassical transport model has been chosen to study the non-diffusive electron heat transport phenomena described in section 1.

The global non-local heat flux model used is described using an integral definition,

$$q_e(r,t) = \int q_{neo}(r',t)K(r'-r)dr' \tag{8.3}$$

This model for the turbulent transport can be seen as a convolution over the neoclassical heat transport. The factor $K(r'-r)$ is the weighting (density in probability theory) function which takes account of the behaviour of the heat flux in every point of the plasma. In the case when $K(r'-r)=\delta(r'-r)$, the neoclassical heat flux is obtained, therefore, in the situations where the plasma has a transition between strong anomalous behaviour and neoclassical heat fluxes the factor $K(r'-r)\to\delta(r'-r)$, whereas that in L-mode, $K(r'-r)$ must to take account the non-local effects of the transport. One could expect that the Gaussian distribution $\frac{1}{\sqrt{\pi}\sigma}\exp\left[-\left(\frac{r'-r}{\sigma}\right)^2\right]$ (being σ a correlation length) is a good candidate for $K(r'-r)$ because in the limit $\sigma\to 0$, $K(r'-r)\to\delta(r'-r)$. However, the simulations with this density function are not correct independently of σ unless the heat transport in the plasma is close to neoclassical values.

In this situation and could expect that whether in the plasma there are long correlations between very distant points that may not be reflected by a Gaussian distribution. Such long correlations may induce an vary large variance, $<r^2>\to\infty$, in the plasma. This characteristic is typical in some studies in economy and in turbulence [Man77]. This behaviour leads to a very important issue, which is the invariance under changes of scale. The fact that, $<r^2>\to\infty$, implies some potential distribution in the limit, $p(r)\sim r^{-\alpha}$. This kind of distribution is typical in many fractal studies [Man77].

One probability density function that can solve some of the problems previously described is the levy distribution. The characteristic function is defined as $\varphi_\alpha(a,k)=e^{-a|k|^\alpha}$ and therefore the density function is $p(r)=\int e^{-ikr}\varphi_\alpha(a,k)dk$, with $0<\alpha\le 2$. For $\alpha=2$, it reduces to a Gaussian distribution, and for $\alpha=1$ to a Cauchy distribution. There are some important features about levy distribution:

- They are stable under addition, i.e. a distribution of n random Levy variables approaches a Levy distribution (Levy stable laws)
- For $1<\alpha\le 2$, $<r^2>\to\infty$, however $<r><\infty$.
- For large r, the tails of the distribution are $p(r)\sim r^{-\alpha-1}$.
- The central behaviour of the distribution is close in shape to a Gaussian distribution.

The key point with this distribution is the tails $p(r) \sim r^{-\alpha-1}$ for large r. In figure 8.1 there is a comparison between Gaussian, Cauchy and Levy distribution. As can be seen, the tail decay may be responsible of the long distance correlations in the transport model applied in this paper.

8.3 LHD configuration

Under the assumption that $K(r'-r)$ is a levy distribution (with $\alpha = 0.5$), the electron pressure equation 8.2 is solved using the non-local transport model presented in equation 8.3. The source term is modelled as a Gaussian (in the next paragraph the form of this Gaussian will be shown) and the sinks correspond to bremsstrahlung losses. For these calculations LHD-like parameters are used, i.e. R=3.6 m, a=0.6 m, B=1.5 T and P_{ext}=2.5 MW. The electron density is kept fix in time with an almost flat profile.

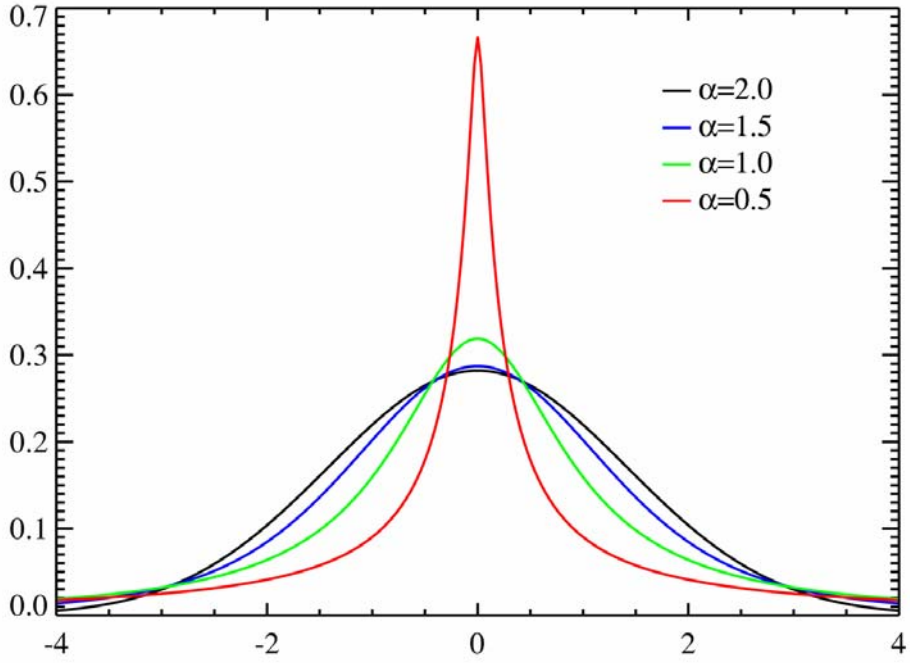

Figure 8.1 Shape of the Gaussian and Cauchy distributions compared with the Levy distribution for different α.

8.4 Steady-State simulation results

In order to analyze the goodness of the transport model to simulate steady-state discharges several plasma conditions have been chosen. The average densities used in this study are shown in table 8.1. Their profiles are the typical density profiles obtained in the LHD. Two input power profiles have been used. The first one is an on-axis Gaussian

Electron Cyclotron Resonant Heating (ECRH) modelled as $\sum Q(r) \sim \exp\left[-\left(\rho/0.3\right)^2\right]$ and the other one is an off-axis Gaussian ECRH heating $\sum Q(r) \sim \exp\left[-\left((\rho-0.2)/0.3\right)^2\right]$.

Density profile	Average density (x 10^{20} m^{-3})
1	0.11
2	0.22
3	0.32
4	0.42

Table 8.1 Average electron densities used in the density study.

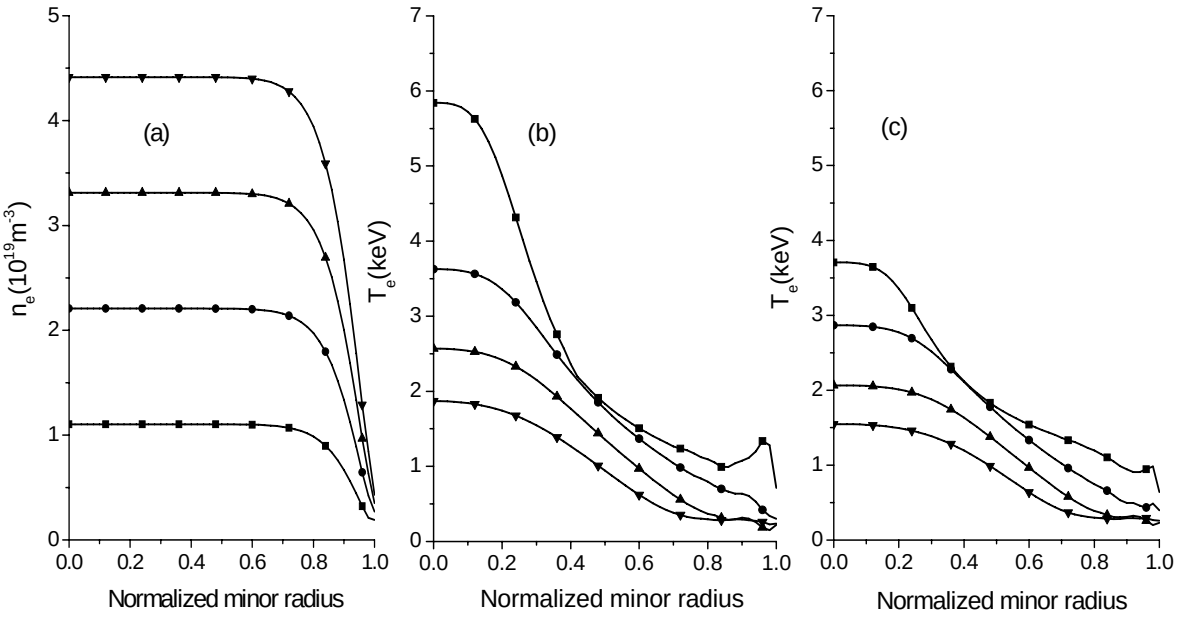

Figure 8.2 Electron density profiles used for the steady-state study (a). Electron temperature profiles obtained by means of the non-local model with on-axis Gaussian ECRH heating (b) and off-axis Gaussian ECRH heating (c).

The electron density profile used in each simulation and the electron temperature profiles obtained are given in figure 8.2. As can be seen from the figures, the profiles obtained with this model are quite parabolic, as expected from the experimental LHD shots with $\langle n_e \rangle > 1\times10^{19} m^{-3}$. According to this model, in the on-axis heating case, central temperature has a strong dependence on the density. In this situation, higher temperature gradients are obtained in the plasma core as density is decreased. This fact is a common

characteristic in LHD plasmas and it leads to the ITB formation.However, in order to get an ITB scenario, a critical transition on the density should be obtained, and, in this simulation, no clear critical transition has been obtained. In the off-axis case and according to figure 8.2 there is not a so strong dependence on density, thus, in order to obtain high temperature gradients at the plasma core, it would be necessary to perform simulations with lower average densities.

In order to see clearly how this model simulates the LHD plasmas, it has been decided to perform a simulation of the #26943 LHD shot and to compare the results with the ones obtained by means of other models in the previous chapter. However, in order to simulate an eITB shot, the model described in section 8.2 is not completely satisfactory, since the kernel used tends to give to many correlations betweens different points, leading to a high heat transport. In the eITB case, where neoclassical transport tends to be important, a better kernel might be a Gaussian one. However, the transition between both kernels does not seem an easy problem. Instead of that, the same model used in the previous chapter has been used in this one, that is, the reduction of heat transport by means of electric flied shear. So, finally the heat transport is described as follows,

$$q_e(r,t) = \frac{q_{e,ano}(r,t)}{\left(1+(\tau f_{ExB})^{\gamma}\right)} \tag{8.4}$$

where $q_{e,ano}(r,t)$ is the heat flux defined in equation 8.3. (The same values for τ and γ have been used here).

Density profile	Average density (x 10^{20} m^{-3})
1	0.07
2	0.09
3	0.11
4	0.22
5	0.32
6	0.52

Table 8.2 Average electron densities used in the non-local transport analysis of the LHD eITB #26943 scenario.

Average densities used in this simulation are given in table 8.2. In figure 8.3 results of the electron temperature profile (left) as well as the dependence of the central temperature with average density (right) are given. With this model, a critical transition of the temperature is observed and some eITB scenarios are obtained. The temperature

profiles are similar to the GyroBohm-like models ones for the eITB scenarios (see previous chapter). These profiles obtained are particularly well simulated for the very low density profiles as can be seen from figure 8.3.

Comparing the simulation performed with $\langle n_e \rangle = 0.7 \times 10^{19} m^{-3}$ and the experimental electron temperature profile from #26943 shot, the values are quite comparable in whole plasma radius. The central temperature dependence with average density, $T_e(0) \propto < n_e >^{-0.74}$, is also very similar to the one obtained in the GyroBohm-like case. However, in the non-eITB region, central temperature dependence with density, $T_e(0) \propto < n_e >^{-0.63}$, is higher.

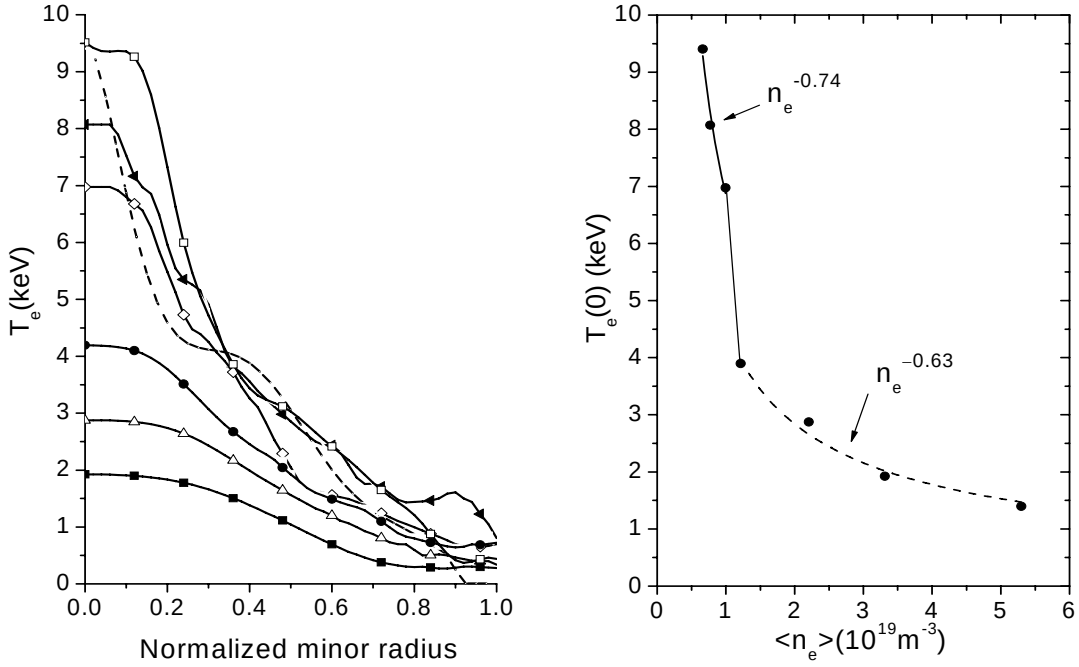

Figure 8.3 Electron temperature profiles obtained with the non-local model for the different electron average densities (left). Central temperature dependence on average density (right).

Results show that, although the eITB scenarios are well simulated with this model, the global results are not so similar to the experimental ones that the previously obtained. Therefore, more studies must be done in order to use this model to analyze and simulate LHD data.

8.5 Turbulent heat pulse studies

Although the steady-state results obtained in the previous section with the non-local model are reasonably correct, more studies must be done in order to improve the results. However, the global objective to make a non-local model is not to simulate a steady-state scenario but to simulate turbulent transient phenomena and non-local turbulent transport as cold pulses or ballistic transport. With the aim of performing such simulations, the non-local transport model proposed in this thesis in equation 8.3 will be used along this section as follows. A perturbation is introduced in the density profile for 0.5 seconds at the plasma edge in a steady-state scenario, as showed in figure 8.4. The perturbation propagation on the electron temperature is analyzed using the non-local formalism and a typical anomalous (diffusive) transport model (in this case, a simple LHD [Yam04] scaling has been used). The delay time and the shape of the perturbation have been studied for different plasma points and for each transport model.

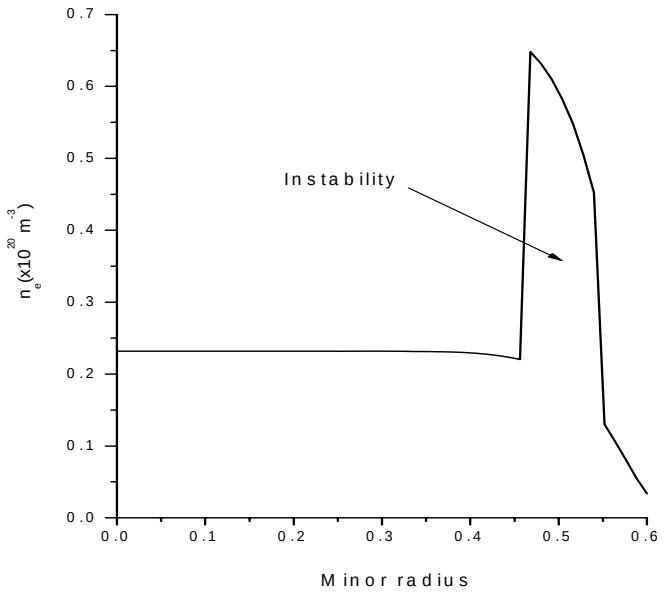

Figure 8.4 Instability introduced in the electron steady-state density at the plasma edge. The perturbation lasting time is 0.5 s.

Calculating the delay time and the distance from the perturbation to some different points, the local speed is calculated for each transport framework. This speed is showed in figure 8.5. As can be seen from the figure, several differences arise from the two points of view analyzed in this thesis.

First, the obtained speeds are really faster in the non-local case, with $v \approx 250\ m/s$ at the plasma edge and $v \approx 300\ m/s$ in the core. In the local case, these speeds reduce to $v \approx 120\ m/s$ and $v \approx 50\ m/s$ at the edge and the core respectively. Therefore, with the non-local transport model the speeds obtained could be up to 8 times faster at the plasma core than the ones obtained by means of the local model. This characteristic is a typical fact in many transient phenomena studied in several fusion devices [Bud03]. Related to the velocity values, some studies have been carried out in order to measure the inward and outward coherent events speed. The values obtained for some devices (including the LHD divertor plate probe) are in the range $150 < v < 2000\ m/s$ [Bud03]. Therefore, as a new contribution of this thesis, the results of the model studied seem to be within the experimental range.

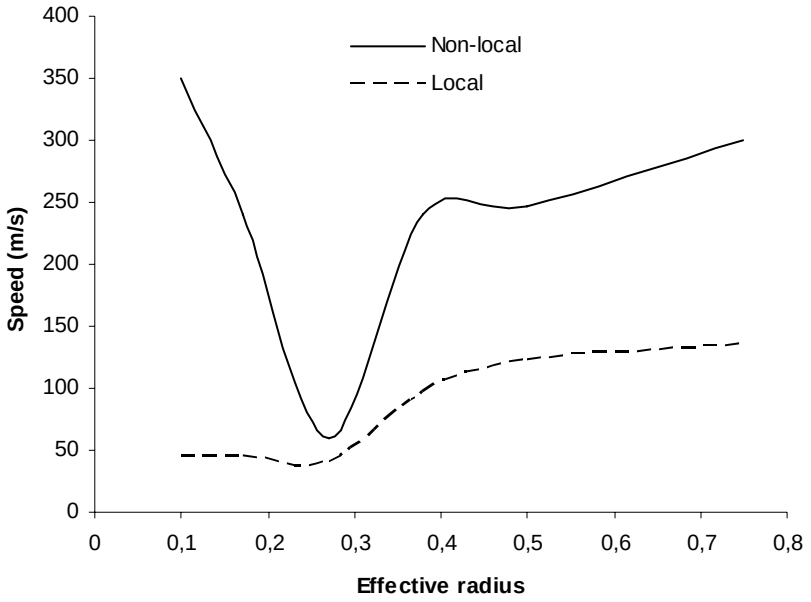

Figure 8.5 Instability propagation velocity for different plasma points.

On the other hand, another important difference arises from figure 8.5. Although in both cases the perturbation has a sudden velocity reduction at $\rho \approx 0.3$, compared with the plasma edge values, in the non-local scenario the speed seems to increase from that point towards the plasma centre. In the local case there is not such behaviour, moreover, the speed tends to be constant. The reason for the velocity reduction in the plasma core in the diffusive framework is that in the stellarators, the thermal electron diffusivity tends to be smaller in the plasma core than at the plasma centre or edge. In this situation, the diffusion propagation speed is expected to be reduced in the plasma core. However, this fact is not

observed in the experimental studies carried out with some cold pulses propagation experiments in the TJ-II [Mil02] as well as in the LHD [Ina04] where sudden velocity increasing was found in the plasma core. Therefore, the model presented in this thesis, based in a non-local heat transfer, reproduces experimental data with reasonably accuracy. The physical reason for this increasing is not clear yet, however, a possible explanation arises from the model used in this study. The velocity growing obtained is due to the combination effect of the correlation function used between different parts of the plasma (Levy distribution $K(r'-r)$) and the typical neoclassical heat transport increasing in the plasma core.

Anyway, more simulations with more fusion devices must be done using this model in order to check its goodness to simulate transient phenomena and the physical conclusions that follow from it.

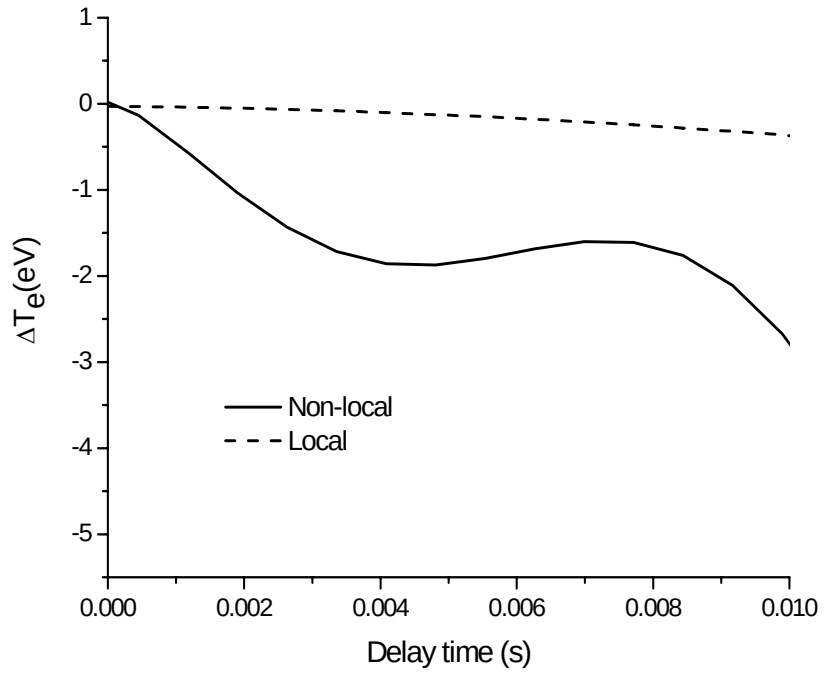

Figure 8.6 Temperature increment at $\rho = 0.3$ due to the perturbation propagation for several delay times after the perturbation begins. The solid line corresponds to the non-local model and the dashed one to the local framework.

There is another important difference between the non-local and the diffusive framework simulation. That is the way the perturbation travels along the plasma. In figure 8.6, the difference between the steady-state electron temperature and the perturbed temperature for one plasma point is showed for different delay times after the perturbation begins. As expected from diffusion framework, the perturbation travels much slower and

the temperature changes smoothly. However, in the non-local case, temperature variation is much faster and, as can be seen from figure 8.6, the perturbation front seems to travel more compact, since there is a quick drop in the temperature and a partial recuperation later. Therefore, in the first transient moments, no smooth temperature changes have been obtained in the non-local case. Perhaps, the way the perturbation travels through the plasmas is the main difference between a non-local point of view of heat transport and the traditional diffusive framework. This characteristic is usually called ballistic transport and it has been reported experimentally in the TJ-II. A schematic picture showing how the perturbation travels using the non-local model used in this thesis is given in picture 8.7. In any case, it is also possible to obtain "non-local" phenomena using a complete diffusive framework by adding a pinch term, $V_{p,e}$, in the particle flux as follows,

$$\Gamma_e(r,t) = -D_e \nabla n_e(r,t) + n_e(r,t) V_{p,e}(r,t) \tag{8.5}$$

However, this term should change its value depending on the plasma conditions (from steady-state scenarios to transient scenarios) and it does not seem an easy problem to solve. Moreover, this pinch term would change its sign depending whether the perturbation travels inward or outward, whereas with the non-local model proposed in this thesis, similar results to the ones obtained in the perturbation case analyzed in figure 8.4 are obtained if the perturbation is localized in the plasma core.

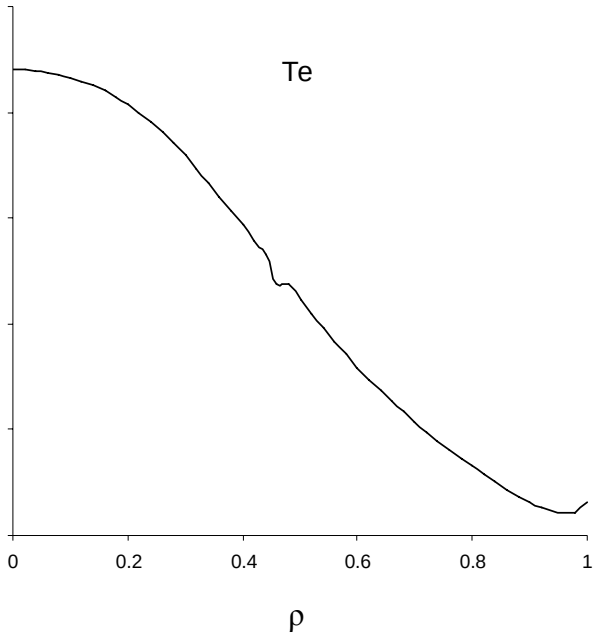

Figure 8.7 Schematic representation of the perturbation propagation obtained by means of the non-local model. Unlike in the local transport, the perturbation tends to keep its shape along the travel throughout the plasma.

Although the propagation front tends to keep its shape along the propagation through the plasma there is an important change in the intensity of the instability. From experimental data from tokamaks [Man02] as well as from stellarators [Ina04] it has been shown that the temperature instability tends to be minimum around $\rho = 0.3 \sim 0.4$ and it is maximum close to the plasma edge and in the plasma core. The data obtained by means of the non-local model derived for this thesis show a very similar maximum amplitude profile, as it is shown in figure 8.8. It has a minimum at $\rho = 0.4$ and strong growth from that point to the edge and the plasma core. From the analysis of the simulated data tails, the following expression for the maximum cold pulse amplitude has been derived,

$$\left|\Delta T_{e,\max}\right| \sim e^{|\rho-\rho_0|} \tag{8.6}$$

where ρ_0 is the position of the minimum cold pulse amplitude. In order to check the validity of the model this formula is useful, since it allows comparing directly the experimental data and the prediction.

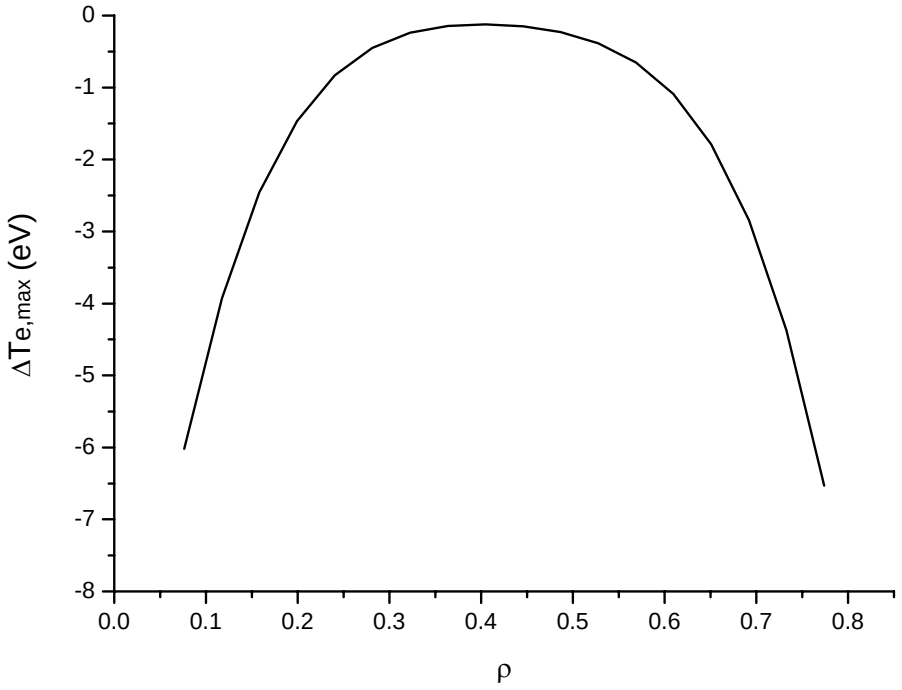

Figure 8.8 Maximum cold pulse amplitude obtained by means of the non-local model. Unlike in the local transport, the cold pulse propagation has minimum amplitude close to the plasma center and maximums at the edge and in the core.

8.6 Conclusions

The electron heat transport channel has been studied from a non-diffusive point of view by means of a non-local heat transport model. The aim of this study is to simulate the non-local phenomena appeared in some transport studies carried out in several fusion devices, as cold pulses or heat pulses inward and outward the plasma.

A convolution over the neoclassical transport has been chosen as a first approximation to the non-local transport phenomena in fusion plasmas. The weighting factor in the convolution definition has been chosen to accomplish some necessary features. The first one is that in the limit with no turbulent transport, that weight factor should lead to neoclassical transport. Second, and according to some experimental data, the correlation between different points in the plasma is far from being Gaussian. Moreover, long tail correlations are present between very far points. Therefore, a non-Gaussian distribution should be taken into account to simulate these non-local phenomena. Finally, a levy-type distribution (Levy flight) has been introduced in the heat transport channel. This distribution has been studied in the non-local phenomena elsewhere before in some analysis about density profiles [San05]. This distribution yields to fractal behavior, which has been found to be present in some experimental studies [Bud03].

According to this non-local heat definition, the pressure equation for electrons has been solved for a LHD-like fusion device. The neoclassical diffusivities used along the work have been described in previous chapters. In order to see clearly how the model simulates the plasma characteristics, two different plasma conditions have been selected. In the first case, steady state plasma conditions have been simulated. On the other hand, purely transient phenomena have been also analyzed.

According to the steady-state studies performed with the non-local model, the electron temperature profiles obtained for several average densities are quite parabolic, which might be expected for that average density range according to the experimental data. In the on-axis heating case, central temperature tends to have a high increasing for low average densities. This behavior could yield to eITB scenarios for very low average densities. However, as the weighting distribution introduced in the heat transport model proposed in this thesis, induces long correlations even for far distant points, it is difficult to obtain an eITB scenario. In order to overcome this difficulty, and, as proposed in the previous chapter, the turbulent transport reduction by means of $E \times B$ shear flow has been introduced also in this non-local description. As a new contribution of this thesis, the results obtained show good agreement between an eITB experimental shot from the LHD and the simulations. The critical density dependence obtained is very similar to the Gyro-

Bohm results obtained in the previous chapter for very low average densities. However, in the high densities scenarios, a too strong dependence has been found.

Whereas the steady-state simulation in a fusion device can be understood in a completely diffusive framework, some transient phenomena, as heat or cold pulses, are difficult to analyze in such framework. In order to study how the transport model introduced in this thesis works with transient plasmas, a sudden instability has been introduced in the electron plasma density localized at the edge.

Some important differences arise from the comparison between a diffusive transport and the non-local one. First, the instability propagation velocities are quite higher in the non-local case. According to the model proposed, in the LHD case, the velocities obtained are in the 200-300 m/s range, whereas in the diffusive model the velocities are quite smaller. These speed values are in the range of experimental data obtained for that device [Bud03].

Second, in the non-local case, there is a sudden drop in the instability velocity propagation at ρ=0.3, however, the speed tends to increase again in the plasma core. This feature has been checked in the LHD and the TJ-II devices. Therefore, this model simulates with reasonable accuracy transient experimental data. According to the model proposed, this increasing is due to the combination of the weighting function (Levy Type) chosen and the neoclassical transport increasing at the plasma core. Very different behavior is obtained in the diffusive framework, where, although a drop in the velocity is also obtained, the speed at the plasma core tends to be constant.

Finally, as a new contribution of this thesis, the way the instability travels along the plasma has been found to be very different in the two frameworks studied. In the non-local case, the instability tends to keep its front compact along the travel throughout the plasma. However, in the diffusion case, the instability becomes smoother while propagating in the plasma. This phenomenon, ballistic transport, has been checked in the TJ-II device [Mil02], and the results obtained here seem to be in the right direction.

Therefore, as a final contribution of this thesis, the non-local model studied reproduces with reasonably accuracy steady-state plasmas as well as transient phenomena, although more studies must be done to check its goodness with more fusion devices and more plasma regimes to take a final decision about its validity. However, this model is one of the first attempts to explain many transient experimental phenomena as well as steady-state plasmas.

Finally, this model must be improved even more, first checking the results with other devices, e.g. TJ-II, and second, a physically meaning and a more formal mathematical background must be introduced in the model, since, although it seems to reproduce some aspect of non-local transport, no physical explanation to this phenomenon arises from the model.

It is worth to point out that this model suggests a possible relation between two apparently unrelated fluxes, neoclassical transport and anomalous transport, and that a possible method to reduce anomalous heat fluxes is to reduce neoclassical transport. This hypothesis has been also suggested in [Sha05].

Chapter 9

Steady fusion reactor characteristics. Comparison between helical and tokamak case

9.1 Introduction

The main goal of magnetically confined plasmas studies is to attain commercial fusion energy. Several possibilities are available in order to achieve this purpose, however, tokamak device fusion is, at the present time, the most attractive magnetically fusion concept due to the good confinement results. Moreover, the next-step tokamak device ITER, which will improve any fusion result obtained until now, will be build in the future. However, tokamaks have some inherent drawbacks, e.g. the induced current necessary to maintain the plasma equilibrium. In order to avoid this difficulty, the steady-state scenarios of a future tokamak commercial reactor are supposed to work with high temperatures and low induced currents (but with a high bootstrap fraction). This induced current might be even generated by Electron Cyclotron Resonant (ECR) heating method. However, in spite of these improvements, the current drive may be source of instabilities.

Unlike in the tokamak case, helical system offers the significant advantage of continuum operation regime, which means that the reactor works for several months without intermission. This purpose can be achieved by means of the superconducting magnetic coils that generate the three dimensional magnetic field optimized to confine the burning plasma. In order to maintain this steady-state regime, the superconducting coils should be cooled at a temperature similar or ever lower than the present LHD superconducting coils (4.4K). However, a possible drawback of this helical design is

closely related to the coils configuration, since the continuous helical coil might be difficult to maintain and repair. Therefore, superconducting coils that will work for 30 years with no serious difficulties are needed, and at the present time, more studies must be done to overcome this issue. In addition to this difficulty other problem arises from the helical concept for the future commercial reactor, since in order to obtain high stable β a very large reactor is expected. Therefore, the capital cost of this machine would be rather high. This issue should be overcome by analyzing other magnetic configurations with smaller aspect ratio and size, as it was pointed in chapter 2.

An important difference between the future helical and tokamak commercial reactors is the characteristic working regime. In the tokamak case, as previously pointed, high temperatures are needed in order to minimize the impact of possible current instabilities. In the helical case, neoclassical transport depends strongly on the effective ripple, and the heat transport losses due to helical ripple transport depend strongly on the temperature. Therefore low temperatures regimes are more suitable since neoclassical transport can be reduced. It is quite important to analyze the different operational working regimes of each fusion device, since the physical variables involved in obtaining burning plasmas can be really different in each case.

A complete simulation is carried out in next sections in order to analyze the main characteristics of the helical commercial reactor with the aim of comparing these results with the tokamak case.

9.2 Helical reactor simulation

For understanding the physical dynamics of the future helical commercial reactor, the radial profile analysis of several plasma variables, e.g. neoclassical and anomalous transport, density limit or neoclassical electric field is absolutely necessary. In order to do a complete analysis, TOTAL_P transport code has been used. The simulation parameters are given in next section.

9.2.1 Neoclassical and anomalous transport

The neoclassical model used along this study is the one described in section 3.3.2.8 of chapter 3. With this model asymmetric helical ripple transport as well as symmetric tokamak-like transport is included in the simulation. The ambipolar neoclassical electric field is also included.

Related to ion and electron anomalous transport, simple radial fits for heat diffusivity (similar to the experimental ones obtained) have been chosen,

$$\chi_{e,i} \propto \frac{\left(1+g\rho^{m}\right)}{f_{imp}^{s}} \tag{9.1}$$

where the value of g depends of the anomalous transport profile, and m=4. The factor f_{imp}^{s} takes account of the plasma confinement and it is based on the ISS-95 scaling laws [Yam04]. For the electron and ions anomalous transport diffusion the particle diffusivity coefficient is assumed as, $D_{e,i} = C_{ano}\chi_{ano}$ with C_{ano}=0.5.

9.2.2 Additional power

Central electron cyclotron heating of 200MW with power deposition width of 30% of plasma minor radius is assumed for start-up and burn control. The profile is shown in the following expression,

$$P_{ec} = P_0 \exp\left(-\frac{\rho^2}{0.3^2}\right) \tag{9.2}$$

9.2.3 Density control

Pellet injection fuelling model is used for the density control in order to get the desired fusion power output.

9.2.4 Plasma main parameters

The geometric characteristics, the magnetic field and the impurity concentration of the helical commercial reactor are given in table 9.1. The magnetic field configuration is the same one that is used in the standard LHD configuration with a 4.2 factor scale. The deuterium-tritium concentration is taken as equal.

Parameter	Value
Major radius R (m)	15.5
Minor radius a (m)	2.5
Factor scale	4.2
Magnetic field (T)	5
Reflection wall coefficient	0.9
% Impurity (Carbon)	1

Table 9.1 Main characteristics of the helical commercial reactor used for the simulations.

9.2.5 Simulation results

In the standard simulation case, high electron anomalous heat transport is assumed ($f_{impe} \approx 2.0$) whereas ion anomalous heat transport is small ($f_{impi} \approx 10.0$). The time evolution of the alpha power, additional power and radiated power for the burning helical plasma is shown in figure 9.1. As can be seen from the picture, with this configuration, the plasma can be ignited, leading to 450MW alpha power and 100MW of radiated power. This radiated power is divided in 95MW of bremsstrahlung and 5 MW of cyclotron radiation (CYTRAN routine has been used for this calculation). The 200MW input power are absolutely necessary in the first 30 s, until the plasma can be ignited. The electron temperature, ion temperature and electron density profiles when t=100s are shown in figure 9.2. Quite flat density profile is obtained, with $n_e(0) \approx 1.9 \times 10^{20}\ m^{-3}$, whereas temperature profiles are parabolic, with $T_e(0) \approx 23\ keV$ and $T_i(0) \approx 21\ keV$. The electron temperature is mainly determined by anomalous transport in this case, whereas ion temperature depends strongly on neoclassical ripple transport, which is determined by negative radial electric field, as shown in figure 9.3.

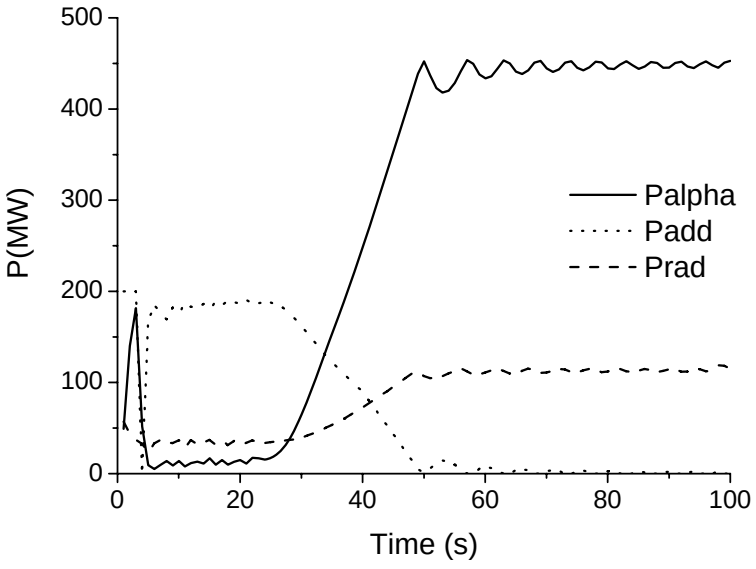

Figure 9.1 Time evolution of alpha power, additional power and radiated power for the helical commercial reactor.

As it was point in the previous sections, the working regime is in the high density and low temperature scenario. In this regime, electron neoclassical ripple losses are minimized (as it has been shown previously) and the key factor for heat losses is just anomalous one. However, in order to get these plasmas ignited with low ripple losses, a very large aspect

ratio is needed (in this case R=15.5 m and <a>=2.5m), which is a drawback due to the expensive costs and technical difficulties associated to its construction.

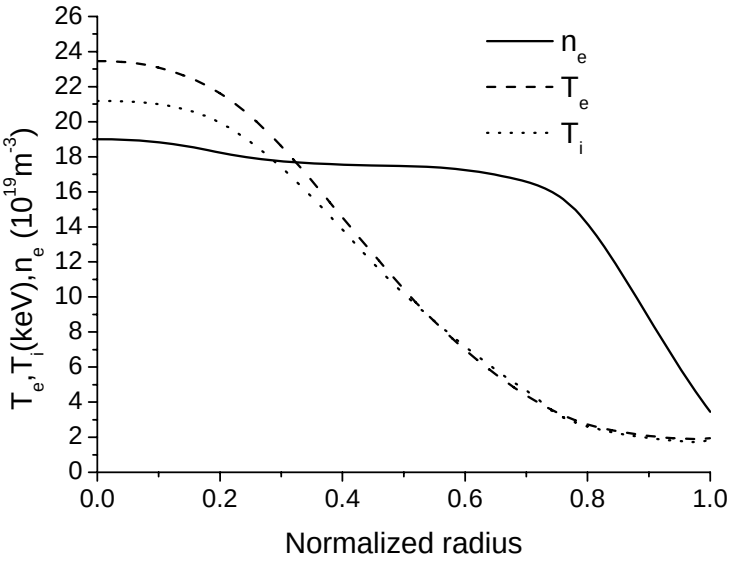

Figure 9.2 Electron temperature, ion temperature and electron density profiles for the helical commercial reactor when t=100s.

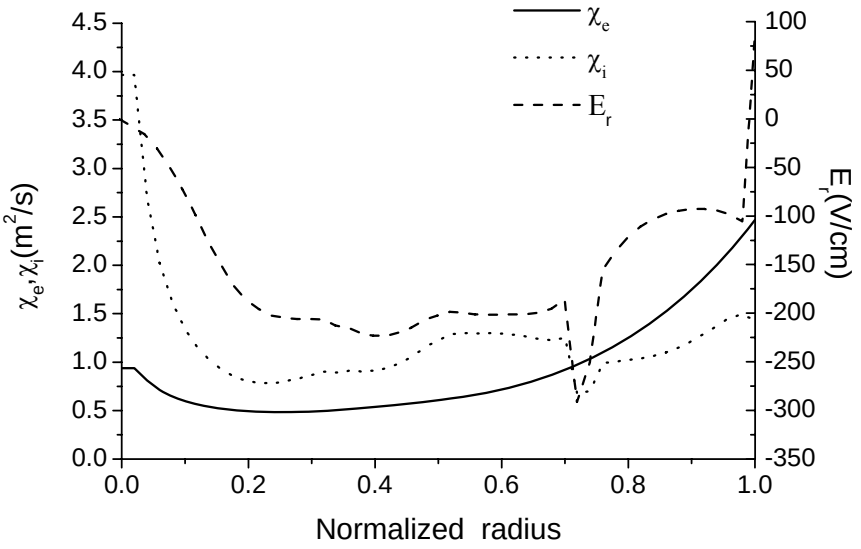

Figure 9.3 Electron thermal diffusivity, ion thermal diffusivity and radial electric field profiles for the helical commercial reactor when t=100s.

In order to see clearly what physical variables are more important in these plasmas, the detailed local density power balances for the plasma electrons are shown in figure 9.4.

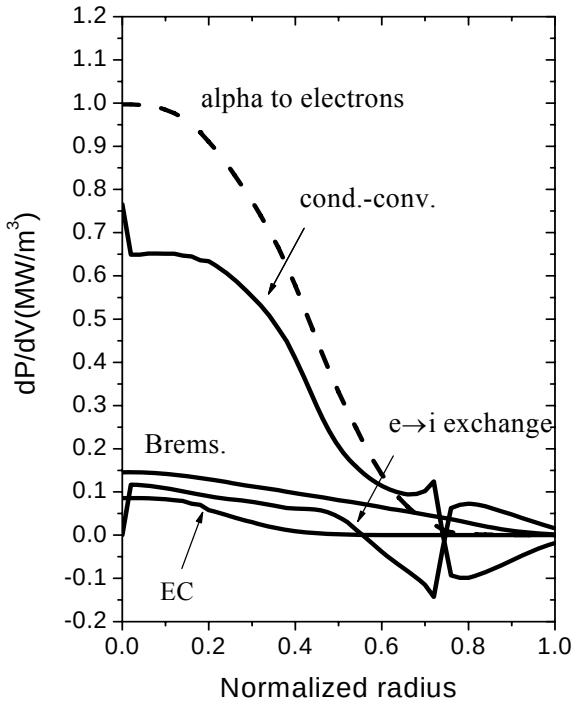

Figure 9.4 Local electron power balance for the Helical commercial reactor scenario when t=100s.

Related to the net source power densities there is just the alpha power coupled to electrons, since this is a steady-state regime. The main power density sink is conductive-convective losses. Related to radiated power density, bremsstrahlung losses are higher than the cyclotron ones in the whole plasma radius. Moreover, cyclotron radiation tends to be zero from ρ≈0.3 up to ρ≈1, whereas bremsstrahlung losses are always positive. The fact that bremsstrahlung power density losses are positive in the outer part of the plasma, where the magnetic surfaces are really large in this reactor, makes that the total radiated power due to bremsstrahlung losses be really high. This fact is due to the high density and low temperature working regime. In fact, the relative importance of electron cyclotron wave power emission (P_{EC}) compared with the power loss through bremsstrahlung (P_{brems}) can be well appreciated from the quasi-dimensionless global scaling [Alb04],

$$\frac{P_{EC}}{P_{brems}} \approx \left(\frac{n}{n_{Gw}}\right)^{-3/2} \left(aB_t\right)\left(\frac{qR}{a}\right)^{3/2} T_e^2 \tag{9.3}$$

where n is the density, a is the plasma minor radius, B_t is the confining toroidal magnetic field, q is the safety factor, R is the plasma major radius and T_e is the electron temperature. This shows that high electron temperature is most effective in making electron cyclotron

wave losses significant, followed by the product aB_t, which is a measure for the confinement capability.

The fact that cyclotron radiation importance in the commercial helical reactor tends to be small makes that the influence of the wall reflection coefficient on the plasma final conditions to be small too. Thus, the choice of the wall reflection R_w=0.9 for the simulation performed in this study does not seem to play an important role in the final results.

Therefore, a new result derived from this thesis is that the LHD helical plasmas can be ignited for R=15.5m, <a>=2.5m and B_t=5 T. However, as has been pointed previously, ion anomalous heat transport must be small. In order to see the influence of the ion heat channel on ignited plasmas, the improvement factor for ion anomalous transport has been chosen similar to the electrons $f_{impi} \approx 2.0$. Time evolution results for this new configuration are shown in figure 9.5. As can be seen from the picture, the plasma becomes thermally unstable and the density control to maintain the desired target of 450 MW alpha power becomes difficult too. Therefore, in order to consider the possibility of a helical commercial reactor, high ion confinement should be assumed.

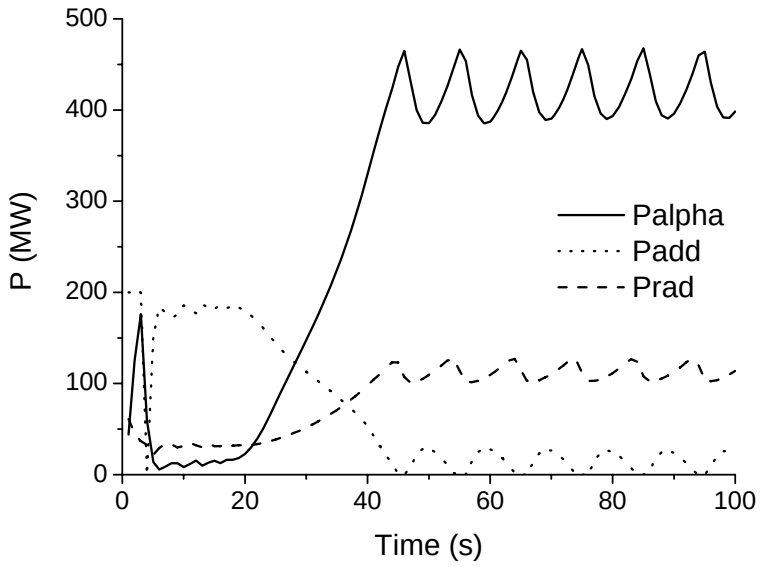

Figure 9.5 Time evolution of alpha power, additional power and radiated power for the helical commercial reactor when low ion confinement is assumed.

9.3 Tokamak simulation

Whereas it has been shown that electron cyclotron (EC) waves contribute comparatively little to the energy losses from a helical commercial reactor, their role in determining the level of energy transport and, hence, the plasma electron and ion temperatures and temperature profiles in the plasma core may be quite important, especially in steady-state tokamak operation scenarios which are characterised by good energy confinement, modest peak plasma density ($n(0) \approx 10^{20}$ m^{-3}), and high peak plasma temperatures ($T_e(0) \approx T_i(0) \approx 40$ keV). In fact, in this case, energy transport by EC waves, from the plasma core, is found to be of the same order and sometimes even larger than the plasma electron heat transport [Alb04]. This is due to the fact that net EC wave emission is strongest in the hot central region of the plasma while the cooler outer plasma layers are weak emitters or even net absorbers of EC waves. Therefore, in order to describe energy transport in steady-state reactor-grade tokamak plasma properly, not only a reliable model for plasma heat transport by conduction and convection is required, but also transport by EC waves must be modelled satisfactorily. This implies that a description of EC wave transport is needed which takes the essentially non-local character of this transport mechanism, due to wave reabsorption and wave reflection, into account.

In this study, in addition to ITER steady-state operation conditions [Pol02], for comparison, ITER inductive operation, as well as steady-state operation of the ITER-EDA [ITE99] as an example of a device approaching fusion reactor conditions is also addressed.

9.3.1 ITER study

To describe EC wave transport covering non-local effects in an approximate but easily treatable way, the CYTRAN routine [Tam81] was adopted. This routine has been tested before against more exact numerical [Tam83] and analytical [Alb02] models and was found to be a reasonable approximation to the latter. The CYTRAN routine was coupled to the ASTRA transport code [Per91]. ASTRA also contains an approach to EC emission in which Trubnikov's formula for the total EC wave power loss from the plasma [Tru79] is applied locally in an ad hoc way. Hence, a comparison between the results of the non-local and this latter model, which has been used frequently in the past, could be made.

9.3.1.1 Transport model

As far as the plasma transport properties are concerned, the standard ITER transport models were adopted. For (most of) the steady-state scenarios, the electron and ion thermal

diffusivities, χ_e and χ_i, respectively, are taken following the phenomenological model of [Pol02] for H-mode transport with an internal transport barrier, namely,

$$\chi_i = \chi_e = Cf(\rho)\left[1 - H(\rho - \rho_1)\right]F(s) + \chi_i^{neo} \tag{9.4}$$

where $C = 0.3\text{m}^2\text{s}^{-1}$ and $f(\rho) = 1 + 3\rho^2$, with $\rho = r/a$ being the radial coordinate normalized with respect to a and $H(\sigma)$ is the Heaviside function, with ρ_1 being taken as 0.95 to model reduced transport at an H-mode edge. $F(s) = 1/(1 + \exp(7(1 - s)))$, with s describing magnetic shear, $s = rq'/q$, accounts for the drop of the thermal diffusivities to the neoclassical value of the ion thermal diffusivity, χ_i^{neo}, in the negative and low shear regions of the plasma interior. The plasma impurity content is modelled by taking an admixture of 2% of beryllium and 0.3% of argon and assuming for the effective confinement time of helium a value around five times the plasma energy confinement time with respect to conductive–convective losses, this value being adjusted in such a way that the effective ion charge number Z_{eff} of the plasma characteristic of ITER steady-state scenarios is reproduced. Also, a similar current profile is assumed to those calculated previously for ITER operation conditions [Pol02].

For the ITER inductive regime, H-mode transport properties are modelled through

$$\chi_i = \chi_e = Cf(\rho)\left[1 - H(\rho - \rho_1)\right] + 2H(\rho - \rho_1)\chi_i^{neo} \tag{9.5}$$

with $C = 0.4\text{m}^2\,\text{s}^{-1}$, and the argon admixture is reduced to 0.1%.

9.3.1.2 Additional power

The heating by fusion α-particles is described by the usual local model, the transfer of power to the plasma electrons and ions being due to binary collisions. For the D–T fusion rate, Putvinskii's analytical fit [Put88] is adopted. The spatial distribution of the external heating power density injected into the plasma, $\text{d}P_{\text{ext}}/\text{d}V$, is taken to be Gaussian,

$$P_{ec} \sim \exp\left(-\frac{\rho^2}{\rho_{width}^2}\right) \tag{9.6}$$

with $\rho_{width} = 0.6$ and it is assumed that this power is distributed between electrons and ions in the ratio 80:20. As far as wall reflection of EC waves is concerned, polarization scrambling is disregarded, as this does not have an important impact on the global plasma parameters [Alb05].

9.3.1.3 Simulation parameters

	Steady-state 1	Steady-state 2	Inductive
Major radius R (m)	6.4	6.4	6.2
Minor Radius a (m)	1.9	1.9	2.0
Elongation/triangularity	1.9/0.40	1.9/0.40	1.7/0.33
B_t (T)	5.2	5.2	5.3
I (MA)	9.0	9.0	15
$n_e(0)$ (10^{19} m^{-3})	7.0	7.0	11
$<n_e>$ (10^{19} m^{-3})	6.4	6.4	10
$T_e(0)$ (keV)	36	43	24
$<T_e>$(keV)	17	19	8.5
$T_i(0)$ (keV)	37	53	19
$<T_i>$ (keV)	17	21	8.0
W(MJ)/τ_E (s)	360/3.0	430/3.5	310/3.3
P_α (MW)/P_{ext} (MW)	82/68	97/68	76/40
P_{EC} (MW)/P_{Brems} (MW)	18/15	29/15	4.1/20
P_{con} (MW)/Q	120/6.0	120/7.1	92/9.5
Z_{eff}/f_{He} (%)	2.3/6.0	2.3/6.0	1.7/3.1
q_0/q_{95}	4.4/4.5	3.8/4.6	0.84/2.7

Table 9.2 Global characteristics of ITER operation scenarios; it is assumed that the external power P_{ext} has a Gaussian profile and is distributed between electrons and ions in the ratio 80:20.

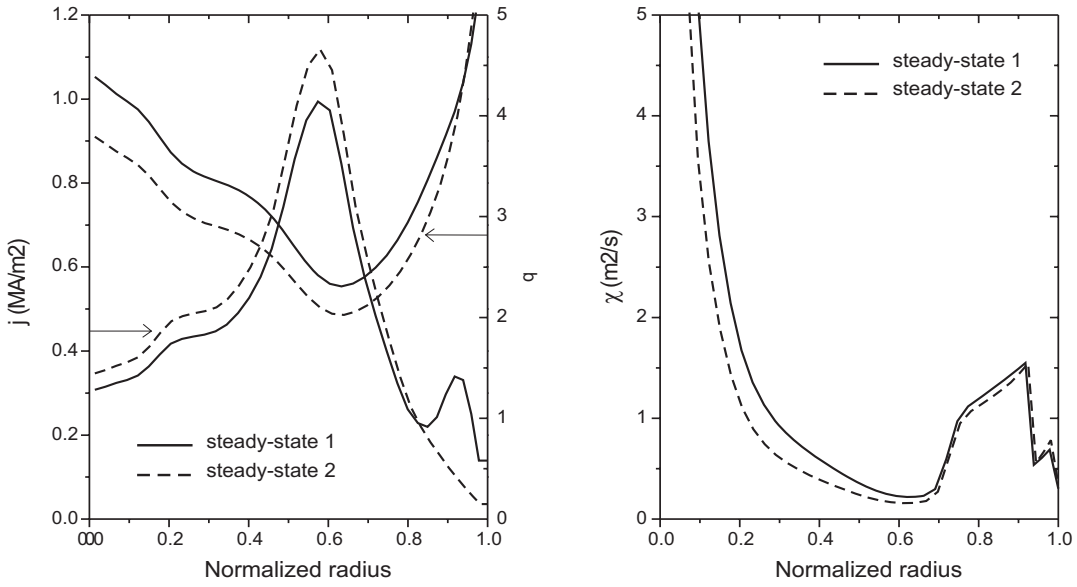

Figure 9.6. Profiles of the current density j and of the safety factor q (left) as well as of the thermal diffusivities (right).

The global characteristics of the operation scenarios considered for ITER are given in Table 9.2. Here, the steady-state case 1 and the inductive case are modelled along the lines of the published ITER scenarios [Pol02]. The steady-state scenario 2 has a slightly modified current profile, the current density in the core being slightly increased and that adjacent to the edge somewhat lower, at constant total current; consequently, the thermal heat conduction in the plasma core tends to be reduced. In figure 9.6, the profiles of the current density $j(\rho)$ adopted for the two steady-state scenarios, as well as those of the safety factor q and the thermal diffusivities $\chi_i(\rho) = \chi_e(\rho)$, are documented.

9.3.1.4 Simulation results

In figure 9.7, the electron temperature (T_e) profiles, for various wall reflection coefficients R_w of the EC waves (assumed to be constant over the relevant frequency range and over the wall surface), are given for the three scenarios. It is seen that the impact of varying R_w is weak as long as $R_w \leq 0.6$ for the steady-state 1 and 2 scenarios and small for the inductive case. Since $R_w = 0.6$ also appears to be a reasonable effective value to be expected for next-step tokamak devices and reactors, this value is adopted generally in the following.

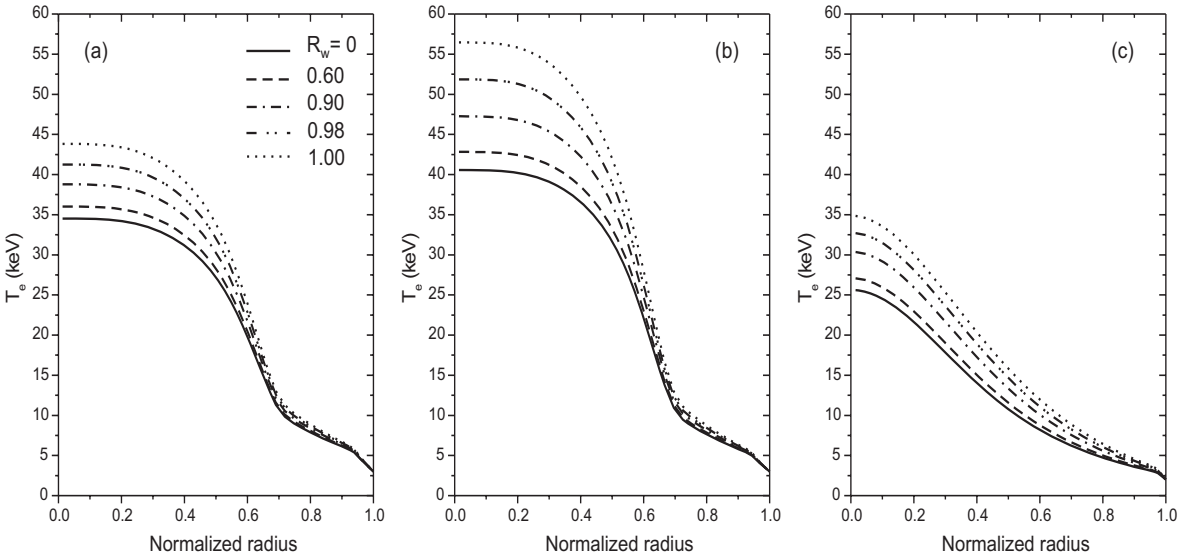

Figure 9.7 Electron temperatures profiles $T_e(r/a)$ for various values of the wall reflection coefficient R_w: (a) steady-state 1, (b) steady-state 2, and (c) inductive, where the R_w curves are identical.

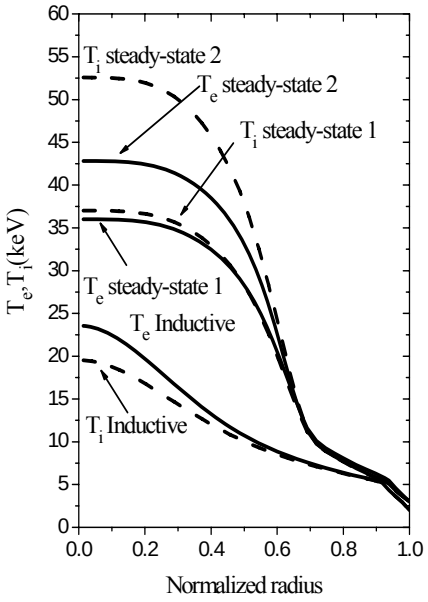

Figure 9.8. Electron (T_e) and ion (T_i) temperature profiles for the ITER scenarios of Table I and for $R_w = 0.6$.

Figure 9.8 shows the ion temperature (T_i) profiles, in addition to those of the electron temperature (T_e), for the three scenarios at $R_w = 0.6$. Although the total heating power going to the electrons is much larger than that transferred to the ions and the heat conductivities of electrons and ions are assumed to be equal, T_i is larger than T_e in the plasma core in the steady-state cases. This is a consequence of the strong radiative cooling of the electrons when T_e is high ($T_e \geq 35$ keV) in the core, (T_i-T_e) increases with increasing T_e as then electrons are more efficiently cooled by radiation while collisional energy transfer between ions and electrons is reduced. Comparing the two steady-state scenarios, from figures 1 and 2 it is also seen that the actual core values of T_e and T_i in the high-temperature (steady-state) regime, quite sensitively depend on the strength of electron heat transport.

The detailed local power balances for the plasma electrons are shown in figure 9.9. Note that the electron cyclotron power loss $(dP/dV)_{EC}$ is the effective one, given by the emitted power density reduced for the power density reabsorbed by the plasma from the EC wave field. For high core electron temperatures (and always for large $R_w \rightarrow 1$), adjacent to the plasma edge, this contribution effectively is a heat source as reabsorption becomes stronger than genuine emission there.

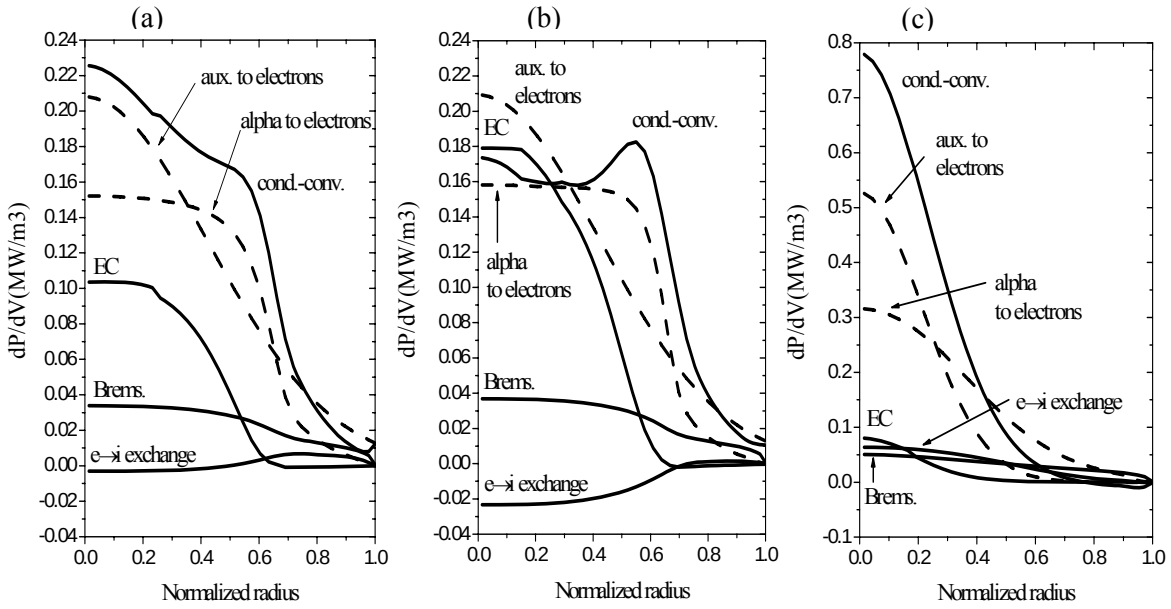

Figure 9.9. Local electron power balance for the ITER scenarios of Table 9.2 and for R_w=0.6: (a) steady-state 1, (b) steady-state 2, and (c) inductive.

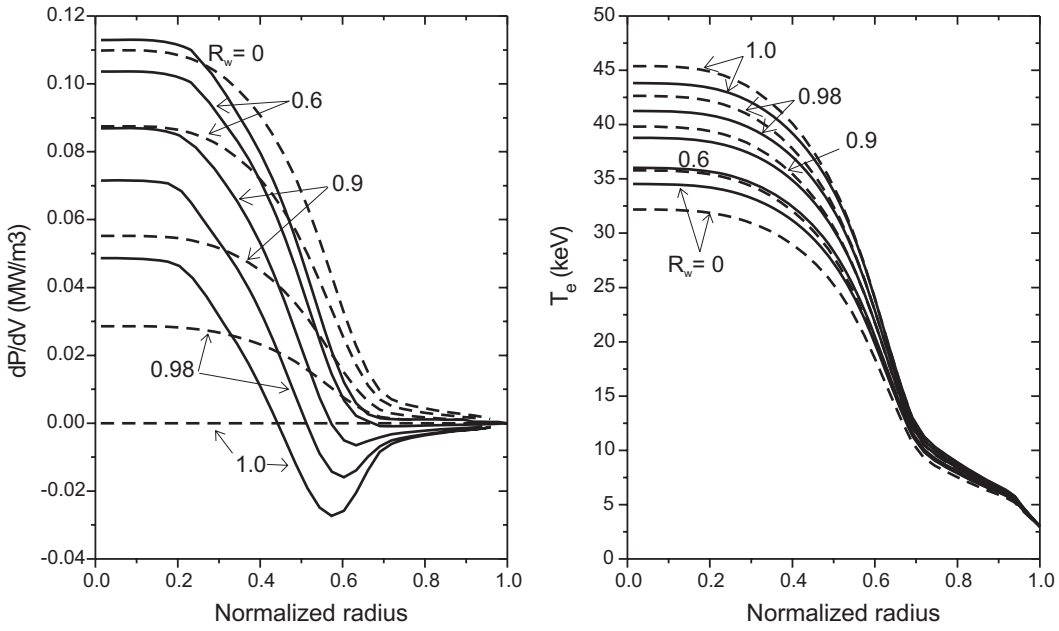

Figure 9.10. Comparison between a non-local model (CYTRAN) for EC radiative transfer (solid) and a local approach based on Trubnikov's formula (dashed) on the profile of the effective EC power density radiated (left) and that of the electron temperature (right) for ITER steady-state case 1 and various wall reflection coefficients R_w.

The main feature transparent from figure 9.9 is that the importance of the power loss of electrons by EC waves strongly increases with increasing electron temperature and, effectively, becomes the dominant electron cooling mechanism in steady-state operation of

ITER in the core plasma if the core electron temperature exceeds about 40 keV (see figure 9.7 (b)). Such a situation, although the ITER reference steady-state regime (figure 9.7 (a)) does not quite reach such conditions, could well arise in practice, given the sensitivity of the core electron temperature to small changes of the heat transport and heating conditions. On the other hand, if $T_e(0)$ is below 25 keV, as happens in the reference inductive scenario, $(dP/dV)_{EC}$ is no longer an important contribution to the local electron power balance, of the order or even less important than bremsstrahlung. It should be noted that the predominant importance of the electron temperature for the strength of EC electron cooling is to be expected on the basis of simple scaling arguments, as shown in the expression 9.3, however, the correct analysis of this phenomenon has been carried out for the first time in this thesis.

A comparison between the non-local approach used here and the local one based on Trubnikov's formula [Tru79] is shown for ITER steady-state case 1 in figure 9.10. As expected, global model underestimates the spatial structure of the EC emission profile, yielding too a low power loss in the plasma core and overestimating it in the outer plasma, the deviation being the stronger the larger is R_w. For the electron temperature profile the difference is less pronounced because of compensation effects.

9.3.2 ITER- EDA

In order to display the impact of the size (or, more precisely, of the confinement capability) of the tokamak device, steady-state operation of the larger ITER as considered earlier in the EDA ("ITER-EDA") and which approaches fusion reactor conditions, have also been analyzed, assuming the same transport model and current density profile as for the steady-state case 1 of ITER in section 9.3.1. To avoid the very high ion temperature arising under these conditions, a case in which ion heat transport is enhanced by a factor 1.5 ('steady-state 3') was treated in addition. The global characteristics of these scenarios are given in Table 9.3, whereas the electron and ion temperature profiles are shown in figure 9.11 (a) for a wall reflection coefficient $R_w = 0.6$.

The local power balances of the electrons are given in figures 9.11 (b) and (c). The main result is that, for a larger confinement capability, the importance of EC wave emission in cooling the core electrons is enhanced (as is to be expected from the simple scaling argument shown in expression 9.3). It is, in fact, the dominant cooling mechanism for both ITER-EDA scenarios considered. Of course, the quite high electron temperatures attained in these scenarios are also essential for this.

	Steady-state 1	**Steady-state 3**
Major radius R (m)	8.1	8.1
Minor Radius a (m)	2.8	2.8
Elongation/triangularity	1.8/0.40	1.8/0.40
B_t (T)	5.7	5.7
I (MA)	15	15
$n_e(0)$ (10^{19} m^{-3})	7.0	7.0
$<n_e>$ (10^{19} m^{-3})	6.4	6.4
$T_e(0)$ (keV)	40	38
$<T_e>$ (keV)	19	17
$T_i(0)$ (keV)	52	43
$<T_i>$ (keV)	23	18
$W(MJ)/\tau_E$ (s)	1200/5.8	1100/5.9
P_α (MW)/P_{ext} (MW)	250/70	220/70
P_{EC} (MW)/P_{Brems} (MW)	67/46	62/44
P_{con} (MW)/Q	210/18	180/15
Z_{eff} /f_{He} (%)	2.3/5.9	2.3/5.9
q_0/q_{95}	4.7/5.6	4.8/5.4

Table 9.3 Global characteristics of ITER-EDA operation scenarios; Steady-state 1: same transport assumptions as for corresponding ITER scenario of Table I; Steady-State 3: ion heat transport enhanced by a factor 1.5.

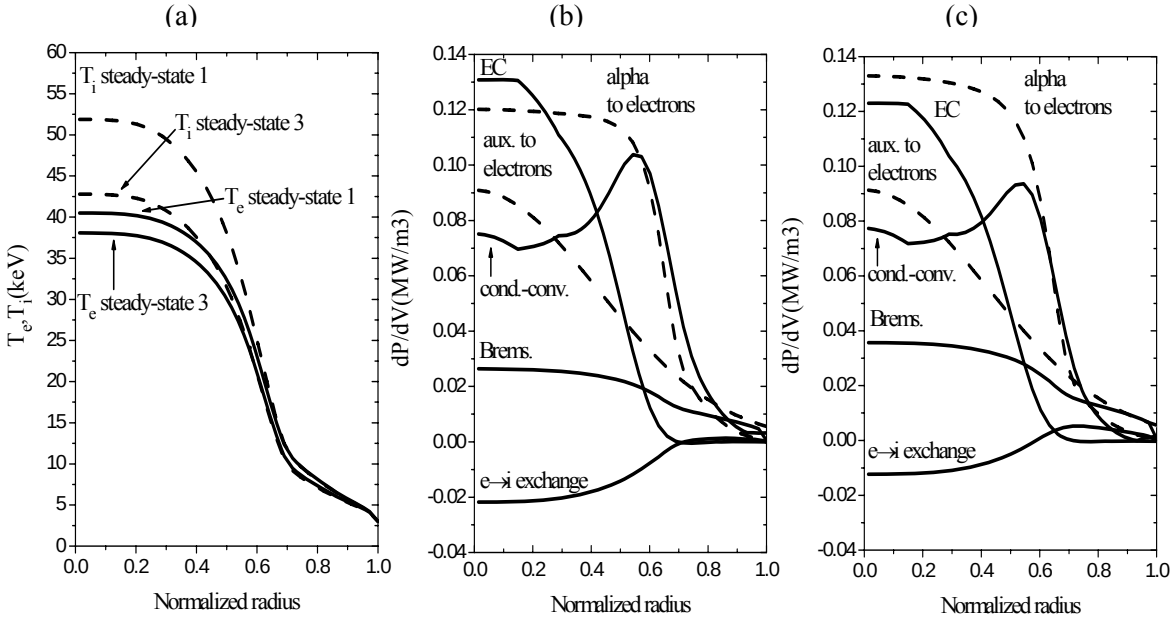

Figure 9.11 Electron (T_e) and ion (T_i) temperature profiles for the ITER-EDA steady-state scenarios of Table 9.3 and for $R_w = 0.6$ (a). Local electron power balance for the ITER-EDA scenarios of Table 9.3 and for $R_w = 0.6$: (b) steady-state 1; (c) steady-state 3.

Therefore, and as a new conclusion derived from this thesis, the comparison between helical and tokamak fusion reactors shows that the physical variables that are mainly involved are quite different. As previously pointed, in the helical reactor conductive-convective and bremmstralung losses seems to drive electron heat channel, however in the tokamak case, due to the high temperature and low density regime, cyclotron radiation may become the most important cooling mechanism for the electrons. This feature can be an important issue for the future tokamak commercial reactor, since it should be taken into account the importance of the wall reflection coefficient in the reactor wall design.

9.4 Conclusions

The helical commercial reactor (based on the LHD design) plasma conditions have been analyzed by means of TOTAL_P code. As a new result derived from this thesis, it has been shown that the plasma can be ignited for R=15.5m, <a>=2.5m and B_t=5T if small anomalous ion heat transport is assumed. In this case, ion channel is completely determined by ripple transport with negative electric field. Otherwise, with anomalous ion and electron heat transport of the same order, the plasma tends to be unstable and it is difficult to achieve the ignition.

The temperatures profiles obtained are quite parabolic, with $T_e(0) \approx 23\ keV$ and $T_i(0) \approx 21\ keV$, and the density pretty flat, with $n_e(0) \approx 1.9 \times 10^{20}\ m^{-3}$. These conditions make possible to achieve the fusion target of 450MW alpha power. In this situation of low temperatures and high density regime the detailed electron power balance has been analyzed. In order to have the most accurate results, CYTRAN routine has been used to take account of the non-local effects of the cyclotron radiation. The analysis shows that the main losses are due to convective-conductive and bremsstrahlung processes, whereas cyclotron radiation tends to be almost negligible. Total radiation power consists in 95MW of bremsstrahlung and only 5MW of cyclotron radiation, moreover, the effect of the wall reflection coefficient is not important in this case.

The analysis of ITER operation regime, focusing on the importance of electron cyclotron wave emission in the local electron power balance, was analyzed using the CYTRAN routine coupled to the ASTRA code which allows covering non-local effects in the wave emission. In addition, also steady-state ITER-EDA working conditions were considered in order to compare the results with the commercial helical case.

As the importance of electron cyclotron emission mainly depends on the electron temperature, it can become a significant cooling mechanism for the core electrons,

exceeding bremsstrahlung, in ITER steady-state operation regimes when the core electron temperature is higher than about 35 keV, and tends to become the dominant one for core electron temperatures above 40 keV. On the other hand, for inductive operation of ITER where the core electron temperature is expected to be about 20 keV, locally electron cyclotron power losses are small. Conversely, in steady-state operation of a device larger than ITER, approaching tokamak commercial reactor conditions, such as the ITER-EDA, the relative importance of core electron cooling by electron cyclotron wave emission is enhanced.

The overall importance of wall reflection of electron cyclotron waves was shown to be small as long as $R_w \leq 0.6$. However, small changes in the transport properties may affect the core electron and ion temperatures significantly and may be decisive for which of the plasma species is hotter in the plasma core.

In conclusion, both tokamak and helical fusion device concepts are able to be the next step future commercial reactors. However, quite different physical processes are involved in both devices and they must be taken into account in order to improve the final design. As has been pointed in this thesis, the accurate analysis of cyclotron radiation and the importance of the wall design seem quite important in order to determine what temperature will be higher in the plasma core of the commercial tokamak. Moreover, wall design with a high reflection coefficient also seems an issue. However, in the helical case, the size of the device and the ion confinement are problems that seem to be major difficulties.

Conclusions

Analysis and modeling of magnetically confined plasmas has become quite important in order to predict the main features of future fusion devices. The design of ITER, as well as other future machines (including the commercial reactor), depends strongly on our capability to predict the behavior of the confined plasma. Computer codes have become a necessary tool for these analyses, since with the actual computers, real time simulations can be performed with acceptable accuracy leading to reasonable global results. Otherwise, if more physically depth analyses are needed, computers can spend several days in order to give more sophisticated results.

In this thesis three different codes, PRETOR-Stellarator, TOTAL and ASTRA, have been used to analyze different features of the magnetically confined plasmas. PRETOR-Stellarator and TOTAL codes have been used to perform simulations and analyses of different aspects of LHD and TJ-II stellarator devices. Finally, ASTRA transport code has been used to compare performance of ITER and the future tokamak commercial reactor with the helical commercial device.

As a first step to analyze and compare some of the latest results obtained in both LHD and TJ-II devices, a complete neoclassical transport model has been introduced in PRETOR-Stellarator. Neoclassical transport has become an important subject in the last years since in many experiments, mainly with eITB, the experimental heat diffusivity is reduced to neoclassical levels. Moreover, the formation of the eITB seems to be linked with the appearance of a high electric field in the plasma core. The origin of this electric field is completely determined by neoclassical transport in stellarators (more correctly is caused by the appearance of non-axisymmetric particle fluxes). In addition, with this model, the lack of such transport in PRETOR-Stellarator (which is particularly important in the stellarator case) is overcome.

Two main approaches to neoclassical transport issue are available. Monte-Carlo techniques can give accurate results, however, are expensive in computational time and are not able to analyze real time plasmas. Another possibility comes by solving the drift kinetic equation. This algebraic method, although possibly not so accurate as the Monte-Carlo one, allows performing real time simulations and also allows seeing interaction between neoclassical transport and other physical variables of the plasma. This last method was choosing to analyze neoclassical transport by means of PRETOR-Stellarator code.

After performing several numerical benchmarking with other neoclassical codes and checking that results were compatible, a preliminary study of neoclassical transport in TJ-II was done. In order to make not just a neoclassical study but a comparison with previously Monte Carlo neoclassical studies performed at CIEMAT, fixed temperature and density profiles (in the case of low and high density regimes) were analyzed. The conclusions show that, as a new contribution of this thesis, results are compatible with that obtained with Monte Carlo techniques, however, with this drift kinetic approximation real time results can be obtained.

Some of the main characteristics of neoclassical transport in TJ-II derived from this fixed profile analyses are the following. First, the electric field has a high positive value in the plasma core and low values (alternating positive and negative) at the plasma edge. Second, unlike in many other stellarators, there is only one solution of the ambipolar equation. In spite of this feature, a high sheared electric field shear is obtained. As it has been shown in this thesis for the first time for the TJ-II, the fact that there is only one solution is due to the special ratio of electron and ion temperatures, $Te/Ti \gg 1$. In the case of higher ion temperatures, the ambipolar equation may lead to three solutions (as expected) with a negative electric field profile. Third, the neoclassical thermal diffusivity is of the order of the experimental one in the plasma core for low densities. For higher densities, the region where they are comparable is reduced.

One shot of the LHD has been analyzed with PRETOR-Stellarator in order to compare neoclassical transport with TJ-II device in the low density case. The results show how a high positive electric field appears in the plasma core; however, unlike in TJ-II, the electric field tends to be again positive at the plasma edge. This feature is closely linked with the ion density profile. Related to thermal diffusivities, it has been shown that are probably neoclassical in the plasma core, as it was pointed for TJ-II case. These results are comparable with the ones obtained with PROCTR code as well as with experimental data.

It can be deduced from the new results of this thesis that the neoclassical transport in LHD as well as in TJ-II can be analyzed is a fast way by using PRETOR-Stellarator code leading to results in concordance with other studies.

eITB formation is one of the most recent achievements in fusion studies. In order to study its formation from the transport point of view, two tools are necessary: first neoclassical transport and second a good description of anomalous transport, which is also present in the eITB scenarios. Some studies have been performed related to anomalous transport previously in LHD, see [Yam92] or [Yam02], however a study of anomalous transport in TJ-II seemed necessary in order to analyze the eITB formation.

Therefore, some anomalous transport models were introduced in PRETOR-Stellarator to simulate TJ-II plasmas. These models can be divided in two categories: semi-empirical models and theoretical models. The semi-empirical models are closely related to different time scaling of some other stellarator devices, e.g. W7-AS and LHD; whereas theoretical models correspond to short and long drift wave models. In order to perform the simulations, two discharges from a density scan were selected, one with low density (and high temperature) and other with high density (and low temperature). Results show that W7-AS and LHD models with no power deposition dependence can simulate the high density discharge with accuracy, however in the low density case the results are not satisfactory unless the model is mended (usually LHD model is corrected for the low densities scenarios). Related to theoretical models, electrostatic model (long wavelength) seems to underestimates heat transport, whereas electromagnetic model (short wavelength) gives a reasonable correct temperature profile mainly in the low density case in which a steeped temperature gradient appears (although the high density case is reasonably well simulated). The heat diffusivity obtained is always growing in whole the plasma radius (except at the edge). This fact has been also obtained elsewhere by using ASTRA code [Lop03].

Thus, from the new results obtained in this thesis, it can be concluded that anomalous transport in TJ-II can be driven by Electron Temperature Gradient (ETG) drift wave modes with short wavelength and that W7-AS model may reproduce high density scenarios in TJ-II, whereas LHD scaling is not suitable for low density discharges.

The low density discharge previously studies correspond to an enhanced heat scenario with internal transport barrier. In spite of electromagnetic models tends to describe correctly this shot, it can not absolutely reproduce the transition between a high density scenario with no eITB and a low density scenario with eITB. This is because some

other effect has to be taken account. In order to study the eITB formation correctly the suppression of anomalous transport by the radial electric field is studied in both LHD and TJ-II.

In the LHD case, this study has been done by adding two different type of anomalous transport to TOTAL code, electrostatic (in this case GyroBohm-like) and the electromagnetic one already used for TJ-II. The effect of anomalous transport reduction by $E \times B$ flow has been also taken account. In order to study the eITB formation, an experimental shot with low density and steeped temperature was selected. Simulations show that electromagnetic models are suitable for the plasma core and GyroBohm one for outside. A new model which mixes both type of transport was derived for this thesis to overcome this difficulty. Results show as this kind of model together with the effect of electric field shear can simulate with reasonable accuracy the experimental shot, as well as the experimental central temperature dependence on average density and the appearance of a critical density. Thus, the new results obtained in this thesis show that the eITB formation in LHD is due to some combined effects. Main heat transport in LHD is due to GyroBohm scaling. However, below a certain average density, a high electric field with a high electric field shear suppress anomalous GyroBohm transport and makes possible the appearance of small convective cells which are responsible of a new anomalous transport mode (electromagnetic) in the plasma core.

The TJ-II study was performed by using the same electromagnetic model used for LHD and the same anomalous transport suppression. It has been shown that the transition between non-eITB and eITB is well simulated since the experimental temperature profiles are correctly reproduced. The electric field obtained with the neoclassical model introduced in PRETOR-Stellarator is quite similar to the experimental one for both types of shots. Neoclassical heat diffusivity in the eITB shot is close to the experimental one in a wide range of the plasma core, however in the non-eITB scenario, this range is reduced. Hence, a new contribution of this thesis is that the transition between non-eITB plasmas and eITB plasmas can be understood as the combined effect of a high electric field with a high electric field shear together with the electromagnetic drift wave transport.

It is worth to point out another important conclusion which arises from this thesis. These results have been obtained by using a routine for computing neoclassical transport which is much faster than the one usually used (based in Monte Carlo techniques), however, results are in concordance with the experimental ones. This fact allows the analysis of the plasmas in an easier way by observing the interaction between neoclassical features and other variables.

In spite of electron heat transport can be studied by analyzing electron heat diffusivity as it has been done throughout this thesis, some important physical processes can not be understood in this "diffusion" framework, e.g. cold pulse propagation. When a sudden perturbation in the plasma temperature is localized at the edge, it propagates through the plasma with a velocity much faster that the expected from a diffusion framework. In order to study such transport, a new non-local heat transport model derived for this thesis has been used. This model is a convolution over the neoclassical transport by means of a kernel which consists in a Levy distribution. This distribution has been chosen because from experimental results the correlation between different points when a cold pulse is propagating obeys such distribution.

When applying sudden density instability to steady-state plasma in LHD device, some interesting results are obtained when this model is used. First, the velocity propagation is much faster than in the diffusive case. Second, in both frameworks the velocity drops at $\rho = 0.3$, however in the non-local case it raises again in the core. Third, the instability propagation tends to keep its front. That is, the instability tends to travel in a first moment like a wave and later the diffusive part of the transport is recovered. All these facts have been experimentally observed not just in LHD but in other fusion devices as TJ-II. In addition, a simulation of a LHD steady-state shot has been performed. It has been shown from the results that it is reasonable well simulated. Therefore, these new results derived from this thesis show that this non-local model can explain many transient phenomena which are difficult to analyze in a diffusive framework. Moreover, one LHD steady-state experimental shot has been simulated too.

Anyway, more studies must be done in order to completely confirm the validity of such kind of models. First, it should be applied to other fusion devices, TJ-II for instance. Second, a more formally mathematical framework should be used to derive this kind of model (probably based in stochastic methods). And third, the kernel used in the model applied in this thesis is based on the experimental data, however in order to have a consistent theory of non-local transport, this kernel should be derived from the physical assumptions of the model. At the present time, this last remark seems far from being possible.

Finally, once that all the physical tools needed for a complete stellarator simulation are available, a comparison between the helical commercial reactor and ITER as well as ITER-EDA (as an example of tokamak-like reactor) has been carried out to analyze what physical variables determine the evolution of the future burning plasmas in stellarators and tokamaks.

As a new result derived from this thesis, it has been shown that a commercial helical reactor based in the LHD design can be ignited with major radius of 15.5m and magnetic field of 5T, leading to 450MW alpha power and 100MW radiated power. However, in order to have sufficient plasma stability, low ion heat losses should be considered. It has been also shown that the working regime of such reactor is the high density and low temperature, since in this situation ripple losses are minimized. If the ion heat losses are of the same level than the electron ones, the plasma tends to be unstable due to the higher density needed to reach the desired output power. From the loss power density analysis it is deduced that principal cooling mechanism for the electrons are convective-conductive losses and radiated power. The radiated power comes in a 95% from bremsstrahlung losses, whereas cyclotron losses effect on plasma are almost negligible. This feature is due to the high density and low temperature working regime. Therefore, the non-local effects of cyclotron radiation (which have been introduced in TOTAL code by means of CYTRAN routine) and the effect of wall reflection coefficient on the plasma are almost negligible.

In addition to this, and for comparison, the effects of non-local cyclotron radiation transport and the wall reflection coefficient on magnetically confined tokamak plasmas has been carried out for ITER and ITER-EDA. The new results derived from this thesis show that, unlike in the stellarator case, cyclotron radiation can be the main cooling mechanism for the core electrons in the ITER steady-state when electron central temperature is above 35keV.On the other hand, in the inductive scenarios, with $T_e(0) \approx 25\ keV$, cyclotron radiation effects are small. As in the helical case, the effects on cyclotron radiation are important for high temperatures. Related to plasma dependence on wall reflection coefficient, it has been found that central electron temperature increases by increasing reflection coefficient. In addition, the effect of wall reflection is small for $R_w \leq 0.6$.

The results obtained for ITER are even more important for the ITER-EDA case. It has been shown that in steady-state operation of a device larger than ITER, approaching tokamak commercial reactor conditions, such as the ITER-EDA, the relative importance of core electron cooling by electron cyclotron wave emission is enhanced. In this case there is no need of high temperatures for obtaining high electron cyclotron losses in the plasma core. This feature is due to the cyclotron radiation dependence on confinement capability.

Therefore, both stellarators and tokamaks are able to be the next-step fusion commercial reactors. However, both designs have their own drawbacks. In the stellarator case, steady-state is something inherent to the design but, as it has been pointed here, ion transport and the reactor size lead to serious difficulties. In the tokamak case, steady-state

scenarios can be difficult to reach due to the extremely high cyclotron losses which can be reduced by having a higher wall reflection coefficient. However, this issue must be studied deeper, since burning plasmas and therefore, the future of fusion energy, may depend strongly.

Appendix

List of common symbols

a	m	Minor radius
A		Aspect ratio
$<a>$	m	Average minor radius
B	T	Total magnetic field
B_t	T	Toroidal magnetic field
B_θ	T	Poloidal magnetic field
D_e	m^2s^{-1}	Helical particle diffusion coefficient
D_{gs}	m^2s^{-1}	Banana particle diffusion coefficient
D_h	m^2s^{-1}	Helical particle diffusion coefficient
D_p	m^2s^{-1}	Plateau particle diffusion coefficient
D_{ps}	m^2s^{-1}	Pfirsch-Schlüter particle diffusion coefficient
D_k^{ano}	m^2s^{-1}	Anomalous particle diffusivity of specie k
E_r	Vm^{-1}	Radial electric field
$E_{r,neo}$	Vm^{-1}	Neoclassical radial electric field
$E_{r\ \max}^{neo}$	Vm^{-1}	Maximum neoclassical radial electric field
f_{BS}		Bootstrap current fraction
f_{He}		Helium particles fraction
f_k		Particle distribution of specie k
g_{ij}		Metric tensor
$H(\rho)$		Heaviside function
I	MA	Plasma current
J	MAm^{-2}	Plasma density current
L_{Pe}	m	Electron pressure characteristic length
L_{Te}	m	Electron temperature characteristic length
M	kg	Plasma effective mass number
m_i	kg	Atom mass of ions

m_k	kg	Atom mass of specie k
n	10^{19} m^{-3}	Plasma density
n_D	10^{19} m^{-3}	Deuterium density
n_e	10^{19} m^{-3}	Electron density
$n_e(0)$	10^{19} m^{-3}	Central electron density
$<n_e>$	10^{19} m^{-3}	Average electron density
$n_{e,max}$	10^{19} m^{-3}	Maximum electron density
n_{Gw}	10^{19} m^{-3}	Greenwald density limit
n_k	10^{19} m^{-3}	Density of specie k
n_T	10^{19} m^{-3}	Tritium density
n_α	10^{19} m^{-3}	Alpha particles density
p_k	10^{19} $keVm^{-3}$	Plasma pressure of specie k
p_e	10^{19} $keVm^{-3}$	Electron pressure
p_i	10^{19} $keVm^{-3}$	Ion pressure
P_{brems}	MW	Bremsstrahlung power density losses
P_{con}	MW	Conductive-convective losses
P_e	MW	Electron total heat sources and sinks power
P_{EC}	MW	Electron cyclotron power density losses
P_{ext}	MW	External power
P_i	MW	Ion total heat sources and sinks power
P_α	MW	Alpha power
q		Security factor
q_0		Central security factor
q_{95}		Security factor at the magnetic surface with 95% of the magnetic toroidal flux
Q		Power amplification factor
Q_e^{neoc}	MWm^{-2}	Neoclassical electron heat flux
Q_k^{neoc}	MWm^{-2}	Neoclassical heat flux of specie k
Q_k^{na}	MWm^{-2}	Non-ambipolar neoclassical heat flux of specie k
Q_e	MWm^{-2}	Electron heat flux
R	m	Major radius
R_w		Wall reflection coefficient
S_k	$m^{-3}s^{-1}$	Particle source of specie k
T_e	keV	Electron temperature
$T_e(0)$	keV	Central electron temperature
$T_{e,max}$	keV	Maximum electron temperature
T_i	keV	Ion temperature
$Ti(0)$	keV	Central ion temperature

$T_{i,max}$	keV	Maximum ion temperature
T_k	keV	Temperature of specie k
$<T_e>$	keV	Average electron temperature
$<T_i>$	keV	Average ion temperature
u_k	ms^{-1}	Plasma flow velocity of specie k
u_i	ms^{-1}	Ion flow velocity
$v_{\|\|}$	ms^{-1}	Particle parallel velocity
v_t	ms^{-1}	Thermal velocity
V'	m^2	Radial derivative of the plasma volume
W	MJ	Stored energy
W_{max}	MJ	Maximum stored energy
Z_{eff}		Plasma effective charge
z_k		Atomic number of specie k
β		Plasma beta
$\beta(0)$		Central plasma beta
β_{max}		Maximum beta
ρ		Normalized minor radius
ρ_i	m	Ion Larmor radius
ρ_{wid}		Power deposition width
τ	s	Plasma confinement time
τ_E	ms	Energy confinement time
τ_{max}	s	Maximum plasma confinement time
ι		Rotational transform
ι_0		Central rotational transform
(V,θ,ξ)		Hamada coordinates
(R,Z,ξ)		Cylindrical coordinates
(ρ,θ,ζ)		Flux coordinates
Γ_k^{neoc}	$10^{19}m^{-2}s^{-1}$	Neoclassical particle flux of specie k
Γ_k^{ano}	$10^{19}m^{-2}s^{-1}$	Anomalous particle flux of specie k
Γ_e^{neoc}	$10^{19}m^{-2}s^{-1}$	Neoclassical electron particle flux
Γ_e	$10^{19}m^{-2}s^{-1}$	Electron particle flux
Γ_i	$10^{19}m^{-2}s^{-1}$	Ion particle flux
Γ_k^{na}	$10^{19}m^{-2}s^{-1}$	Non-ambipolar neoclassical particle flux of specie k
Γ_e^{ano}	$10^{19}m^{-2}s^{-1}$	Anomalous electron particle flux
$\left\langle \left\|\nabla\rho\right\|^2 \right\rangle$		Metric tensor average
$V_{p,e}$	ms^{-1}	Electron pinch velocity
$V_{p,k}$	ms^{-1}	Pinch velocity of specie k

$\langle \sigma v \rangle_{fusion}$	10^{19} m^{-3} s^{-1}	Deuterium-Tritium reaction cross section
ε_h		Helical ripple
ε_t		Toroidal ripple
χ_e	m^2s^{-1}	Electron heat diffusivity
χ_k^{ano}	m^2s^{-1}	Anomalous heat diffusivity of specie k
χ_e^{ano}	m^2s^{-1}	Electron anomalous heat diffusivity
χ_{ripple}	m^2s^{-1}	Non-ambipolar electron heat diffusivity
χ_{sym}	m^2s^{-1}	Axisymmetric electron heat diffusivity
χ_e^{neo}	m^2s^{-1}	Neoclassical electron heat diffusivity
χ_i^{neo}	m^2s^{-1}	Neoclassical ion heat diffusivity
$\overleftrightarrow{\Pi}_k$		Viscous tensor of specie k
$\overleftrightarrow{\Pi}_i$		Ion viscous tensor
ν_{ei}	s^{-1}	Electron-ion collision frequency
ω_{pe}	s^{-1}	Plasma frequency
$\delta(r'-r)$		Dirac delta

Bibliography

[Alb02] Albajar F., Bornatici M. and Engelmann F. "*Electron cyclotron radiative transfer in fusion plasmas*", Nucl. Fusion **42** 670 (2002)

[Alb04] Albajar F, Bornatici M., Cortes G., Dies J., Engelmann F., Garcia J., Izquierdo J. "*Electron cyclotron radiation transfer in fusion plasmas: use of the ASTRA transport code coupled with the CYTRAN routine*", ECA (EPS-CCFPP) **28G** P-4.171 (2004)

[Alb05] Albajar F., Bornatici M. and Engelmann F. "*Electron cyclotron radiative transfer in the presence of polarization scrambling in wall reflections*", Nucl. Fusion **45** 9 (2005)

[Ale90] Alejaldre C. et. al. *"TJ-II project: a flexible heliac stellarator"*, Fusion Technology **17** 131 (1990).

[Ama00] Amano T., Hernegger F., Wobig H., Yamazaki K., "*Adaptation of TOTAL_P code for interactive modelling of transport phenomena in stellarators and helias reactor*", Report IPP-III/246, 2000

[Ama82] Amano T., Mizuno J., Kako M., "*Simulation of impurity transport in tokamak I*" Report IPPJ-616, Nagoya Univ. Inst. of Plasma Physics, 1982

[Boe02] Boedo, J.A., Gray D.S., Ferry P.W., Jachmich S., Tynan G.R., Conn R.W., TEXTOR-94 Team "*Scaling of plasma turbulence suppression with velocity shear"* Nucl. Fusion **42** 117-121 (2002)

[Bou92] Boucher D., *"Études et modelisation du transport de l'energie de particules dans un plasma du fusion thermonucléaire côntrolée. Aplication au transport anormal et aux conditions du fontionenement du tokamak"*, Ph. D. Thesis, Ecole Polytechnique de Paris, (1992)

[Bud03] Budaev V.P., Takamura S., Ohno N., Komori A., Masuzaki S., Kirnev G.S., Garshing S.A., "Edge plasma turbulence in fusion devices: Bursty behaviour and fractal properties", ECA (EPS-CCFPP) **27A** P-3.174 (2003)

[Bur97] Burrell K.H., "*Effects of E x B velocity shear and magnetic shear on turbulence and transport in magnetic confinement devices*", Phys. Plasmas **4** 1499 (1997)

[Cam98] Campbell, Colin J. and Laherrere, Jean J. "*The end of cheap oil*", Scientific American **91** March (1998)

[Cas00] Castejón F., et al. Problems of Atomic Science and Technology. 2000. Nº6. Series: Plasma Physics (6). p. 3-7

[Cas02] Castejón F., Tribaldos V., García-Cortés I., E. de la Luna, Herranz J., Pastor I., Estrada T., TJ-II Team, "*Enhanced heat confinement in the flexible heliac TJ-II*", Nucl. Fusion **42**, 271-280 (2002)

[Cas04] Castejón F., López-Bruna D., Estrada T., Ascasíbar E., Zurro B. and Baciero A. "*Influence of low-order rational magnetic surfaces on heat transport in TJ-II heliac ECRH plasmas*", Nucl. Fusion **44** 593 (2004)

[Cha82] Chang C.S., Hinton F.L., "*Effect of finite aspect ratio on the neoclassical ion thermal conductivity in the banana regime* ", Phys Fluids **25** 1493(1982)

[CIE05] Available at the web site of the CIEMAT: http://www-fusion.ciemat.es/New_fusion/en/

[Con90] Conn R.W. et al., "*Economic safety and environmental prospects of fusion reactors* " Nucl. Fusion **30** 1919 (1990)

[Cru88] Crume, E.C., Shaing, K.C., Hirshman, S.P., Van Rij W.I., "*Transport scaling in the collisionless-detrapping regime in stellarators*", Phys Fluids **31** 11 (1988)

[Die02] Dies J., Castejón F., Fontdecaba J.M., Fontanet J., Izquierdo J., Cortes G., Alejaldre C., *"Benchmarking of PRETOR-Stellrarator code using PROCTR simulations on TJ-II shots",* ECA (EPS-CCFPP) **26B** 5.027.1-5.027.4 (2002)

[Die04] Dies J., Castejón F., García J., Fontdecaba J.M., Albajar F., Izquierdo J.," *Benchmarking of electrón heat difusión models in TJ-II plasmas*" ECA (EPS-CCFPP) **28B** 4.172 (2004)

[EFD05] Available at the website of the JET: http://www.jet.efda.org

[Egu03] Eguilior S., Castejón F., E de la Luna, Cappa A., Likin K., Fernández A. and TJ-II Team "*Heat wave experiments on TJ-II flexible heliac*", Plasma Phys. Control. Fusion **45** 105 (2003)

[EIA99] Energy Information Administration (Department of energy of U.S.), "*International Energy Annual 1999*". Available at the website of the EIA: http://www.eia.dov.gov/international

[Fig03] Figarella C.F., Benkadda S., Beyer P.,Garbet P. and Voitsekhovitch I., "*Transport Reduction by Rotation Shear in Tokamak-Edge Turbulence*" Phys. Rev. Lett. **90** 015002 (2003)

[Fon01] Fontanet F., *"Simulación de plasmas de dispositivos de fusión por confinamiento magnético tipo tokamak y stellarator.Validación experimental y aplicación al estudio del Heliac Flexible TJ-II",* Ph. D. Thesis, Universitat Politecnica de Catalunya , (2001).

[Fon99] Fontanet J., Dies F., Castejon F., Alejaldre C., "*Adaptation of PRETOR code to stellararator simulation. Applicattion to shots of flexible heliac TJ-II*." ECA (EPS-CCFPP) **23J** 345 (1999).

[Fow78] Fowler R.H., Smith J., Rome J.A., "*A fast ion Fokker-Planck code*", Comput. Phys. Commun. **13** 323-340 (1977)

[Fuj99] Fujisawa A., Iguchi H., Minami T., Yoshimura Y., Sanuki H., Itoh K., Lee S., Tanaka K., Yokoyama M., Kojima M.,. Itoh S., Okamura S., Akiyama R., Ida K., Isobe M., Morita S., Nishimura S., Osakabe M., Shimizu A., Takahashi C., Toi K., Hamada Y., Matsuoka K., and Fujiwara M., "*Electron Thermal Transport Barrier and Density Fluctuation Reduction in a Toroidal Helical Plasma*" Phys. Rev. Lett. **82** (1999) 2669

[Fun02] Funaba H., Shimozuma T., Kubo S., Idei H., Yoshimura Y., Notake T., Narihara K., Ida K., Nagayama Y., Inagaki S., Takeiri Y., Osakabe M., Tanaka K., Peterson B.J., Watanabe K.Y., Murakami S., Yokoyama M., Kawahata K., Ohyabu N. and the LHD Experimental Group, "*Transport Analysis of ECH Overlapped NBI Plasmas in LHD*", ECA (EPS-CCFPP) **26B** P-1.077 (2002)

[Gal98] Galli P., Cherubini A., De Angelis R., De Luca F., Erba M., Giannella R., Gorini G., Jacchia A., Jäckel H., Mantica P., Parail V.V., Porte L. and Taroni A., "*Transient heat transport studies using laser ablated impurity injection in JET*", Nucl. Fusion **38** 1355 (1998)

[Gar04] Garcia J., Yamazaki K., Dies J., Castejon F., Funaba H., Amano T., Fontdecaba J.M., Fontanet J., Albajar F., Izquierdo J., *"Neoclassical transport studies in stellarators using PRETOR code",* Journal of Plasma and Fusion Res. SERIES **6** (2004) 481

[Gar06] Garcia J., Yamazaki K., Dies J., Izquierdo J. *"Internal transport barrier simulationand analysis in the LHD",* Plasma Phys. Control. Fusion **48** 15-27 (2006)

[Gen97] Gentle K.W., K. W. Gentle, R. V. Bravenec, G. Cima, G. A. Hallock, P. E. Phillips, D. W. Ross, W. L. Rowan, and A. J. Wootton, "*The evidence for nonlocal transport in the Texas Experimental Tokamak*", Phys. Plasmas **4** 3599 (1997)

[Has85] Hastings D., Houlberg W., Shaing, K.-C., "*The ambipolar electric field in stellarators*", Nucl. Fusion **25** 445 (1985)

[Her00] Herranz J., Pastor I., Castejón F., E. de la Luna, García-Cortés I., Barth C. J., Ascasíbar E., Sánchez J., and Tribaldos V., "*Profile Structures of TJ-II Stellarator*", Plasmas Phy. Rev. Lett. **85** 4715 (2000)

[Hin76] Hinton F.L., Hazeltine R.D., "*Theory of plasma transport in toroidal confinement systems*", Rev. Mod. Phys. **48**, 239(1976)

[Hir86] Hirshman S.P., Shaing K.C., Van Rij W.I., Beasly C.O., Crume E.C., Phys. Fluids **29** (1986)

[Hor03] Horton W., Hu B., Dong J.Q. and Zhu P., "*Turbulent electron thermal transport in tokamaks*", New Journal of Physics **5** (2003)

[Hor88] Horton W., Hong B. G., Tang W. M., "*Toroidal electron temperature gradient driven drift modes*", Phys. Fluids **31** 2971 (1988).

[Hug78] Hughes M.H., Post D. E., "*A Monte Carlo algorithm for calculating neutral gas transport in cylindrical plasmas*", J. Comput. Physics **28** 43-55 (1978)

[Hul83] Hulse R., Nucl. Technology/Fusion, **3**, 259-272 (1983)

[Ida03] Ida, K., Shimozuma T., Funaba H., Narihara K., Kubo S., Murakami S., Wakasa A., Yokoyama M., Takeiri Y., Watanabe K. Y., Tanaka K., Yoshinuma M., Liang Y. and Ohyabu N., "*Characteristics of Electron Heat Transport of Plasma with an Electron Internal-Transport Barrier in the Large Helical Device*", Phy. Rev. Lett. **91,** 085003 (2003)

[Ide93] Idei H., Ida K., Sanuki H., Yamada H., Iguchi H., Kubo S., Akiyama R., Arimoto H., Fujiwara M., Hosokawa M., Matsuoka K., Morita S., Nishimura K., Ohkubo K., Okamura S., Sakakibara S., Takahashi C., Takita Y., Tsumori K., and Yamada I., "*Transition of the radial electric field by electron cyclotron heating in the CHS heliotron/torsatron*", Phy. Rev. Lett. **71** 2220 (1993)

[Ina04] Inagaki S., Ida K., Tamura N., Shimozuma T., Kubo S., Nagayama Y., Kawahata K., Sudo S., Ohkubo K., and LHD Experimental Group, "*Cold pulse experiments in plasma with an electron internal transport barrier on LHD*", Plasma Phys. Control. Fusion **40** (2004)

[IPP05] Available at the web site of the W7-X Project: http://www.ipp.mpg.de/de/for/projekte/w7x/for_proj_w7x.html

[ITE05] Available at the website of the ITER: http://www.iter.org

[ITE99] ITER Physics Basis Editors *et al* Nucl. Fusion **39** 2137 (1999)

[Ito96] Itoh K. and Itoh S.I., "*The role of the electric field in confinement*", Plasma Phys. Control. Fusion **38** 1 (1996)

[Jac00] Jachmich J., and Weynants R.R., "*Efficiency of transport suppression due to E×B flow shear - a parameter study*", Plasma Phys. Control. Fusion **42** (2000)

[Kaw99] Kawahata K., Tanaka K., Ito Y., Ejiri A., and Okajima S., "*Far infrared laser interferometer system on the Large Helical Device*" Rev. Sci. Instruments **70** 707 (1999)

[Kim90] Kim D., Duk-In Choi, Horton W., Yushmanov P. N. and Parail V. V., "*Transition from neoclassical to turbulent electron diffusion* ", Phys. Fluids **B 2** 547-53 (1990)

[Kis96] Kissick M.W., Callen J.D., Fredrickson E.D., Janos A.C. and Taylor G. " *Non-local component of electron heat transport in TFTR*", Nucl. Fusion **36** 1691 (1996)

[Kop00] Koponen J.P.T., Geist T., Stroth U., Fiedler S., Hartfuss H.-J., Heinrich O., Walter H., ECH Group, W7-AS Team and Dumbrajs O., "*Perturbative particle transport studies in the W7-AS stellarator*", Nucl. Fusion **40** 365 (2000)

[Kut95] Kuteev B.V., "*Hydrogen pellet ablation and acceleration by current in high temperature plasmas*", Nucl. Fusion **35** 431-453 (1995)

[Lis76] Lister G.C., Post D. E. and Goldston R., "*Plasma heating in toroidal devices*", Third Sympos. Plasma Heating in Toroidal Devices, 303-307 (1976)

[Lop03] López-Bruna D., Castejón F., Fontdecaba J.M., "*Transporte con ASTRA en TJ-II*", CIEMAT internal report.

[Lot88] Lotz W., Nührenberg J., "*Monte Carlo computations of neoclassical transport*", Phys. Fluids **31** 2984 (1988)

[Lyo00] Lyon J.F., M. Valanju P., Zarnstorff M. C., Hirshman S. P., Spong D. A., Strickler D. J., Ware A. S., and Williamson D. E., "*Compact stellarators as reactors*", 18th IAEA Fusion Energy Conference, (2000)

[Maa00] Maaβberg H., Beidler C. D., Gasparino U., Romé M., Dyabilin K. S., Marushchenko N. B., and Murakami S., "*The neoclassical ``Electron Root'' feature in the Wendelstein-7-AS stellarator* ", Phys. Plasmas **7** 295 (2000)

[Man02] Mantica P., Gorini G., Imbeaux F., Kinsey J., Sarazin Y., Budny R., Coffey I., Dux R., Garbet X., Garzotti L., Ingesson C., Kissick M., Parail V., Sois C., Walden A., and contributors to the EFDA-JET Workprogramme, "*Perturbative transport experiments in JET low or reverse magnetic shear plasmas*", Plasma Phys. Control. Fusion **44** 2185 (2002)

[Man77] Mandelbrot B.B., "*Intermittent turbulence in self-similar cascades: divergence of high moments and dimension of the carrier*", J. Fluid Mech. **62** 331 (1974)

[Mil02] Van Milligen B.P., E. de la Luna, Tabarés F.L., Ascasíbar E., Estrada T., Castejón F., Castellano J., García-Cortés I., Herranz J., Hidalgo C., Jimenez J.A., Medina F., Ochando, M, Pastor I., Pedrosa M.A., Tafalla D., García L., Sánchez R., Petrov A., Sarksian K. and Skvortsova N., "*Ballistic transport phenomena in TJ-II*", Nucl. Fusion **42** 787-795 (2002)

[Min04] Minami T., Fujisawa A., Iguchi H., Liang Y., Ida K., Nishimura S., Yokoyama M., Murakami S., Yoshimura Y., Isobe M., Suzuki C., Nomura I., Toi K., Yoshinuma M., Shimizu A., Takahashi C., Matsuoka K., Okamura S. and CHS group, "*Increased understanding of neoclassical internal transport barriers in CHS*", Nucl. Fusion **44** 342 (2004)

[Nar01] Narihara K., Yamada I., K., Hayashi H., and Yamauchi K., "*Design and performance of the Thomson scattering diagnostic on LHD*", Rev. Sci. Instruments **72** 1122 (2001)

[NIF04] Available at the website of the National Institute for Fusion Science: http://www.nifs.ac.jp

[Par78] Parks P.B., Turnbull R. J., "*Effect of transonic flow in the ablation cloud on the lifetime of a solid hydrogen pellet in a plasma*", Phys. Fluids **21** 1735-1741 (1978)

[Per91] Pereverzev G. and Yushmanov P.N., "*ASTRA: Automated System for TRansport Analysis in a Tokamak*", Report IPP 5/42 (1991)

[Pol02] Polevoi A.R., Medvedev S.Yu., Pustovitov V.D., Mukhovatov V.S., Shimada M., Ivanov A.A., Poshekhonov Yu.Yu., Chu M.S.,*" Possibility of Q>5 Stable Steady-state Operation in ITER with Moderate β and H-factor*", Proc. 19th Int. Conf. on Fusion Energy (Lyon, 2002) CD-ROM file CT/P-08

[PPP05] Available at the website of the Princeton Plasma Physics Laboratory: http://www.pppl.gov

[PPP05b] Avalaible at the website of the Princeton Plasma Physics Laboratory: http://w3.pppl.gov/~hammett/gyrofluid/gyrofluid.html

[Put88] Putvinskii S.V. "*Some aspects of the kinetics of nuclear reactions in a thermonuclear plasma"* Problems of Nuclear Science and Technology (Thermonuclear Fusion) ed Ye.P. Velikhov (Moscow: State Committee on the Utilization of Nuclear Energy, USSR) p3

[Rij89] Van Rij W. I. and Hirshman S. P., "*Variational bounds for transport coefficients in three-dimensional toroidal plasmas*", Phys. Fluids **B1** 563 (1989)

[Rin90] Ringler H., Ringler H., Gasparino U., Kuhner G., Maassberg H., Renner H. and Sardei F., "*Confinement studies on the Wendelstein VII-AS stellarator*", Plasma Phys. Control. Fusion **32** 933 (1990)

[San05] Sánchez R., B. Ph. van Milligen and Carreras B. A. "*Probabilistic transport models for plasma transport in the presence of critical thresholds: Beyond the diffusive paradigm*", Phys. Plasmas **12** 056105 (2005)

[San05b] Sánchez J. and Tribaldos V., "*Keeping the options open: concept improvements and stellarator physics*", Plasma Phys. Control. Fusion **47** (2005) B349–B361

[Sha05] Shaing K.C. "On the relation between neoclassical transport and turbulent transport", Phys. Plasmas **12** 082508 (2005)

[Sha83] Shaing K.C., Callen J.D., "*Neoclassical flows and transport in nonaxisymmetric toroidal plasmas*", Phys Fluids **26** 3315(1983)

[SST05] Available at the website of the Spherical Stellarator project: http://www.highfactor.com/ss/

[Str01] Stroth U., Itoh K., Itoh S.-I., Hartfuss H., Laqua H., the ECRH team, and the W7-AS team, "*Internal Transport Barrier Triggered by Neoclassical Transport in W7-AS*", Phy. Rev. Lett. **86** 5910 (2001)

[Str01b] Stroth U., Itoh K., Itoh S.-I., Hartfuss H., Laqua H., "*Internal transport barriers in W7-AS*", J. Plasma Fusion Res. SERIES **4** (2001)

[Sud90] Sudo S., Takeiri Y., Zushi H., Itoh K., Itoh S.-I., Kondo K., Liyoshi A., Nucl. Fusion **30** 11 (1990)

[Tal01] Tala T., Heikkinen J. A., Parail V. V., Baranov Yu. F. and Karttunen S. J. "*ITB formation in terms of $\omega_{E\times B}$ flow shear and magnetic shear on JET*", Plasma Phys. Control. Fusion **43** 507 (2001)

[Tam81] Tamor S., "*A simple fast routine for computation of energy transport by synchrotron radiation in tokamaks and similar geometries*", Rep. SAI-023-81-189-LJ/LAPS-72, Science Applications, Inc., La Jolla, CA (1981)

[Tam83] Tamor S., "*Calculation of energy transport by cyclotron radiation in fusion plasmas*", Nucl. Technol. Fusion **3** 293 (1983)

[Tod02] Toda S. and. Itoh K, "*Theoretical study of the structure of the electric field in helical toroidal plasmas by the use of an anomalous transport model*", Plasma Phys. Control. Fusion **44** 325 (2002)

[Tri01] Tribaldos V., "*Monte Carlo estimation of neoclassical transport for the TJ-II stellarator* ", Phys. Plasmas **8** 1229 (2001).

[Tru79] Trubnikov B.A. *Reviews of Plasma Physics* vol 7, ed M.A. Leontovich (New York: Consultants Bureau) p 345 (1979)

[UN05] Available at the website of the United Nations: http://www.un.org

[UNE01] Climate change 2001, synthesis report. Intergovernmental panel on climate change, United Nations Environment Program

[USc01] Schwenn U., "*Videoconferencing at IPP: Transition from H.320 Point-to-Point to H.323 Multipoint*", 3rd IAEA Technical Committee meeting on Control, Data Acquisition, and Remote Participation for Fusion Research, Padova , July (2001)

[Veg03] Vega J., Sánchez E., López. A., Portas A., Ochando M., Mollinedo A., Sánchez A., Ruiz M., López S and Barrera E., "*Design of the TJ-II remote participation system*", Rev. Sci. Ins. **74** 1791 (2003)

[Wak01] Wakasa A., Murakami S., Maaβberg H., Beidler C.D., Nakajima N., Watanabe K., Yamada H., Okamoto M., Oikawa S., Itagaki S., *"Monte Carlo simulations of neoclassical transport in inward shifted LHD configurations"*, J. Plasma Fusion Res. SERIES **4** 408 (2001)

[Wak98] Wakatani M., "*Stellarator and Heliotron devices*", Oxford University Press (1998)

[Woo90] Wootton A.J., Carreras B. A., Matsumoto H., McGuire K., Peebles W. A., Ritz Ch. P., Terry P. W., and Zweben S. J., "*Fluctuations and anomalous transport in tokamaks*", Phys. Fluids B 2, 2879 (1990)

[Yam02] Yamazaki K., Minami K., Narihara K., Tanaka K., Kubo S. and LHD experimental group, "*Transport barrier analysis of LHD plasmas in comparison with neoclassical models*", J. Plasma Fusion Res. SERIES **5** 611-615 (2002)

[Yam04] Yamazaki K, Milkhailov M., Sakakibara S., Okamura S., García J., Dies J., Funaba H., Amano T., *"Neoclassical and Anomalous Transport Analyses of Helical Reactors",* J. Plasma and Fusion Res. SERIES **6** 357-361 (2004)

[Yam04b] Yamazaki K, 9th Workshop on MHD and Stability Control**,** November 21-23 PPPL (2004)

[Yam92] Yamazaki K. and Amano T., "*Plasma transport simulation modelling for helical confinement systems*", Nuclear Fusion **32** (1992)

Publications associated to the thesis

The work presented in this thesis has produced the following publications in reviews, communications in conferences and reports:

Articles and conferences

Internal transport barrier simulation and analysis in LHD
García J., Yamazaki K., Dies J., Izquierdo J.
Plasma Phys. Control. Fusion **48** (2006) 15–27

Theoretical transport analysis in TJ-II scenarios with enhanced heat confinement
Dies J., Castejón F., Garcia J., Izquierdo J.
Submitted to Plasma Physics and Controlled Fusion

Importance of Electron Cyclotron Wave Energy Transport in ITER
Albajar F., Bornatici M., Cortes G., Dies J., Engelmann F., Garcia J., Izquierdo J.
Nuclear Fusion **45** 642-648 (2005)

Internal transport barrier simulation in the LHD
García J., Yamazaki K., Dies J., Izquierdo J.
32nd European Physical Society (EPS) Conference on Plasma Physics, ECA **29C** P-5.037 (2005). http://eps2005.ciemat.es/papers/pdf/P5_037.pdf

Theoretical transport analysis in TJ-II scenarios with enhanced heat confinement
Dies J., Castejón F., Garcia J., Izquierdo J.
32nd European Physical Society (EPS) Conference on Plasma Physics, ECA **29C** P-5.036 (2005). http://eps2005.ciemat.es/papers/pdf/P5_036.pdf

Electron Cyclotron Radiation Studies Using the ASTRA Transport Code Coupled with the Cytran Routine
Dies J., García J., Albajar F., Fontdecaba J.M., Cortés G., Izquierdo J.
Journal of Plasma and Fusion Research Series **6** 469-472 (2004)

Neoclassical transport studies in TJ-II stellarator using PRETOR code
García J., Yamazaki K., Dies J., Castejón F., Funaba H., Amano T., Fontdecaba J.M., Fontanet J., Albajar F., Izquierdo J.
Journal of Plasma and Fusion Research Series, **6** 481-484 (2004)

Neoclassical and Anomalous Transport Analyses of Helical Reactors
Yamazaki K., Milkhailov M., Sakakibara S., Okamura S., García J., Dies J., Funaba H., Amano T.
Journal of Plasma and Fusion Research, Series **6** 357-361 (2004)

Importance of Electron Cyclotron Wave Energy Transport in ITER
Albajar F., Bornatici M., Cortes G., Dies J., Engelmann F., Garcia J., Izquierdo J.
20a IAEA Fusion Energy Conference, pp 4-18, Vilamoura, Portugal, November 2004

Simulation Modeling of Impurity Transport in Toroidal Fusion Plasmas
Yamazaki K., Amano T., Igitkhanov Y., García J., Dies J., Samitov M., Mikhailov M.
14th International Toki Conference on Plasma Physics and Controlled Nuclear Fusion, pp 2-38, Toki, Japan, October 2004

Energy-resolved neutral particle fluxes in TJ-II ECRH plasmas
Fontdecaba J.M., Castejón F., Balbín R., López-Bruna D., Yakovlevich S., Albajar F., Cortés G., Dies J., Garcia J., Izquierdo J., Fontanet. J.
Fusion Science and Technology **46** (2) 271-278 (2004)

Risk assessment of initiating events for ITER
Izquierdo J., Taylor N.P., Dies J., García J., Albajar F.
30a Reunión Anual de la Sociedad Nuclear Española, pp 13-08, Alicante, Spain, September 2004

Comparación y análisis de modelos de transporte de energía utilizando descargas de TJ-II
Dies J., Castejón F., Garcia J., Fontdecaba J. M., Albajar F., Izquierdo J.
30a Reunión Anual de la Sociedad Nuclear Española, pp 13-09, Alicante, Spain, September 2004

Progress in the development of a PIE-PIT for the ITER Tokamak
Izquierdo J., Taylor N.P., Dies J., García J., Albajar F.
23rd Symposium on Fusion Technology, pp 373, Venice, Italy, September 2004

Benchmarking of electron heat diffusion models in TJ-II plasmas
Dies J., Castejón F., García J., Fontdecaba J. M., Albajar F., Izquierdo J.
31st European Physical Society (EPS) Conference on Plasma Physics, ECA (EPS-CCFPP) **28B** P- 4.172 (2004). http://eps2004.clf.rl.ac.uk/pdf/P4_172.pdf

Electron cyclotron radiation transfer in fusion plasmas: use of the ASTRA transport code coupled with the CYTRAN routine
Albajar F., Bornatici M., Cortes G., Dies J., Engelmann F., Garcia J., Izquierdo J.

31st European Physical Society (EPS) Conference on Plasma Physics, ECA (EPS-CCFPP) **28B** P- 4.171 (2004). http://eps2004.clf.rl.ac.uk/pdf/P4_171.pdf

Electron cyclotron radiation studies using the ASTRA transport code coupled with the CYTRAN routine
Albajar F., Bornatici M., Cortes G., Dies J., Engelmann F., Garcia J., Izquierdo J.
13th Joint Workshop on ECE and ECRH, Nizhny Novgorod, Russia, May 2004

Acoplamiento de la Subroutina Cytran en el Código ASTRA para Cálculo de las Pérdidas de Energía por Radiación. Aplicación a las Condiciones de Operación de ITER
Díes J., García J., Albajar F., Fontdecaba J. M., Izquierdo J., Cortés G., Fontanet J.
29ª Reunión Anual de la Sociedad Nuclear Española, Zaragoza, October 2003

Ion heat transport analysis in TJ-II plasma
Fontdecaba J.M., Castejón F., Balbín R., López-Bruna D., Albajar F., Cortés G., Díes J., García J., Izquierdo J., Fontanet J.
14th Stellarator Workshop, Greifswald (Germany), September 2003

El proyecto ITER-Vandellòs
Dies J., Fontdecaba J. M., Izquierdo J., Cortes G., Garcia J., Albajar F.
Seguridad Nuclear, nº 24, pp 30-37, September 2002

Reports

Internal Transport Barrier Simulation in LHD
Garcia J., Yamazaki K., Dies J., Izquierdo J.
Research Report NIFS Series, NIFS-813, ISSN 0915-633X, Toki, June 2005